Records of Himalayan Metamorphism and Contractional Tectonics in the central Himalayas (Darondi Khola, Nepal)

Elizabeth Catlos[1]

[1]The University of Texas at Austin, Jackson School of Geosciences, Dept. of Geological Sciences, Austin TX, US

November 26, 2022

Abstract

The Himalayan orogen exposes a range of metamorphosed assemblages, from low-grade Indian shelf sediments of the Tethyan Formation to eclogite and ultra-high pressure rocks documented near the suture zone between the Indian craton and Asian subcontinent. Barrovian-grade pelites and mafic protoliths are exposed in the Himalayan core and include the Greater Himalayan Crystallines and Lesser Himalayan Formations. These units are separated by the Main Central Thrust (MCT). This fault system accommodated a significant amount of India-Asia convergence and is the focus of several models that explore ideas about the development of the range and collisional belts in general. These units provide critical information regarding the mechanisms of heat transfer within collisional belts. Garnets collected across the MCT record their growth history through changes in chemistry. These chemical changes can be extracted and modeled using a variety of thermodynamic approaches. This paper reviews the geological framework of the Himalayas with a focus on the protolith of its metamorphosed assemblages. It describes and applies particular thermobarometric techniques to decipher the metamorphic history of several garnet-bearing rocks collected across the MCT in central Nepal. Comparisons are made between the results of previously-reported conventional rim P-T conditions and P-T paths extracted using the Gibb's method to isopleth thermobarometry and high-resolution P-T path modeling using the same data and assemblages. Predictions of the paths on garnet zoning are also presented for the high-resolution P-T path modeling and Gibb's method using the program TheriaG. Although the approaches yield different absolute conditions and P-T path shapes, all are consistent with the development of the MCT shear zone due to imbrication of distinct rock packages. Greater Himalayan Crystalline garnets experienced higher-grade conditions that make extracting its P-T conditions and paths a challenge. Lesser Himalayan garnets appear to behave as closed systems and are ideally suited for thermodynamic approaches.

Records of Himalayan Metamorphism and Contractional Tectonics in the central Himalayas (Darondi Khola, Nepal)

E. J. Catlos

[1] The University of Texas at Austin, Jackson School of Geosciences, Dept. of Geological Sciences, Austin TX, US

Index terms

8110 Continental tectonics: general (0905)

8108 Continental tectonics: compressional

3660 Metamorphic petrology

3651 Thermobarometry

3652 Pressure-temperature-time paths

Keywords

Himalayas, Compression, Collision, Metamorphism, Thermobarometry

Abstract

The Himalayan orogen exposes a range of metamorphosed assemblages, from low-grade Indian shelf sediments of the Tethyan Formation to eclogite and ultra-high pressure rocks documented near the suture zone between the Indian craton and Asian subcontinent. Barrovian-grade pelites and mafic protoliths are exposed in the Himalayan core and include the Greater Himalayan Crystallines and Lesser Himalayan Formations. These units are separated by the Main Central Thrust (MCT). This fault system accommodated a significant amount of India-Asia convergence and is the focus of several models that explore ideas about the development of the range and collisional belts in general. These units provide critical information regarding the mechanisms of heat transfer within collisional belts. Garnets collected across the MCT record their growth history through changes in chemistry. These chemical changes can be extracted and modeled using a variety of thermodynamic approaches. This paper reviews the geological framework of the Himalayas with a focus on the protolith of its metamorphosed assemblages. It describes and applies particular thermobarometric techniques to decipher the metamorphic history of several garnet-bearing rocks collected across the MCT in central Nepal. Comparisons are made between the results of previously-reported conventional rim P-T conditions and P-T paths extracted using the Gibb's method to isopleth thermobarometry and high-resolution P-T path modeling using the same data and assemblages. Predictions of the paths on garnet zoning are also presented for the high-resolution P-T path modeling and Gibb's method using the program TheriaG. Although the approaches yield different absolute conditions and P-T path shapes, all are consistent with the

development of the MCT shear zone due to imbrication of distinct rock packages. Greater Himalayan Crystalline garnets experienced higher-grade conditions that make extracting its P-T conditions and paths a challenge. Lesser Himalayan garnets appear to behave as closed systems and are ideally suited for thermodynamic approaches.

1 Introduction

Nineteenth-century geologists studying the Himalayas perceived an anomalous geologic relationship that appeared to contradict two commonly accepted principles: the oldest rocks in a sedimentary succession are found at the base of the pile, and metamorphosed strata are older than unmetamorphosed. The Main Central Thrust (MCT), located at the base of the Himalayan break in slope, places lower-grade Lesser Himalayan Formation (LHF) metasediments beneath high-grade gneisses of the Greater Himalayan Crystallines (GHC) (Figure 1 and Figure 2). Exploration of the Himal Pradesh region in northern India surprised the pioneering geologists (Medicott, 1864; Oldham, 1883; Middlemiss, 1887) who saw the highest-grade, and thus supposedly oldest rocks, form the tallest peaks:

> "Now the belief which is at present so rapidly gaining ground that metamorphic strata are presumably older than unmetamorphosed strata makes one at first glance assume the strong probability in favor of the inner schistose series [Greater Himalayan Crystallines] being of much greater age than the outer zone of formations [Lesser Himalaya]. But no sooner has this a priori probability obtained a firm hold of the mind than a rude shock is given to it by the discovery that at every point round the schistose area the Outer formations appear to dip towards and under the schistose series at steep angles (50°-60°), whilst the schistose series itself is disposed apparently…upon the top of the Outer Formations, and culminating in a capping of gneissose rock on the summit of Kalogarhi mountain, the highest point in the neighborhood (Middlemiss, 1887)."

The recognition of widespread thrusting within the Himalaya was largely based on the observations (von Loczy, 1907; Pilgrim & West, 1928; Auden, 1937; Heim and Gansser, 1939) and the orogen's "inverted metamorphism," an increase in metamorphic intensity towards higher structural levels, appeared resolved by invoking compressional/contractional tectonics and the thrusting of the GHC unit on top of the LHF. However, future studies indicated that the kyanite isograd remained unbroken across the MCT, and its footwall is characterized by an inverted geotherm (Figure 3) (Ray, 1947; Gansser, 1964; LeFort, 1975; Pêcher, 1989; England et al., 1992). The idea of Himalayan inverted metamorphism reemerged but was relocated to the MCT footwall.

Inverted metamorphic gradients suggest the presence of wholly overturned strata or heat sources that counteract the influence of the asthenosphere (e.g., England & Molnar, 1993; Jamieson et al., 1996; Grasemann & Vannay, 1999; Kidder et al., 2013). The cause of the phenomenon has implications for establishing mechanisms of heat transfer within collisional belts and the role of heat sources, such as shear heating in fault zones, heat advection by magmas, radiogenic heating, and asthenospheric input. Inverted metamorphism has long been associated with areas of extensive thrust faulting, where heat is thought to flow from a hot upper plate to a colder lower plate (Ernst, 1973; Graham & England, 1976; Spear et al., 1995). Some models of Himalayan orogenesis link the apparently anomalous geothermal gradient spatially and temporally with motion along the MCT, whereas others suggest a juxtaposition of previously

metamorphosed sequences (Searle & Rex, 1989; Harrison et al., 1999; Hodges, 2000; Dasgupta et al., 2004; Larson et al., 2015).

The MCT has accommodated a significant amount of Indo-Asian convergence (e.g., Schelling & Arita, 1991; Yin & Harrison, 2000; Yin, 2006; Tobgay et al., 2012; Roberts et al., 2020), but other large-scale structures, including crustal-scale strike-slip faults to the north, active thrusts to the south, and the Main Himalayan Thrust (MHT) decollement compete for strain accommodation (Figure 2). The MCT has long been thought to be presently quiescent (Ye et al., 1981; Ni & Barazangi, 1984; Schelling & Arita, 1991; England et al., 1992). However, some earthquakes, like the 2015 Nepal (Gorkha) and 1991 Uttarkashi (Garhwal) events, challenge the notion, as their epicenters and epicenters of their aftershocks are modeled to zones within the LHF (Thakur & Kumar, 1994; Jain & Chander, 1995; Kayal, 1996; Gupta et al., 2015; Bai et al., 2016; Catlos et al., 2020). The MCT has also been linked to the generation of numerous geologic elements that characterize the Himalayan range, including hanging wall anatectic granitoids and crustal-scale extension found in association with the GHC (e.g., Burg et al., 1984; Valdiya, 1988; Burchfiel et al., 1992; Harrison et al., 1997; Kawakami et al., 2019).

Studies of the MCT hanging wall indicate the unit has discontinuities possibly related to internal structures (e.g., western Nepal, Carosi et al., 2010; Montomoli et al., 2013; Braden et al., 2017; central Nepal, Cottle et al., 2015; Wang et al., 2013; 2016; Rapa et al., 2018; Larson et al., 2015; Sikkim, Chakraborty et al., 2019; NW India, Iaccarino et al., 2020; Benetti et al., 2021; see discussions in Mukherjee et al., 2012; Larson et al., 2013; Montomoli et al., 2015). The nature of these cryptic discontinuities is unclear and could be due to unmapped faults or shear zones or inheritance of pre-existing basement structures (e.g., Cottle et al., 2015). Their presence enhances the complexity of the Himalayan orogenic system as their activity could have significantly disrupted geotherms within the GHC core during its exhumation. This is a scenario that is not accounted for in the channel flow model for the extrusion of the Himalayan core (e.g., Benetti et al., 2021; Maiti & Mandal, 2021). Understanding when Himalayan fault systems were active is critical for deciphering the processes involved during convergence.

The metamorphic history of the Himalayas has been the focus of sustained attention for almost seventy-five years (e.g., Ray, 1947). Garnet-bearing assemblages have long been using to test hypotheses proposed for the origin of MCT inverted metamorphism, understand the slip history of the MCT and the dynamics of Himalayan convergence. The focus includes generating the peak pressure-temperature (P-T) conditions and paths that rocks followed as they were metamorphosed during Indo-Asia collision (e.g., Brunel and Kienast, 1986; Hodges et al., 1988; Hodges and Silverberg, 1988; Hubbard, 1989; Inger and Harris, 1992; Hodges et al., 1993; Metcalfe, 1993; Pognante and Benna, 1993; Kaneko, 1995; Macfarlane, 1995; Coleman, 1996; Vannay and Hodges, 1996; Vannay and Grasemann, 1998; Manickavasagam et al., 1999; Catlos et al., 2001; Kohn et al., 2001; Kohn, 2008; Phukon et al., 2019; Waters, 2019; Iaccarino et al., 2020; Catlos et al., 2018; 2020).

As a universal outcome, models for the development of the Himalayas predict the P-T paths that rocks follow as they track the conditions they experienced during displacement. Common approaches to generate Himalayan P-T paths have included connecting peak metamorphic conditions of individual rocks, inferring from mineral assemblages, pseudosections, or Gibbs method thermodynamic modeling. Some rocks yield problematic P-T estimates based on (1) a lack of evidence of phases in equilibrium among phases, (2) the application of barometers to inappropriate (uncalibrated) mineral compositions, and (3)

calculated conditions that appear at odds to observed mineral assemblages and structural data (e.g., Kohn & Spear, 2000; Kohn, 2008). P-T paths and absolute peak P-T conditions may not be diagnostic of tectonic processes involved (e.g., Gervais & Brown, 2011). Low-resolution P-T paths can be limited in their ability to test ideas regarding lithospheric response to perturbations, including motion within fault zones. However, this type of information can be used to supplement other data, such as the timing of deformation or strain recorded in microstructures (see Kohn, 2016; Rolfo et al., 2014).

This paper has two goals. The first is to review the geological framework of the Himalayas with a focus on the protolith of its metamorphosed assemblages. The second is to describe and apply particular thermobarometric approaches to decipher the metamorphic history of garnet-bearing rocks collected from the central portion of the range across the MCT using data published in the literature (Darondi Khola, Figure 3, Figure 4, Figure 5) (Kohn et al., 2001). A range of approaches are available to obtain P-T and time garnet growth (P-T-t data) (see review by Waters, 2019). The Darondi Khola case study compares conventional and isopleth thermobarometry in terms of their outcomes and insights and presents new P-T paths from metamorphosed garnet-bearing rocks using previously collected data. Garnet-bearing pelitic assemblages exposed in units across the Himalayas contain information regarding their history that can be extracted and applied to test models developed to decipher the crustal response during orogeny.

2 Geological Background

The Himalayan arc extends ~2400 km from Nanga Parbat (8138 m) in the west to Namche Barwa (7756 m) in the east (e.g., Le Fort, 1996) (Figure 1 and Figure 2). This region includes the independent kingdoms of Nepal and Bhutan and parts of Pakistan, India, and China. The orogen forms a sharp transition between the average ~5 km-high, arid Tibetan plateau and the warmer, wetter Indian lowlands and is comprised of roughly parallel, crustal-scale fault systems that bound distinctive lithologic units along strike (DiPietro & Pogue, 2004; Yin, 2006). These units have Indian affinity and experienced variable degrees of metamorphism before their assembly with Asia.

2.1 Geological framework before collision

The Indian subcontinent initiates rifting from other continents and fragments associated with Gondwana during the Early Cretaceous (140-130 Ma, e.g., Scotese et al., 1988; Jadoul et al., 1998; Hu et al., 2010). Evidence for Early Cretaceous rift- and plume-related alkaline and basaltic volcanism exists within the LHF, which extends the entire length of the Himalayas, and is the oldest stratigraphically lowest unit (e.g., Sakai et al., 2013; Bhandari et al., 2019). The LHF is considered the MCT footwall and Main Boundary Thrust (MBT) sheet (Figure 1 and Figure 2) (Dey et al., 2020). It is mainly comprised of Paleoproterozoic Gondwana-associated sediments that experienced deposition and granite intrusion centered around 1800 Ma (e.g., Trivedi et al., 1984; Tripathi & Singh, 1987; Parrish & Hodges, 1996; Miller et al., 2000; DeCelles et al., 2004; Kohn et al., 2010; Martin et al., 2011; McKenzie et al., 2011; Long et al., 2011; Sakai et al., 2013; Khanal et al., 2014; Mandal et al., 2016). The depositional environment is a passive-margin, shallow-water coastal, fluvial, volcanoclastic (e.g., Parrish & Hodges, 1996; Ahmad et al., 1999; Martin et al., 2011; Sakai et al., 2013; Bhandari et al., 2019). However, the lower section of the LHF may have formed in a continental arc on the northern margin of the Indian plate (Kohn et al., 2010; Mandal et al., 2016). In some locations, rift-related alkaline

trachytic lava and pillow-bearing volcanic rocks are interbedded with pebble conglomerates and black shales, and signatures of significant asthenosphere upwelling are evident using geochemical proxies (e.g., Ahmad et al., 1999; Larson et al., 2019; Bhandari et al., 2019).

The stratigraphic classification of the Proterozoic succession of Lesser Himalaya is yet to be defined following the Code of Stratigraphic Nomenclature, and orogen-scale correlations along strike are hindered by uncertainties (Myrow et al., 2006; Long et al., 2011; Mandal et al., 2016; Dey et al., 2020). Sedimentation was long-lasting, but a lack of fossiliferous assemblages makes correlating specific units problematic (Upreti, 1999; Martin et al., 2011; Long et al., 2011). Detrital zircon geochronology and stable isotopic analysis of suitable assemblages assist in this regard (e.g., Long et al., 2011; Martin et al., 2011; Sakai et al., 2013). A series of augen gneisses (the Melung Salleri or Phaplu Augen Gneiss of eastern Nepal and NW India, the Ulleri of central Nepal, or Chainpurplay in western Nepal) distinguish different levels of the MCT shear zone and LHF stratigraphy (Figure 3, Figure 4, Figure 5) (Kohn et al., 2010; Dyck et al., 2019; Jharendra & Paudyal, 2019). These gneisses have ages from 2.2 Ga to 900 Ma (e.g., Le Fort & Rai, 1999; DeCelles et al., 2000; Catlos et al., 2002; Kohn et al., 2010) and define the base of the MCT shear zone in some interpretations. A Permian-Cambrian unconformity is recognized in NW India, Nepal, and Bhutan (e.g., Bhargava et al., 2011; Martin et al., 2011; Long et al., 2011). Some have related its presence and Cambro-Ordovician granites found in GHC and LHF units to a pre-Tertiary orogeny (Gehrels et al., 2003; 2006; Cawood et al., 2007; Bhargava et al., 2011).

The GHC protolith is a clastic sedimentary sequence intruded by Cambro-Ordovician granitoids (e.g., Trivedi et al., 1984; Bhargava & Bassi, 1994; Parrish & Hodges, 1996; Upreti & Le Fort, 1999; DeCelles et al., 2004; Dyck et al., 2019). The depositional age is bracketed between the age of the youngest detrital zircons (~800-600 Ma) and granite intrusions (~500-460 Ma) (Ahmad et al., 2000; DeCelles et al., 2000; DeCelles et al., 2004; Martin et al., 2005; Dyck et al., 2019). Whole-rock Nd isotopes distinguish GHC [εNd(0) -19 to -12, average -16] from LHF affinities [εNd(0) -20 to -26, average -21.5] (Robinson et al., 2001; Martin et al., 2005). The GHC detrital zircons may have originated from the East African portion of the Pan-African orogeny (Arabian-Nubian Shield), uplifted during the Neoproterozoic (DeCelles et al., 2000; 2004), or from the late Mesoproterozoic terranes of Western Australia and East Antarctica (Circum-East Antarctic Orogen, Upreti & Yoshida, 2005; Yoshida & Upreti, 2006). The GHC has been modeled as unconformably deposited on the LHF (Parrish & Hodges, 1996) or tectonically juxtaposed (Upreti & Le Fort, 1999; DeCelles et al., 2000). The similarity in Cambrian ages between the LHF and GHC suggest they may be part of a shared depositional environment, with the LHF as proximal and the GHC as distal (Brookfield, 1993; Parish & Hodges, 1996; Corfield & Searle, 2000; Myrow et al., 2003; Myrow et al., 2006; Long et al., 2011). Alternatively, the GHC may have been a distinct basement unit separating the LHF from the Tethyan metasediments (Saxena, 1971; Aharon et al., 1987) or an exotic terrane involved in a pre-Himalayan collision (DeCelles et al., 2000; Gehrels et al., 2003).

Tethyan sedimentary and metasedimentary rocks are bounded to the north by the Indus Yarlung-Tsangpo suture zone (also Yarlung Zangbo Ophiolite Zone, Liu et al. 2010) (Gansser, 1964; Dewey & Bird, 1970; Burg et al., 1984; Yin et al., 1994; Quidelleur et al., 1997; Zhang et al., 2004; Yin, 2006; Zyabrev et al., 2008), and to the south by the GHC or South Tibetan Detachment System (STDS) (Figure 1 and Figure 2) (e.g., Makovsky & Klemperer, 1996; Wu et al., 1998; Searle, 2010; Long et al., 2017; Montomoli et al., 2017; Hughes et al., 2018; Kellett et

al., 2018; Long et al., 2019). The Great Counter Thrust (or the Renbu-Zedong Thrust or Himalayan Backthrust) is mapped south of the zone also works to accommodate crustal shortening (Yin et al., 1999; Yin, 2006; Aikman et al., 2008). The Tethyan unit has long been considered as a contiguous stratigraphic cover of the GHC (Bodenhausen et al., 1964; Bordet et al., 1971; Stöcklin, 1980; Garzanti & Pagni Frette, 1991; Brookfield, 1993; Liu & Einsele, 1994; Fuchs & Linner, 1995; Vannay & Steck, 1995; Garzanti, 1999; Dyck et al., 2019), and the suture zone marks the geological boundary separating rocks of Indian and Asian affinity (e.g., Gansser, 1981; Yin & Harrison, 2000). In NW India, the Tethyan Formation may be in thrust contact with the LHF (Webb et al., 2007). The Tethyan Formation consists of Paleoproterozoic to Eocene Indian shelf sediments (marine, fossiliferous strata) interbedded with Paleozoic and Mesozoic volcanic assemblages (Bassoullet et al., 1980; Brookfield, 1993; Yin, 2006; Bhargava & Singh, 2020). The unit has been divided into four sequences: a Proterozoic to Devonian pre-rift, a Carboniferous–Lower Jurassic rift and post-rift, Jurassic–Cretaceous passive continental margin sequence, and an uppermost Cretaceous–Eocene syn-collision sequence (Liu & Einsele, 1994; Garzanti, 1999; Yin, 2006). Tethyan Formation lithostratigraphy changes both along and perpendicular to the Himalayan orogeny (Brookfield, 1993; Yin, 2006). In some locations, the unit has undergone pre-Himalaya low-grade to greenschist facies metamorphism (e.g., Crouzet et al., 2007; Dunkl et al., 2011; Montomoli et al., 2017) and the latest Cretaceous to Paleocene sequence of the formation records the obduction of ophiolitic material (Allègre et al., 1984; Burg et al., 1987; Willems et al., 1996; Gnos et al., 1997; Makovsky et al., 1999; Aitchison et al., 2000; Ding et al., 2005).

2.2 Timing of major metamorphic events and fault systems

2.2.1 Collision and metamorphism in the Tethyan Formation

The Indian subcontinent moves over 60° latitude north towards Asia during the mid-Mesozoic to Eocene, closing the ancient Neo-Tethyan Ocean (e.g., Burg, 2011). The Early Cretaceous (140-130 Ma) is often cited as the time when the Indian subcontinent initiates rifting from other continents and fragments associated with Gondwana (e.g., Scotese et al., 1988; Jadoul et al., 1998; Hu et al., 2010). Remnants of Neo-Tethyan ophiolites are present across the Himalayas and provide information regarding the timing and processes involved during Indo-Asia collision and the nature of Neo-Tethyan ocean crust and upper mantle (e.g., Hébert et al., 2012; Hu et al., 2016; Catlos et al., 2019). Based on data from these ophiolites, a Late Cretaceous intra-oceanic arc has been suggested to be present within the Neo-Tethyan Ocean near the paleo-equator (e.g., Reuber, 1986; Abrajevitch et al., 2005; Metcalfe, 2009; Dai et al., 2011; Siddiqui et al., 2012; Siddiqui et al., 2017) or ~30°N (Zhu et al., 2013). The arc is recorded by the Samail (Oman), Zagros (Iran), Chagai–Raskoh (western Pakistan, southern Iran, eastern Afghanistan), Kandahar and Kohistan–Ladakh, Dazhuqu, and Zhongba arcs (Brookfield and Reynolds, 1981; Bhutani et al., 2004; Abrajevitch et al., 2005; Dai et al., 2011; Siddiqui et al., 2012; Baxter et al., 2016). Paleogeographic reconstructions of Lawver et al. (2018) restrict the location of the intra-oceanic arc to the south of the Lhasa Terrane, although others suggest the Lhasa Terrane had already accreted onto other Tibetan-related continental fragments by the Late Jurassic-Early Cretaceous (Rolland, 2002; Kapp et al., 2003, 2007; Guynn et al., 2006; Zhu et al., 2013). Alternatively, the Lhasa Terrane accreted just before the final collisional event in the Paleocene (54.9±2.3 Ma and 40.0±3.3 Ma; Yang et al., 2015; 61 Ma and ~53-48 Ma; Yuan et al., 2020). Multiple arcs, besides the Lhasa Terrane, may also have been present (e.g., Zyabrev et al., 2008). The oldest portion of the Neo-Tethyan domain is Late Triassic to Late Cretaceous (Sinha-

Roy, 1982; Şengör and Atayman, 2009; Cao et al., 2018) and is sometimes termed the Ceno-Tethyan Ocean (Metcalfe, 1999; Matsuoka et al., 2002; Wakita and Metcalfe, 2005). The Yarlung-Tsangpo suture zone itself is mapped as the zone of the closure of the Ceno-Tethyan Ocean (e.g., Metcalfe, 1999; 2009; 2013).

The timing of initial collision varies along strike of the range but is often cited as during the Paleocene (Patriat & Achache, 1984; Klootwijk et al., 1992; Rowley, 1996; Yin & Harrison, 2000; Najman et al., 2001, 2002, 2003; Zhu et al., 2005; Ding et al., 2005; Yang et al., 2015; Hu et al., 2016). Much younger constraints are also suggested (e.g., Eocene/Oligocene boundary, Aitchison et al., 2007) and a division between a soft (Paleocene) and hard collision (25-20 Ma, van Hinsbergen et al. 2012; see review in Parsons et al., 2020). In the hard scenario of Indo-Asia collision, the Tethyan unit represents the northern extension of the Indian subcontinent (Brookfield, 1993; Yin & Harrison, 2000; Myrow et al., 2003, Hughes et al., 2005; Myrow et al., 2009; Myrow et al., 2015; Hughes, 2016). Others suggest the Tethyan formation may have been an independent terrane in the Mesozoic (DeCelles et al., 2000; see review in Yuan et al., 2020). Parsons et al. (2020) note that little progress has been made to resolve the differences between models of Indo-Asia collision. Gehrels et al. (2003) indicates that ascertaining the relative contributions of early Paleozoic versus Tertiary tectonism poses a significant challenge in understanding the Himalayan orogen. To understand which model is relevant requires understanding the metamorphic and timing history of fault systems that were active during collision. The Great Counter Thrust, which bounds the upper portion of the Tethyan Formation along much of its strike (Figure 1), is significantly younger than the Paleocene ages of Indo-Asia collision. This structure shows activity primarily during the Miocene (20-13 Ma) across the western and central Himalayas (see review in Yin, 2006).

Compilations regarding the Tethyan Formation's metamorphic history collected along strike suggest the Tethyan sequences have experienced multiple (4-5) deformation events, although the timing of these episodes is poorly constrained (Aikman et al., 2008; Dunkl et al., 2011). Studies focusing on the low-grade history reveal Early Cretaceous pre-collisional metamorphism (e.g., Crouzet et al., 2007; Dunkl et al., 2011). Eocene greenschist to amphibolite facies metamorphism is recorded in portions of the unit and record conditions likely related to the onset of collision (580-600°C, 5-8 kbar) (Dunkl et al., 2011; Catlos et al., 2020). Paleocene radiometric ages related to collision are found in the Spongtang ophiolite (Figure 1) (64.3±0.8 Ma and 42.4±0.5 Ma, zircon U-Pb ages, Catlos et al., 2019) and in a Tethyan Formation garnet (50.3±0.6 Ma; Catlos et al., 2020). The collisional event is also recorded by eclogite, high-pressure (HP) and ultra-high pressure (UHP) rocks documented within the Tethyan Formation near the suture zone (e.g., Guillot et al., 2008; Laskowski et al., 2016). In some locations, HP assemblages record multiple metamorphic stages (e.g., Chen et al., 2021). Oligo-Miocene anchi- to epizonal metamorphism and alteration are related to crustal shortening during this time, whereas rocks at the base of the unit record Miocene STDS motion and gneiss dome exhumation (e.g., Dunkl et al., 2011). Oligocene- to Miocene-age contact metamorphism marks the onset of the intrusion of some North Himalayan granitic bodies and gneiss domes (e.g., Guillot et al., 1995, 1999; Liu et al., 2016; Gao et al., 2016; Lihter et al., 2020). The onset of the north-dipping STDS and its associated imbrications (Figure 1) is often constrained to the Miocene (Carosi et al., 1998, 1999a, 1999b; Searle, 1999; Sachan et al., 2010; Iaccarino et al., 2017; Long et al., 2017; Montomoli et al., 2017; Kellett et al., 2018; Iaccarino et al., 2020). However, at some locations, the GHC shows a transitional relationship with limestone of the Tethys sediments and metamorphic grade remains unchanged across the STDS with stratigraphy and lithology

excluding a distinct fault boundary (e.g., Bordet et al., 1975; Stöcklin, 1980; Fuchs et al., 1988; Schneider & Masch, 1993; Vannay & Steck, 1995; Cooper et al., 2012; Long et al., 2017). Long et al. (2019) suggest that extensional motion associated with the STDS in Bhutan occurs both within the GHC and Tethyan units.

2.2.2 The GHC Eohimalayan and Neohimalayan events

The GHC is mainly comprised kyanite- to sillimanite- grade gneisses intruded by High Himalayan leucogranites in structurally higher levels (e.g., Upreti, 1999; Searle et al., 2006; Sachan et al., 2010; Wu et al., 2020). The GHC is generally divided into different units, although the assemblages that comprise its sections differ along strike (Le Fort, 1975; Myrow et al., 2003; Yin, 2006). In central Nepal (Guillot, 1999), the upper Formation III consists of augen orthogneisses, whereas the middle Formation II are calc-silicate gneisses and marbles, and the basal Formation I are kyanite- and sillimanite-bearing metapelites, gneisses, and metagreywackes with abundant quartzite. The division of the package into three units mirrors the nomenclature ~250 km east (Lombardo et al., 1993; Pognante & Benna, 1993; Carosi et al., 1999a), although the assemblages differ from that of central Nepal. In eastern Nepal, the upper Black Gneiss is comprised of biotite-sillimanite paragneisses with metaconglomerates and quartzite layers. The middle Namche Migmatite Orthogneiss contains granite-granodiorite sillimanite-bearing orthogneisses. The Barun Gneiss at the base is a migmatized paragneiss with minor metabasites, calc-silicate rocks, and marbles. In the Garhwal Himalaya, the Vaikrita Group is the analog to the GHC (e.g., Ahmad et al., 2000). Early observations, the unit's complex metamorphic history, and possibility of out-of-sequence thrusting at higher levels led Stöcklin (1980) to doubt the assumption of a three-tiered, laterally-continuous, tectonostratigraphic framework. More recent thermobarometric data and P-T-t paths from garnet-bearing assemblages from the GHC unit indicate the unit itself has discontinuities related to internal structures that overlap in age with MCT motion (Carosi et al., 2010; Montomoli et al., 2013; Wang et al., 2013; Larson et al., 2015; Montomoli et al., 2015; Carosi et al., 2016; Wang et al., 2016; Braden et al., 2017; Rapa et al., 2018; Chakraborty et al., 2019; Benetti et al., 2021).

A Tertiary history involving two metamorphic episodes has been proposed for the GHC (see Pêcher & Le Fort, 1986; Metcalfe, 1993; Pognante & Benna, 1993; Wiesmayr & Grasemann, 2002; Carosi et al., 1999b; Lombardo & Rolfo, 2000; Hodges, 2000; Wiesmayr & Grasemann, 2002; Cottle et al., 2009; Kohn, 2014; Robyr & Lanari, 2020). The first stage (Eocene-Oligocene) of Barrovian-type metamorphism, termed the Eohimalayan event, corresponds to the nappe's burial beneath Asia and is best preserved near the base of the unit (e.g., Pêcher, 1989; Hodges et al., 1994; Wiesmayr & Grasemann, 2002). During this stage, the base of the unit reached garnet-grade conditions (550-750□C and at least 8-10 kbar, e.g., Pognante & Benna, 1993; Hodges et al., 1994). Thrusting may have been accommodated by a fault system considered a proto-STDS that reactivated as a normal fault during the second stage in the Miocene (e.g., Vannay & Hodges, 1996; Wiesmayr & Grasemann, 2002; DiPietro & Pogue, 2004). The locations where this scenario has been proposed show mylonitic contractional fabrics overprinted by extensional structures and include the Himachal Pradesh, NW India (Vannay & Grasemann, 1998), Zanskar, NW India (Patel et al., 1993), and the Kali Gandaki, central Nepal (Vannay & Hodges, 1996). Note that even earlier events may have preceded Himalayan orogenesis and can be challenging to distinguish from Cenozoic tectonics (see Gehrels et al., 2003).

The Eohimalayan event occurred between 50-35 Ma coincides with a dramatic decrease in convergence rate between India and Asia from ~15 to ~4 cm/yr (Copley et al., 2010). During the Miocene Neohimalayan event, the base of the GHC experienced 550-600□C and the top records lower pressures and/or temperatures (3-7 kbar, 575-850□C) (e.g., Hodges et al., 1994; Simpson et al., 2000; Daniel et al., 2003). The Neohimalayan event has been associated with MCT slip and with the development of Miocene-age High Himalayan leucogranites found in close association with STDS (Pêcher, 1989; Harris et al., 1993; Metcalfe, 1993; Hopkinson et al., 2017; Liu et al., 2018; Yang et al., 2019; Wu et al. 2020).

The duration and onset of MCT movement varies along strike and is often attributed sometime during the Miocene. To time fault activity, monazite [(Ce, La,Th)PO4] is often targeted, a mineral that appears in these rocks at garnet grades and is ideal for timing metamorphism (e.g., Catlos, 2013). In western Bhutan, the duration of MCT displacement is bracketed by monazite ages between 20.8±1.1 and 15.0±2.4 Ma (Togbay et al., 2012). However, in eastern Bhutan, prograde metamorphism and deformation is reported to have been underway along the structure by c. 23 Ma (Daniel et al., 2003). Monazite ages from the lower portions of the GHC in western Nepal yield younger ages timed to fault motion at 17-13 Ma (Montomoli et al., 2013). Depth profiling of unpolished monazite indicate that the MCT hanging wall was deforming in central Nepal between 24-22 Ma (Harrison et al., 1995). The 22 Ma age is also attributed to MCT activity in central Nepal (Hodges et al., 1996; Coleman & Hodges, 1998)

In NW India (Garhwal region), the MCT shear zone is thought to be active from 20 Ma to 5 Ma (Iaccarino et al., 2020) or even younger to 1 Ma (Catlos et al., 2007; 2020). Mukhopadhyay et al. (2017) suggest activity on the MCT itself in the Sikkim region occurred in pulses over an extended period of time from 26 to 11 Ma. Monazite grains from the MCT shear zone in the Sikkim indicate the structure was active at c. 22 Ma, 14-15 Ma, and 12-10 Ma (Catlos et al., 2007) and from 21-13 Ma (Mottram et al., 2014). Younger ages are attributed to structures south of the GHC-LHF contact, and are often found at lower structural levels within the shear zone elsewhere. For example, Figure 5 shows the distribution of in situ secondary ion mass spectrometry (SIMS) Th-Pb monazite and muscovite $^{40}Ar/^{39}Ar$ total gas ages along the Darondi Khola (Catlos et al., 2001). The oldest early Miocene monazite ages are found in upper LHF units (21.7±1.2 Ma to 21.1±0.8 Ma), but they decrease towards lower structural levels to 7.6±0.2 Ma to 6.9±0.5 Ma. In Arun valley of eastern Nepal Himalayas, Oligocene activity within the upper portions of the MCT shear zone has been reported (~31 Ma, Groppo et al., 2010). Late Eocene to Oligocene monazite ages have been found in GHC samples from central Nepal (37.6±3.8 Ma to 30.4±0.5 Ma, Catlos et al., 2001; see also Gibson et al., 2016 for the same transect) and NW India (37.9±0.9 Ma to 34.3±0.8 Ma, Catlos et al., 2007). The Oligocene ages are consistent with the events related to the Eohimalayan time frame of Himalayan orogenesis and may not be related to activity along the MCT.

Distinguishing between the Eohimalayan and Neohimalayan events is challenging, and the Eohimalayan event may only be recorded in GHC and Tethyan units in particular locations (Aikman et al., 2008; Stickroth et al., 2019). North-east verging folds of the Tethys Formation may have developed during the Eohimalayan event (e.g., Godin et al. 1999a, 1999b), whereas these and others reported in the GHC (Bhargava & Bassi, 1994; Carosi et al., 1999b) may be the result of gravity sliding along the STDS (e.g., Burchfiel et al., 1992; Hodges et al., 1996; Vannay & Hodges, 1996; Searle, 2010). Large-scale folding that aligns preexisting isograds into an apparent inverted metamorphic position was attributed as a significant factor in the metamorphic

history of the GHC (Searle & Rex, 1989). In a petrochronology study of GHC monazite-bearing assemblages, Gibson et al. (2016) suggest that Eocene-Oligocene monazite ages represent prograde burial, which was followed by Miocene retrograde metamorphism and Miocene-Pliocene exhumation. Wu et al. (2020) suggest the High Himalayan leucogranites can be classified as Eohimalayan (46-25 Ma), Neohimalayan (25-14 Ma), and post-Himalayan (<14 Ma) based on their relationship with particular detachment systems, ages, and compositions. Some North Himalayan granites that intrude Indian shelf sediments are similar in age to their post-Himalayan stage (Harrison et al., 1997; 1998; Lee et al., 2004; Zhang et al., 2004).

2.2.3. Metamorphism in the LHF

At their base, the GHC is thrust over Middle Proterozoic phyllites, metaquartzites, and mylonitic augen gneisses of LHF along the broad-scale 8-12 km thick MCT shear zone (Le Fort, 1975; Gansser, 1981; Arita, 1983; Brunel & Kienast, 1986; Pêcher, 1989; Searle & Rex, 1989; England et al., 1992; Schelling, 1992; Le Fort, 1996; Henry et al., 1997; Harrison et al., 1998; Kohn et al., 2004; Bollinger et al., 2006; Carosi et al., 2013; Parsons et al., 2016; Martin, 2017a,b; Mukhopadhyay et al., 2017; Yin & Harrison, 2000; Catlos et al., 2001; Catlos et al., 2018; 2020). The onset of MCT activity occurred during the early Miocene (Pêcher, 1991; Vannay et al., 2004; Yin, 2006), at a time when Indo-Asia convergence slows (>40% between 20-10 Ma, Molnar and Stock, 2009) and had a significant impact on the extrusion of the GHC orogenic wedge (Maiti et al., 2020). The MCT fault system plays a central role in many models for the evolution of the Himalayas (e.g., Le Fort, 1975; Searle & Rex, 1989; England et al., 1992; Henry et al., 1997; Harrison et al., 1998; Bollinger et al., 2006; Kohn, 2008; Carosi et al., 2013; Beaumont et al., 2001; 2004; Jamieson et al., 2004; 2006; Searle et al., 2006; Long & McQuarrie, 2010; Wang et al., 2013; Cottle et al., 2015).

Lack of an apparent break in metamorphic grade between the GHC and LHF makes the placement of the boundaries of the MCT shear zone difficult to discern. Definitions of the structure center around age, metamorphic history, rheology, and role as separating units of different depositional environments (see Martin, 2017a). As the GHC and LHF evolved in different depositional environments, geochemical and geochronological evidence aids in its placement (e.g., Parrish & Hodges, 1996; Ahmad et al., 2000; Martin, 2017a,b; Khanal et al., 2014). The original Pêcher (1989) MCT definition involved three criteria in identifying the MCT in the field: (1) the boundary between hanging wall gneisses and upper carbonate-rich formations of the Lesser Himalaya, (2) where Lesser Himalaya shear fabric (L-S) is replaced by the flattening fabric of the Greater Himalayan Crystallines, and (3) where the rotational deformation that increases progressively through the Lesser Himalaya reaches a maximum. In central Nepal, Arita (1983) places two thrusts (MCT-I and MCT-II) on each side of the MCT shear zone. The MCT-II corresponds to that described by Pêcher (1989), whereas the MCT-I separates a mylonitic augen gneiss from other Lesser Himalaya metasedimentary rocks. The MCT-I correlates to the Ramgarh Thrust, which accommodates the Ramgarh Thrust sheet within the LHF duplex (DeCelles et al., 2001; Robinson et al., 2003; Pearson & DeCelles, 2005; Robinson et al., 2006; Matin and Mukul, 2010; Khanal et al., 2014; Mandal et al., 2015). Some researchers do not recognize the MCT-I anywhere in the Nepal Himalaya (see Upreti, 1999). Along the Dudh Kosi-Everest transect, the MCT corresponds to the contact between the GHC gneisses and the upper LHF pelitic schists, whereas the MCT-I separates the mylonitic Phaplu augen gneiss from low-grade Lesser Himalaya metasedimentary rocks. Along the Bhagirathi River, Garhwal region, the Vaikrita Thrust (=MCT) and Munsiari Thrust (=MCT-I) bound the MCT shear zone,

but no equivalent to the Phaplu augen gneiss is exposed (e.g., Valdiya, 1980; Pêcher, 1991; Metcalfe, 1993; Searle et al., 1993; Ahmad et al., 2000; Singh & Thakur, 2001).

The MCT footwall is characterized and defined by inverted metamorphism, where metamorphic grade increases toward structurally shallower levels (e.g., Ray, 1947; Pêcher, 1989; Larson et al., 2015; Chakraborty et al., 2016; Searle et al., 2008; Iaccarino et al., 2020). Understanding the origin this phenomenon has implications for establishing the role of various crustal heat sources and mechanisms of heat transfer within collisional belts (e.g., radiogenic, asthenospheric input, shear heating, addition of melts) (e.g., England et al., 1992) and is facilitated by obtaining metamorphic P-T conditions and paths from shear zone garnet-bearing assemblages (Stäubli, 1989; Metcalfe, 1993; Kaneko, 1995; Vannay & Hodges, 1996; Vannay & Grasemann, 1998; Manickavasagam et al., 1999; Kohn et al., 2001; Catlos et al., 2001; Imayama et al., 2010; Corrie et al., 2010; Larson et al., 2013; Anczkiewicz et al., 2014; Kohn, 2014; Mottram et al., 2014; Mukhopadhyay et al., 2017; Catlos et al., 2018; Waters, 2019; Catlos et al., 2020).

The MCT has also been considered to be an expression of the Main Himalayan Thrust (MHT) (Bollinger et al., 2004; Mahajan et al., 2010), a pervasive décollement that separates the downgoing Indian plate from the Himalayan orogenic wedge (Figure 2) (Bilham et al., 1997; Nelson et al., 1996; Subedi et al., 2018; Zhao et al., 1993). Other surface expressions of the MHT include the MBT and Main Frontal Thrust (MFT) (Figure 1 and Figure 2). The STDS may be a local phenomenon, occurring when the Tethys dissociated from the GHC and slid along N-dipping planes due to gravity following uplift (e.g., Pêcher & Le Fort, 1986; Fuchs, 1987), although some models for channel flow connect this fault system to the MHT (e.g., Beaumont et al., 2001; 2004; Jamieson et al., 2004; 2006). The MHT is one of the largest and fastest slipping continental megathrusts on Earth (e.g., Duputel et al., 2016; Rajendran et al., 2017; Searle et al., 2017). Understanding its geometry, history, and fault systems that splay into the structure has implications for assessing and predicting the initiation, propagation, and termination of major event Himalayan earthquakes (e.g., Wang et al., 2017). The topography of the MHT is uncertain (e.g., Caldwell et al., 2013; Denolle et al., 2015; Elliott et al., 2016; Hazarika et al., 2017; Hubbard, 2016; Nábělek et al., 2009; Whipple et al., 2016; Wang et al., 2017; Zhou et al., 2019), due in part to the lack of recognition that fault systems within the LHF duplex or MCT shear zone have the potential to accommodate present-day slip (Catlos et al., 2020). The LHF duplex has long been known to be a ~50-km-wide seismogenic zone of predominately moderate earthquakes (Bai et al., 2016; Cattin & Avouac, 2000; Khattri & Tyagi, 1983; Mahajan et al., 2010). Bai et al. (2016) suggest that a thrust system within the LHF is the most seismically active region in the Himalayas and accommodates most of its elastic strain accumulation. Alternatively, the shallower events are explained by a segmented MHT that includes a ramp (He et al., 2018; Hubbard, 2016; Pandey et al., 1995).

2.2.4 The MBT and MFT

South of the MCT, the MBT separates the Lesser Himalaya from Neogene molasse, the Siwalik Formation (Figure 1) (Valdiya, 1992; Meigs et al., 1995; Mukul, 2000; Thakur et al., 2010; Goswami & Deopa, 2017; Dhamodharan et al., 2020). South of the MBT, the MFT is the boundary between the Siwalik Formation and the northern Indo-Gangetic Plains (e.g., Mugnier et al., 1999; Mukul et al., 2007; Burgess et al., 2012; Bollinger et al., 2014). The MBT has few timing constraints, but is primarily thought to have been initiated during the Late Miocene (13-10 Ma, Meigs et al., 1995; Chirouze et al., 2012; Patra & Saha, 2019), although it may have been

active since 5 Ma in Nepal (DeCelles et al. 2020). The Siwalik formation overall is a 7-10 km-thick succession of dominantly fluvial sedimentary rocks located along the entire length of the Himalaya from the Potwar plateau to the Brahmaputra in the east, likely due to the evolution of the Ganga river system (Bora and Shukla, 2005; Sanyal & Sinha, 2010; Khan et al., 2019; Dhamodharan et al., 2020). The Siwalik unit itself is divided into several sectors due to lineaments related to normal faulting in the Indian basement that reactivated as thrust faults during Himalayan collision (Raiverman et al., 1983; Dubey, 1997; Sanyal & Sinha, 2010). The Siwalik formation records key information regarding Himalaya erosional history, paleoclimate, transitions in paleobotany, and exhumation rates (e.g., Quade et al., 1989, 1995; Acharya, 1994; Najman et al., 2009; Sanyal & Sinha, 2010; Najman et al., 2017; Ghosh et al., 2018; Khan et al., 2019). In some locations, the MBT has nearby active steep faults that show normal or strike-slip senses of motion as they accommodate a critical taper (Mugnier et al., 1994; Patra & Saha, 2019). The MFT cuts Siwalik strata in places and is often manifested as growing anticlines (Yeats et al., 1992; Powers et al., 1998; Srivastava et al., 2018). These crustal-scale faults sole into the MHT (Figure 2) (Zhao et al., 1993; Nelson et al., 1996).

3. Models for the extrusion of the Himalayan core

The MCT fault system has long played a central role in models for the evolution of the Himalaya. Initial models presume that activity along the MCT only occurred during the Early Miocene (Figure 6) (Le Fort, 1975; Searle & Rex, 1989; Hubbard, 1996; England et al., 1992; Hodges et al., 1993; Harris & Massey, 1994). LeFort (1975) conceived that the inverted metamorphism in the LHF footwall was caused by the transfer of thermal energy due to large-scale underthrusting of the LHF beneath the GHC (the “Hot-Iron model” Figure 6A). In this scenario, fluids released from the MCT footwall migrate through the hanging wall and flux a leucogranite belt. The alternative was proposed by Hubbard (1996), in which the inverted mineral isograds result from ductile shearing a pre-existing zone of right-way-up metamorphism (Figure 6B). Searle and Rex (1989) delegated a significant role to STDS and suggested that the present-day distribution of metamorphic facies and leucogranite bodies are caused by overprinting earlier isograds during MCT-related anatexis and folding (Figure 6C). Fluids released from the MCT footwall assist with the formation of leucogranite. The STDS has appeared prominently in almost every model since. Hodges et al. (1993) proposed that the wedge GHC extruded via synchronous STDS and MCT movement (Figure 6D), and Harris & Massey (1994) suggested extensional collapse led to rapid GHC exhumation and decompression melting of kyanite-bearing schists that led to melts emplaced near the STDS (Figure 6E).

As more data became available, more numerical solutions and quantitative models appeared (Figure 7). Molnar and England (1990) matched P-T conditions obtained by Hubbard (1996) by solving a one-dimensional time-dependent heat equation for an inclined fault (Figure 7A). The model derived thermal energy from three sources: (1) radioactive nuclides, (2) the asthenosphere, and (3) frictional heating along the MCT, and suggested that shear stresses >100 MPa can account for peak T< 600°C at the MCT and contributes ~13°C/km to the inverted geotherm. Huerta et al. (1998) introduced the idea that MCT inverted metamorphism was caused by accretion and erosion acting on a crust enriched with radiogenic elements (Figure 7B). The presence of post-Miocene mineral crystallization ages in the LHF and MCT shear zone led Harrison et al. (1998) to model footwall inverted metamorphism as the accretion of tectonic slivers of the LHF to the hanging wall (Figure 7, Figure 8A). This model was one of the first to suggest the concept of critical taper as an important control in developing inverted

metamorphism and the geometry of the fold-and-thrust belt. In this scenario, anatexis is linked to shear heating on along the MHT. This model is also the first in a series that suggested the Himalaya is an outcome of stacked thrust systems within and below the GHC (Figure 8) (e.g., Kohn, 2008; Corrie & Kohn, 2011; Cottle et al., 2015; Catlos et al., 2020).

Large-scale imaging of the Himalayan and Tibet crust led Nelson et al. (1996) to advocate that thrusting within the Himalaya results from anatexis (Figure 7D). The Tibetan middle crust is assumed to be partially molten today, and the region between the MCT and STDS is earlier extruded equivalent. This model is the foundation of others that suggest the GHC is the result of gravity-driven lateral mid-crustal flow (Gruijic et al., 1996; Beaumont et al., 2001; Jamieson et al., 2006; Searle, 2010; Webb et al., 2011; Cottle et al., 2015). Channel flow was initially conceived as a Neohimalayan event, with the extrusion of the GHC due to synchronous MCT and STDS activity with focused erosion along the topographic front (e.g., Beaumont et al., 2001; 2004; Jamieson et al., 2004; 2006; Robinson et al., 2006; Searle et al., 2006; Long & McQuarrie, 2010; Wang et al., 2013; Cottle et al., 2015). This model can be combined with the scenario where LHF footwall slivers are accreted to the hanging wall as GHC channel flow progressed (Figure 8B). LHF footwall inverted metamorphism may also be an outcome of channel flow experienced by the GHC (Daniel et al. 2003; Searle et al., 2008).

Channel flow has also been invoked to model the inverted metamorphic sequence within the MCT footwall, where discrete fault systems within the LHF and the MCT or other faults within the GHC are active during the Miocene (Imayama et al., 2010; Goswami-Banerjee et al., 2014). The alternative to channel flow is the critical taper model, where the GHC is exhumed through a series of stacked thrust systems within and below the GHC (Figure 8A) (Kohn, 2008; Corrie & Kohn, 2011). Critical taper has also been applied to explain thrusting with fault systems associated with the MFT (Mukul et al., 2007; Hirschmiller et al., 2013). In addition, the recognition that in NW India, the LHF and Tethyan Formation appear in thrust contact suggests that the GHC may have acted as a tectonic wedge (Figure 8C and D) (Webb et al., 2007; Webb et al., 2011; Cottle et al., 2015). One outcome of these models has been a wholesale re-distribution and re-defining of the MCT from a fault system that separates the GHC and LHF to one in which portions of the GHC are involved in large-scale thrust movement (Searle et al., 2008; Carosi et al., 2018). The inverted metamorphic sequence is redelegated from the LHF and MCT footwall to lower levels of the GHC (Figures 8E and F). Thermal heating along faults within the GHC may have played a role in accommodating wedge extrusion and developing inverted metamorphism (e.g., Goscombe et al., 2006; Searle et al., 2008). Figure 8G shows a scenario in which the MCT shear zone develops due to imbrication and activity is accommodated by fault systems within the GHC (Carosi et al., 2016). GHC structures include the Kalopani shear zone (KSZ) at 41-30 Ma (Eohimalayan time frame) and High Himalayan Discontinuity (HHD) at 26-24 Ma (Neohimalayan).

Although lines of evidence exist that the LHF inverted metamorphism involved multiple episodes of post-Miocene imbrication and deformation with the MCT shear zone or LHF duplex (e.g., Figure 5) (Caddick et al., 2007; Catlos et al., 2001; Kohn et al., 2001; Groppo et al., 2009; 2010; Herman et al., 2010; Mosca et al., 2012; Montomoli et al., 2013; Mottram et al., 2014; Carosi et al., 2016; Braden et al., 2018; Catlos et al., 2018; Montemagni et al., 2018; Catlos et al., 2020; Montemagni et al., 2020), the idea of tectonic inversion of a coherent rock package that experienced a single Barrovian Neohimalayan-related metamorphic event remains (Hubbard, 1996; Martin et al., 2010; Gaidies et al., 2015). Multiple episodes of ductile overthrusting of the

GHC over the LHF are proposed as an explanation (Goscombe & Hand, 2000), as well as post and tectonic overpressure that changed fundamental rock properties (Thakur et al., 2015; model of Schmalholz & Podladchikov, 2013). The originally-proposed "hot iron" model in which the primary heat source for inverted metamorphism is GHC thermal energy transferred as Miocene MCT emplacement occurred (England & Molnar, 1993) has an alternative end-member, where no contribution of dissipative to downward conductive heating from the GHC is required (Stephenson et al., 2000).

The Himalaya is often framed as a large-hot orogen that may have grown by distributed extrusion (channel flow) or discrete thrusting (critical taper) (Beaumont et al., 2006; Jamieson & Beaumont, 2013; Mukherjee, 2013; Iaccarino et al., 2020; review in Wang et al., 2013). In fact, both scenarios may be relevant to the Himalayan core, depending on the location within the range and the time frame of metamorphism (Larson et al., 2010; Mukherjee, 2013; Cottle et al., 2015). The Himalaya may indeed represent a scenario in which the two 'end-member models apply and are not mutually exclusive (Beaumont & Jamieson, 2010; Larson et al., 2010, 2013; Corrie et al., 2012; Jamieson & Beaumont 2013; Cottle et al., 2015). Evaluating models for GHC extrusion requires understanding of the P-T-t paths of its rocks as they experienced the transition from convergence and subduction to their final exhumation (e.g., Catlos et al., 2001; Caddick et al., 2007; Kohn, 2008; Corrie et al., 2010; Goswami-Banerjee et al., 2014; Catlos et al., 2018, 2020).

Kohn (2008) presents particle paths predicted by end-member critical taper and channel flow models in the end-member models. Channel flow predicts the GHC experienced isothermal exhumation, and the LHF experiences isobaric heating. Critical taper predictions imply isobaric cooling for GHC rocks and "hair-pin" LHF P-T paths (Kohn, 2008). The metamorphic field gradients predicted by the models also differ. Complicating this scenario is the observation that P-T conditions from garnet-bearing assemblages collected from the MCT hanging wall indicate the unit has cryptic discontinuities related to unmapped faults, shear zones, or inheritance of pre-existing basement structures (see discussions in Mukherjee et al., 2012; Larson et al., 2013; Montomoli et al., 2015; Cottle et al., 2015; Carosi et al., 2016). Understanding when these possible fault systems, termed High Himalayan discontinuities (HHD), were active is critical for deciphering the processes involved during convergence. Their age may similar to activity along the MCT (28-18 Ma; e.g., Carosi et al., 2010; Montomoli et al., 2013, Larson et al., 2015; Montomoli et al., 2015; Carosi et al., 2016; Carosi et al., 2018; Benetti et al., 2021). This is a scenario that is not accounted for in the channel flow model (e.g., Benetti et al., 2021; Maiti & Mandal, 2021).

4 Himalayan Metamorphism and Contractional Tectonics (Darondi Khola, Central Nepal)

As indicated in the previous sections, garnet-bearing assemblages are valuable recorders of compressional/contractional metamorphism and help constrain models for the Himalaya's uplift history. P-T data from garnet-bearing Himalayan assemblages can be generated using several approaches (see review in Waters, 2019). This section compares conditions generated using conventional thermobarometers and the Gibb's method (Kohn et al., 2001) to those obtained using isochemical phase diagrams, isopleth thermobarometry, and the garnet zoning method (e.g., de Capitani & Petrakakis, 2010; Moynihan & Pattison, 2013; Catlos et al., 2018; 2020). The approaches were applied to the same samples and data from rocks collected from the GHC and LHF units along the Darondi Khola in central Nepal (Figure 3, Figure 4, Figure 5). The TheriaG model of Gaides et al. (2008) is also used to predict garnet zoning based on Gibb's P-T

paths for some samples. The reason for any discrepancies in the P-T paths and conditions within the context of equilibrium thermodynamics is evaluated, and the impact of the results on models for Himalayan orogenesis is explored. Regardless of calibrations used, the P-T conditions and paths coupled with previously-reported timing constraints from Darondi Khola assemblages suggest the MCT shear zone developed during pulses of movement that resulted in progressive transfer of rock packages as the MCT shear zone developed (Catlos et al., 2001; Kohn et al., 2001).

4.1 Methods, samples, and assumptions

4.1.1 Samples

Kohn et al. (2001) report rim P-T conditions from eighteen garnet-bearing assemblages exposed along the Darondi Khola and divides LHF samples into lowermost (n=3), lower to mid (n=6), and upper MCT zones (n=4) (Figure 4 and Figure 5, Table 1). Five GHC rocks were also analyzed. We use the definition of the MCT shear zone following this nomenclature, but also note that based on the placement of the Phaplu and Ulleri augen gneisses, others would allocate all of these samples squarely in the GHC unit (e.g., Searle et al., 2008).

Mineral assemblages, X-ray element maps, and compositional transects were made across garnets and are reported in Kohn et al. (2001). Petrographic images of some samples are shown in Figure 9. All samples contain garnet and prograde quartz, muscovite, biotite, and ilmenite. All are metamorphosed pelites, except DH38, which is a metabasite and contains hornblende and plagioclase. All lower LHF rocks contain prograde chlorite and plagioclase, but DH75A and DH75B also have retrograde chlorite (Figure 9). The upper LHF and GHC rocks do not have chlorite (DH38, DH60, DH61, DH63, DH66, DH67) or contain only retrograde chlorite (DH57, DH58, DH71). All samples, except upper LHF rock DH57, contain plagioclase. Most plagioclase show core-rim zoning with higher-Ca cores and lower-Ca rims, expected if garnet grew in a closed chemical system (Spear et al., 1990). Samples DH26, DH75A, and DH75B have plagioclase with relict albite cores overgrown by an oligoclase mantle that is either unzoned or slightly zoned to lower Ca towards its rim. The mantle was assumed to be metamorphic and reflects garnet growth and uptake of Ca. Sample DH57 has both staurolite and kyanite, whereas DH63 has staurolite. Other rocks for this study do not show any of these index minerals. No chloritoid or carbonate minerals are reported in the samples. All samples appear syntectonic and the presence of strain shadows are common. As seen in Figure 9, micas and quartz appear deflected around the garnet porphyroblasts. Some garnets are inclusion free, however, middle LHF sample DH30 has quartz inclusions in the center of the garnet that appear thinner and elongated compared to the larger, anhedral grains in its outer-rim region. GHC samples DH61, DH63, and DH67 have inclusion filled cores and inclusion free outer rims. Inclusions of ilmenite and quartz in middle LHF samples DH51 and DH75B are aligned in relatively straight tracks into the rock matrix, consistent with syntectonic growth.

Figure 10 shows garnet compositional transects for LHF samples in which high-resolution P-T paths (DH17, DH19, DH22, DH23, DH26, DH75B) were obtained and Figure 11 shows compositional transects across garnets in two GHC samples (DH61 and DH66). LHF samples show typical prograde bell-shaped profiles in Mn, with no evidence of retrogression at the rims. The garnets all show a smooth decrease in grossular and increase in pyrope and almandine from core to rim. GHC garnets, however, show evidence of retrogression with sharp increases in Mn contents at the rim. These garnets also show significant fluctuations in grossular,

pyrope, and almandine from core to rim. GHC samples are not ideal candidates for high-resolution P-T path modeling because their zoning profiles suggests modification of prograde garnet compositions after growth, open-system behavior, and the potential of major changes in rock bulk composition after growth. These situations are assumed not to occur when modeling and developing high-resolution P-T paths.

4.1.2 Conventional thermobarometry and Gibbs method P-T paths

The garnet-biotite thermometer calibrated by Ferry and Spear (1978) with the Berman (1990) Ca-in garnet solution model and the garnet-muscovite-biotite-plagioclase barometer of Hoisch (1990) were applied to the assemblages with pelitic bulk compositions (Kohn et al., 2001). Sample DH38 is a metabasite, so the garnet-hornblende thermometer of Graham and Powell (1984) and the garnet amphibolite barometer of Kohn & Spear (1990) were used. Results are summarized in Table 1. The conditions are internally consistent, and Kohn et al. (2001) emphasize that different calibrations would change estimated P and T by ±25°C and ±0.5–1 kbar and would not alter overall trends. The conditions were estimated using minimum garnet Mn contents. Note that these garnet compositions are the same used for the estimating the garnet rim conditions using isopleth thermobarometry as described in the next section (Table 2; polygons in Figure 12, Figure 13, Figure 14, Figure 15, Figure 16, Figure 17).

The Gibb's method to generate the P-T paths from zoned garnets and their co-existing matrix mineral assemblages is outlined in Spear & Selverstone (1983), Spear (1986, 1993), Spear et al. (1984), and Spear & Rumple (1986). P-T paths were only generated from LHF rocks with pelitic bulk compositions (DH16, DH17, DH22, DH23, DH26, DH75A, and DH75B) that preserved prograde compositional zoning best. The rocks were modeled with the observed solid assemblage garnet + biotite + chlorite + muscovite + plagioclase + quartz in the MnNCKFMASH system. Compositional changes were derived from garnet and plagioclase compositional zoning produced as the garnet grew. Garnet core and rim conditions were selected for samples DH17, DH19, DH22, and DH26, whereas an intermediate point was also included for samples DH23, DH75A, and DH75B. This intermediate garnet composition was used to better account for nonlinearity in the garnet zoning pattern. In the case of DH23 and DH75B, its inclusion results in hair-pin P-T paths (Figure 13A, Figure 14C, and Figure 17). A pure H2O fluid at lithostatic pressure was assumed to have been present. Kohn et al. (2001) emphasize that activity models would not significantly affect the trends of retrieved P-T paths.

The P-T results obtained using conventional and Gibb's method show an inverted metamorphic signature in the LHF, with P-T conditions increasing up section from near the garnet isograd at 520±25°C and 5.0±1.0 kbar (DH16) to 640±25°C and 11.5±2 kbar (samples DH57 and DH58) just below the mapped MCT. GHC rocks were collected near the mapped MCT (Figure 4 and Figure 5) and record the highest P-T conditions (660-715°C and 7.6-11.5 kbar). Samples DH17, DH19, and DH75A have P-T paths consistent with burial (increasing in both P and T), whereas those from DH22 and DH26 yield exhumation paths (decreasing P with increasing T). P-T paths from DH75B and DH23 are "hair-pin" and are interpreted as recording both burial and exhumation during imbrication of the MCT shear zone. Monazite inclusions in DH75B garnets range from 11.1±0.7 Ma to 7.6±0.2 Ma (Th-Pb secondary ion mass spectrometry, SIMS, ±1□) and were interpreted as constraining Late Miocene reactivation of the MCT shear zone (Figure 5). These Late Miocene monazite inclusions in garnet are also found in other samples along the transect as well as young (Pliocene-Late Miocene) $^{40}Ar/^{39}Ar$ muscovite total gas ages (Catlos et al., 2001; Kohn et al., 2001).

4.1.3 Isopleth core thermobarometry

The approach to obtain isopleth P-T conditions and paths is the same as that outlined in Catlos et al. (2018, 2020) and Etzel et al. (2019). Bulk rock compositions were obtained from rock chips of the DH samples using inductively coupled plasma spectrometry (ICP) at Activation Laboratories (Canada) (Table 3 and Table 4). No modifications in these compositions were made for the approach. Samples DH22 and DH23 were collected nearby, and the same bulk composition is used for both rocks. Compositions vary from low SiO_2 (~45 wt % samples DH17, DH22, and DH23) to higher SiO_2 (69-76 wt% DH26, DH75A). In general, upper LHF and GHC rocks have mid to high SiO_2 contents (56-80 wt%). Their molar values are used as direct input for the effective bulk composition needed to create the isochemical phase diagrams using the software package Theriak-Domino (de Capitani and Brown, 1987; de Capitani and Petrakakis, 2010) (Figure 12, Figure 13, Figure 14, Figure 15, Figure 16, Figure 17). The Holland and Powell (1998 with updates to solution models through 2010) thermodynamic dataset and appropriate mixing models in the system MnO-Na_2O-CaO-K_2O-FeO-MgO-Al_2O_3-SiO_2-H_2O-TiO_2 were used. The specific solid solution models used are the same as in Catlos et al. (2018). H2O saturation is assumed for these samples (i.e., H2O (100) in Theriak Domino), as is appropriate for these assemblages. Fe^{3+} was not estimated but did not significantly affect results.

For samples where compositional data were available from the garnet's central section, isopleths of ±0.01-0.02 mole fraction spessartine, almandine, pyrope, grossular, and ±0.01-0.02 Mg-# (Mg/Fe+Mg), are plotted on the phase diagram as grey-shaded bars. Their intersection corresponds with our closest approximation of garnet core P-T conditions as indicated by a polygon. Although isopleth intersections occurred over small regions, the uncertainty in the conditions is likely approaching that of conventional methods (i.e., ±25°C and ±1 kbar). Overlapping garnet core isopleths are only found for LHF samples DH17, DH19, DH22, DH23, DH26, DH75A, DH75B, DH58, and GHC sample DH61 (Figures12, Figure 13, Figure 14, Figure 15, Figure 16). The core was defined as the portion of the garnet with the highest Mn content and is the best approximation of the chemical system when garnet began growth. In all cases, the intersections are located in mineral stability fields consistent with their assemblages (feldspar + garnet + biotite + phengite + ilmenite ± rutile ± chlorite + quartz + H2O) and anticipated conditions. Core metamorphic conditions increase up section over a north-south distance of ~5 km from a low of 4-4.5 kbar and 520-540°C in lower LHF samples DH17 and DH19 to 6.8-7.5 kbar and 540-550°C in middle LHF samples DH75A and DH75B (Table 2). Upper LHF sample DH58 collected directly beneath the MCT yields overlapping core isopleths at ~550°C and 6.0 kbar. Core isopleths for GHC sample DH61 overlap at ~7 kbar and 580°C, similar to those from some LHF rocks (Table 2).

The garnet-in reaction line and garnet growth contours (volume 0.5% increments) are overlaid on each isochemical phase diagram (Figure 12, Figure 13, Figure 14, Figure 15, Figure 16). The topology of the diagrams and the location of the garnet core suggest that garnet appears in all samples through chlorite dehydration. Only samples DH75A and DH75B yield core P-T conditions that overlap the garnet-in reaction line (Figure 14). The other samples yield overlapping isopleths on or near the 0.5% (DH17, Figure 12A), 1% (DH19, DH61, DH58, Figure 12C, Figure 15A and Figure 15C), and 1.5-2% volume contours (DH22 and DH23, Figures 12E and Figure 13A). The results suggest that the true core was missed during the analysis of these garnets. The lack of retrograde zoning in the LHF samples suggests that the effect of diffusional

homogenization is minimal (Figure 10), although this process likely modified GHC DH61 garnet compositions (Figure 11B).

4.1.4 High-resolution and Gibb's P-T path modeling

For samples DH17, DH19, DH22, DH23, DH26, DH75A, and DH75B, the garnet's core isopleth P-T conditions can be directly compared to those obtained using the Gibb's approach (Figure 17). Sample DH26 yields the same pressure using both methods (~6.5 kbar), but the thermal conditions are lower using the Gibb's method by 50°C. Sample DH23 yields the same thermal conditions using both approaches (~525°C), but the isopleth barometry suggests the sample experienced lower pressures by ~2 kbar (5.1 kbar compared to 7.0 kbar). In all other samples, isopleth thermobarometry results in the samples recording lower P (from 0.5 kbar to 1.7 kbar, samples DH75A and DH75B) and higher T (from 10°C to 50°C, samples DH75A and DH75B) compared to than those generated by the Gibb's method. The discrepancies of 10°C and 0.5 kbar are within the stated uncertainties of both methods (Kohn, 1993), but those approaching 50°C and 1.5 kbar are significant differences that would influence understanding their depth of exhumation and metamorphic reaction history. For example, in sample DH26, the Gibb's core P-T condition shows similar P, but the low Gibb's T starting conditions lie in a region where chlorite, not garnet, is stable (Figure 13C).

High-resolution P-T paths (Moynihan and Pattison, 2013) were generated for lower LHF samples where garnet transect data were available, suggested prograde conditions, and minimal modification since growth. In generating the high-resolution P-T paths, zoning profiles are smoothed using a Savitzky-Golay function to minimize the impact of missing analyses due to inclusions or cracks (Figure 10). The Matlab script starts with the bulk composition and initial smoothed core garnet composition and calls Theriak-Domino to calculate an isochemical phase diagram. A Matlab optimization function searches the P-T grid for the smallest misfit between a modeled garnet composition and the smoothed composition. It then calculates the portion of the bulk composition sequestered in the first step of garnet growth. Sequestered components are subtracted from the bulk composition to estimate an effective bulk composition for the next step of growth. A new diagram is calculated from the effective bulk composition, and the process is repeated for all steps along the garnet zoning profile from core to rim. Each step yields an estimate of the P-T conditions of incremental garnet growth, culminating in a P-T path. This data is available in the repository.

Two independently estimated high-resolution P-T paths can be obtained from a rim-to-rim compositional transect across the garnet using the garnet zoning method. The expectation is that the P-T paths from the same garnet should record similar trajectories, and was the case for samples DH17, DH19, and DH23 (Figures 12A and C, Figure 13A). The starting and endpoints may differ due to the proximity of the initial condition near the garnet core and the extent of garnet rim preservation. In addition, garnet zoning can be predicted by the high-resolution P-T path and is indicated as a bolder grey line in Figure 10. The high-resolution P-T paths reproduce the original garnet zoning to ±0.01 mole fraction in most cases and for most compositions, which is expected if the garnet behaved in a closed system and had no significant changes in bulk rock composition as it grew.

As with the core conditions, the shapes of the high-resolution P-T paths for samples DH17, DH19, DH22, DH23, DH75A, and DH75B can be directly compared to those obtained using the Gibb's approach (Figure 17). The length of the high-resolution and Gibb's P-T paths are

similar (ranges from 14°C to 52°C) but do not show the same trajectories. For example, instead of hair-pin trajectories (increase in P followed a P decrease as T increases) predicted by DH23 and DH75B Gibb's P-T paths, their high resolution P-T paths suggest that these rocks only experience an increase in P as T increased. The Gibb's P-T path in sample DH17 shows an increase in P, but the high-resolution P-T path from the same rock using the same data decreases in P as T increases. Minor fluctuations in P in the high-resolution P-T paths (±10-50 bars) in sample DH19 and near the core of sample DH22 are likely due to small compositional changes as the program seeks the best fit and should not be interpreted tectonically. DH19 shows an overall similar P-T path shape as the one reported using the Gibb's approach, but the conditions are different with the high-resolution P-T path showing much lower P (by ~2 kbar) and higher T (by ~50°C). The high-resolution P-T paths from samples DH22 and DH23 are similar in that they show minor increases in P as T increased, but the Gibb's P-T path from sample DH22 suggests decompression, a result not observed with this sample. A P-T path from sample DH26 could not be generated due to a lack of garnet zoning data, but core and rim isopleth conditions suggest it could have followed the decompression path as T increased. A decrease in P as T increased is the same trajectory suggested by the Gibb's P-T path but at higher T conditions.

To gauge how well Gibb's P-T paths reproduce garnet zoning, the Gibb's P-T path was used as input in the program TheriaG (Gaides et al., 2008) using the bulk composition indicated in Table 3. The time of garnet growth over the P-T path is regularly spaced over durations of 5 m.y., 10 m.y., and 15 m.y. Modeling parameters are available in supplementary files. In each case, the predicted Gibb's P-T path was identical and would predict garnet zoning inconsistent with what is observed in the sample (Figure 10). Results may change if different size classes than those used were selected (10 μm successive shells in 2000 □m garnet radius), if garnet growth did not occur over regular space durations, or if the selected exhumation path was different. Using the chosen parameters, the Gibb's P-T path predictions for samples DH17, DH19, and DH22 show similar trends with the garnet zoning but significantly different compositions (Figure 10). The Gibb's P-T paths predictions for those samples that produced hair-pin P-T paths (DH75B and DH23) resulted in significantly different garnet zoning and compositions and did not replicate observed garnet compositions.

4.1.5 Isopleth rim thermobarometry

Garnet rim isopleth conditions were estimated using the same garnet compositions used to generate conventional P-T conditions. Rim isopleths also include those from the sample's average composition of matrix plagioclase (±0.01 mole fraction Ca), chlorite, and biotite [±0.01 Mg-number, Mg#= Mg/(Mg+Fe)], when available. The last effective bulk composition generated by the high-resolution P-T paths was used for LHF samples DH17, DH19, DH22, DH23, and DH75B. For other LHF samples where garnet transect data is not available and for the GHC rocks, the bulk composition was used (DH26, DH75A, DH58, DH60, DH61, DH63, DH66, DH67) (Table 3 and Table 4). Only three GHC samples (DH61, DH63, and DH66) yield overlapping garnet compositional isopleths (Figure 15D, Figure 16A and B), and those from upper LHF sample DH58 did not overlap.

The extent of overlap of garnet rim with matrix mineral compositions varies for the GHC and LHF rocks. Garnet rim isopleths for GHC sample DH61 rim overlapped with all matrix mineral compositions, but DH66 show no overlap of the garnet rim with any of the matrix mineral compositions. The garnet rim isopleths for GHC sample DH63 overlapped with ±0.01 Mg-number chlorite, but not with the biotite or plagioclase compositions. As seen with some

844 footwall samples, the overlaps for the GHC assemblages are located far from the garnet-in
845 reaction line as seen by the garnet growth contours (>1.5 vol%) (Figure 15 and Figure 16). The
846 garnet rim isopleths for LHF samples DH17, DH19, DH22, DH23, and DH75B overlap with
847 Mg# biotite, but not plagioclase. No matrix mineral isopleths overlap with the garnet rim
848 isopleths for samples DH26 and DH75A within the compositional ranges applied here (±0.01
849 mole fraction Ca and Mg#).

850 For samples where garnet and matrix mineral isopleths overlap, conditions are consistent
851 with their mineral assemblages and are similar to the garnet core assemblages (feldspar + garnet
852 + biotite + phengite + ilmenite ± rutile ± chlorite + quartz + H2O). As with the core conditions,
853 the rim P-T conditions increase up section over a north-south distance of ~5 km from a low of
854 4.5-4.8 kbar and 550-560°C in lower LHF samples DH17 and DH19 to 5.5-8.8 kbar and 560-
855 590°C in middle LHF samples (Table 2). Although garnet compositional data is not available for
856 Upper LHF sample DH51, its mineral assemblage of coexisting staurolite and kyanite allows for
857 an approximation of rock conditions using only its bulk rock composition and observations
858 conditions where these mineral coexist (Figure 15E), which appears at ~7.0 kbar and ~650°C.
859 Rim isopleths for GHC samples DH60, DH61, and DH66 yield similar P of ~7 kbar, but T
860 ranges from 550-600°C. GHC sample DH63 yields the highest P-T isopleth conditions of ~10.5
861 kbar and 650°C.

862 Comparisons are made between the conventional rim P-T conditions and isopleth rim
863 conditions. As seen in Figure 17B, the lower LHF samples yield higher T (by 25-30°C) and
864 lower P (by 1.4-2.3 kbar). All middle LHF samples (Figure 17D and F) overlap in P conditions
865 within uncertainty, but the isopleth T for samples DH22 and DH26 is higher than the
866 conventional results by 5-85°C, depending on how uncertainty is applied. For GHC sample
867 DH61, the approaches yield similar T conditions, but P differ by 1-2 kbar, depending on
868 uncertainty (Figure 17F). The opposite observation is seen with GHC sample DH66, where P is
869 similar, but the isopleth conditions suggest significantly lower T (Figure 17F). Some overlap is
870 seen with GHC sample DH63, but the conventional results suggest higher P-T than the isopleth
871 results.

872 **5 Discussion**

873 Using the same samples and data, Darondi Khola MCT footwall P-T paths using the
874 Gibb's method and high-resolution garnet modeling do not yield the same conditions or shapes
875 (Figure 17), even within the estimated uncertainties of the Gibb's method (e.g., Kohn, 1993). In
876 addition, the lowest-grade footwall samples record higher T and lower P isopleth rim P-T
877 conditions than those generated using conventional thermometers and barometers. Conventional
878 garnet rim P-T conditions and isopleth thermobarometry for GHC samples yield absolute
879 conditions that differ, although overlap exists within uncertainty (±25°C and ±1kbar). An
880 important check on the feasibility of the P-T conditions generated using any approach is if the
881 results seem geologically reasonable and consistent with mineral assemblages (e.g., Moynihan
882 and Pattison, 2013; Kelly et al., 2015; Catlos et al., 2018; Etzel et al., 2019; Craddock Affinati et
883 al., 2020). However, this is the case with all conditions reported for the Darondi Khola samples,
884 regardless of approach.

885 Several assumptions underlie many P-T estimates generated using thermodynamic
886 modeling. For all thermobarometric methods applied here, a critical assumption is that the
887 minerals in a sample experienced equilibrium, which can never be proven for any rock system

(e.g., Spear & Peacock, 1989; Lanari & Duesterhoeft, 2019). The samples are also assumed to have experienced closed system behavior, and the original compositions of the mineral phases and the bulk rock have not changed significantly since metamorphism (e.g., Lanari and Engi, 2017). LHF assemblages appear to have preserved their original garnet compositions, as shown by their prograde zoning profiles (Figure 10). Garnets with preserved divalent cation zoning based on previously reported thermal conditions of generally <600°C (e.g., Carlson, 1989, Spear, 1993; Carlson 2002), consistent with the results shown here. GHC samples show fluctuations in garnet compositions from core to rim and have evidence of diffusional modification by an increase of Mn at the rims (Figure 11).

Multiple sources of error are inherent in conventional P-T conditions and include uncertainty in the accuracy of end-member reactions, electron microprobe analyses, calibration errors, variations in activity models, and compositional heterogeneity (e.g., Kohn & Spear, 1991). The precise uncertainty with approaches that involve isochemical phase diagrams is likewise challenging to determine due to the same factors incorporated into their creation as well as uncertainty associated with the thermodynamic properties inherent in the choice of internally consistent database (e.g., molar enthalpy of formation, molar entropy, molar volume, heat capacity, bulk modulus, Landau parameters, and Margules parameters, e.g., White et al., 2014; Lanari & Duesterhoeft, 2019). The error suggested by the grid created due to overlapping mineral compositional isopleths likely underestimates the actual uncertainty in the identified conditions. Applying a standard values of uncertainty (±25°C and ±1 kbar) to the overlapping isopleth conditions as those used for conventional results appears appropriate, and is commonly reported (e.g., Spear & Peacock, 1989; Kohn, 1993; Kohn et al., 2001).

Ultimately, each approach to generating P-T conditions discussed here transforms the sample into a model representing the true rock and mineral assemblage but restricts its behavior as if it was in a closed system that experienced particular boundary conditions. Confidence in conventional and Gibb's P-T paths increases when conditions agree with minerals assemblages and if the P-T paths reproduce broad-scale trends in garnet zoning from core to rim. Samples collected from the same outcrop or nearby should yield similar P-T conditions and paths. Although Kohn et al. (2001) only report one Gibb's P-T path per sample, the expectation is that multiple paths collected from the same garnet or multiple garnets in the same rock would agree in terms of shapes and conditions. The high-resolution P-T path approach and the garnet isopleth thermobarometry use these same criteria to evaluate the estimated result's appropriateness. However, they have two additional values in critically evaluating results. First, a user can gauge the extent of overlapping mineral isopleths in P-T space. Second, a user can identify how well the high-resolution P-T paths predict the trends and values of garnet compositional zoning (Figure 10). A significant value of the high-resolution P-T path and isopleth approaches is that a user can detect when systems stray from the equilibrium and closed system assumptions.

These samples illustrate that not all garnets are suitable candidates for high-resolution P-T path modeling and isopleth thermobarometry. Garnets with significant changes in composition over short distances from core to the rim and those affected by diffusion cannot be modeled. Garnets in samples that experienced significant changes in bulk composition or multiple deformation episodes resulting in modification of composition are also unable to be modeled. Not all field areas are ideal candidates, and the GHC samples show that they often fail assumptions required for isopleth thermobarometry and high-resolution P-T path modeling. For example, overlapping garnet core isopleths were only found for one GHC sample DH61, and this

was located far from the garnet-in reaction line (Figure 15C). In fact, the intersections for all samples, except DH75A and DH75B, are far from the garnet-in reaction line (>1 vol%), although all overlap mineral stability fields consistent with rock assemblages. The compositional core may not coincide with the geometric garnet center (e.g., Spear & Daniel, 1998), shown for most samples. Overlapping garnet compositional rim isopleths were found for three GHC samples (DH61, DH63, DH66), but only GHC sample DH61 appears ideal as garnet rim isopleths also intersect those of the matrix minerals (±0.01 mole fraction Ca in anorthite and ±0.01 Mg# chlorite and biotite). Confidence in isopleth conditions increases when matrix mineral compositions overlap the garnet rim conditions, as these mineral compositions are independent.

The high-resolution P-T paths should be considered approximations of how a garnet with a specific type of compositional zoning would behave in a closed system of a known bulk composition as it evolves during increasing T. Rocks are open systems, but LHF garnet-bearing assemblages appear as if they approach an ideal scenario of a closed system. This appearance of equilibrium is shown by overlapping isopleths of compositions from the garnet core and from those of the garnet rim with matrix minerals. In addition, predictions of garnet zoning made by the high-resolution P-T paths closely match the original garnet for these samples (Figure 10). Multiple paths from the same sample yield similar conditions and shapes. The inability to reproduce garnet zoning using Gibb's P-T path trajectories using TheriaG modeling suggests these paths may not be relevant to the samples using the applied parameters.

Regardless of calibrations used, the P-T conditions and paths along with previously-reported timing constraints, are consistent with an imbrication model that suggest the MCT shear zone developed as rock packages within the LHF were progressively transferred (Catlos et al., 2001; Kohn et al., 2001). For example, Figure 18 shows P-T path predictions for one such imbrication model described in Catlos et al. (2018) and (2020). In this model, thermobarometric histories are calculated using a two-dimensional finite-difference solution to the diffusion-advection equation. Samples within the LHF travel along the MCT at a 5 km/Ma speed rate from 25 to 18 Ma (Figure 18A). The hanging wall speed rate is 10 km/Ma, and topography progressively accumulates until a maximum height of 3.5 km. The increase in topography is required to accommodate the pressure changes recorded by the garnets while matching their thermal histories. Once the topography is achieved at 18 Ma, a period of cessation is applied to the MCT between 18 and 15 Ma, and topography is reduced at a rate of 1.5 km/Ma. The model returns to activity within the MCT shear zone with the activation of the MCT footwall slivers from 8 to 2 Ma (Figure 18B). P-T changes recorded by the footwall garnets are the direct result of thermal advection combined with alterations in topography. Changes in the timing of fault motion would affect the model outcomes. However, the model’s current constraints and boundary conditions appear to match the observed high-resolution P-T paths. For example, the P-T diagram in Figure 18 C-E are model predictions for samples that experienced imbrication in the MCT footwall. High-resolution P-T paths are also plotted in these panels from samples collected from the LHF along the Darondi (Figure 18C) and Marsyangdi (Figure 18D) rivers in central Nepal and from along the Bhagirathi River in NW India (Figure 18E). For most samples, the P-T paths match the model predictions remarkably well. P-T paths for sample DH75B (Panel 18C) suggests the possibility of very high exhumation rates (>12mm/year) within the MCT shear zone since the Pliocene, which is a scenario predicted by this imbrication model.

6 Conclusions

This paper reviews the geological framework of the Himalayas and describes and applies particular thermobarometric approaches to decipher the metamorphic history of garnet-bearing rocks collected across the MCT along the Darondi Khola in central Nepal using previously reported data (Kohn et al., 2001). A comparison is made between the results of conventional and isopleth thermobarometry for all samples and high-resolution and Gibb's P-T paths for MCT footwall rocks only. A significant value of the high-resolution P-T path and isopleth approaches is that a user can detect when systems stray from the equilibrium assumption. Confidence in conditions exists when minerals assemblages predicted by thermodynamic modeling appear consistent with the actual rock and when the P-T paths reproduce broad-scale trends in garnet zoning from core to rim. The expectation is that multiple paths collected from the same garnet or multiple garnets in the same rock would agree in terms of shapes and conditions and that samples collected from the same outcrop or nearby should record similar P-T conditions and paths. Using isopleth thermobarometry, a user can gauge the extent of overlapping mineral compositions and where the overlap occurs with respect to the garnet-in reaction line and garnet volume % growth contours. MCT footwall garnet compositions predicted by Gibb's P-T paths using the software package TheriaG fail to reproduce the original garnet zoning. However, high-resolution P-T paths reproduce the original garnet zoning to ±0.01 mole fraction in most cases and for most compositions, expected if the garnet behaved in a closed system and had no significant changes in bulk rock composition as it grew. Although the assumption of equilibrium has long been known can never be proven for any rock system (e.g., Spear & Peacock, 1989), isopleth thermobarometry and high-resolution P-T path modeling applied to garnet-grade Himalayan MCT footwall assemblages show they appear to behave as if they evolved in a closed system that experienced particular P-T path trajectories. Ultimately, the P-T conditions and paths generated for rocks across the MCT along the Darondi Khola, regardless of calibrations used, are consistent with the imbrication model that suggest the MCT shear zone developed as rock packages within the LHF were progressively transferred (Catlos et al., 2001; Kohn et al., 2001).

Figure Captions

Figure 1. Geological map of the Himalayas after Yin (2006). See Figure 2 for a cross-section through central Nepal and Figure 3, Figure 4, and Figure 5 for the sample transect taken across the MCT shear zone along the Darondi Khola.

Figure 2. Generalized cross-section through the Himalayas in central Nepal after DeCelles (2015) and Robinson et al. (2006). See additional cross-sections in the range in DeCelles et al. (2020).

Figure 3. Generalized geological map of the Annapurna-Manaslu-Ganesh region of central Nepal after Colchen et al. (1980). Isograds are dashed and labeled: bt= biotite, grt= garnet; ky= kyanite; sta= staurolite; sil= sillimanite; pyx= pyroxene, carbonate lithologies. STDS? = the presence of the South Tibetan Detachment is debated; MCT= Main Central Thrust; MCT-I?= the presence of Arita's (1983) thrust at the base of the MCT shear zone is debated.

Figure 4. Sample location map from rocks collected along the Darondi Khola. The contour interval is 500 ft. See Figure 3 for the location of this transect on the geological map of the Himalayas. Samples are indicated by "DH#" in the text. Isograds are dashed and labeled (grt= garnet; stau= staurolite). See Figure 5 for a cross-section along A-A'.

Figure 5. Cross-section across the Darondi Khola section showing available muscovite $^{40}Ar/^{39}Ar$ and Th-Pb ages after Catlos et al. (2001). See Figure 4 for line of section.

Figure 6. Cross-sections of early models of Himalayan inverted metamorphism and leucogranite formation. (A) The "hot-iron" model of LeFort 1975. (B) Juxtaposing right-way-up metamorphic isograds after Hubbard (1996). (C) A combination of models in panels (A) and (B) after Searle and Rex (1989). Wedge extrusion models after (D) Hodges et al. (1993) and (E) Harris & Massey (1994).

Figure 7. Cross-sections of early kinematic models of Himalayan inverted metamorphism and leucogranite formation. (A) After Molnar and England (1990). (B) After Huerta et al. (1998). (C) After Harrison et al. (1989). (D) After Nelson et al. (1996).

Figure 8. (A) An illustration of the critical taper model. (B) Schematic of channel flow and wedge extrusion. (C) A combination of critical taper and tectonic wedging of the GHC. A "*" indicates an incipient fault. (D) Illustration of GHC tectonic wedging after Webb et al. (2011). Panels (E) and (F) show the final geometry of the range, which has affected the position and definition of the MCT. Panels (A), (B), (C), and (E) are after Cottle et al. (2015), and panel (F) is after Searle et al. (2008).

Figure 9. Selected petrographic (plane polarized light) images of samples along the Darondi Khola showing the relationship of the garnet porphyroblasts and rock textures. Garnets are outlined using bold lines. Pressure shadows and inclusion trails are indicates by lighter and dashed lines, respectively. Mineral abbreviations after Whitney and Evans (2010). Panels are labeled with sample number. The scale bar for each image is 200 □m. See Figure 4 and 5 for sample locations.

Figure 10. Compositional transects across garnets in lower LHF samples (A) DH17 and (B) DH19, and middle LHF samples (C) DH22, (D) DH23, and (E) DH75B. Distance is in analytical points, and the spacing between the points is ~20□m. The larger black squares are the raw electron microprobe data, whereas the smaller black squares near the EPMA data points are the smoothed data used for input into the model to generate the high-resolution P-T paths. The high-resolution P-T paths predict garnet zoning, which is shown by the bold gray lines. TheriaG was used to predict the garnet zoning for the Gibb's P-T paths, and these are also indicated.

Figure 11. Compositional transects across garnets in GHC samples DH66 (two transects) in (A) spessartine, (C) grossular, (E) pyrope, and (G) almandine. Panels (B), (D), (F), and (H) are compositional transects in spessartine, grossular, pyrope, and almandine, respectively, across a garnet in sample DH61. Distance from the garnet core is in analytical points, and the spacing between the points is ~20□m.

Figure 12. Isochemical phase diagrams from lower LHF samples DH17 (A) garnet core and (B) garnet rim, DH19 (C) core and D (rim), and mid-LHF sample DH22 (E) core and (F) rim. See Figures 4 and 5 for sample locations. Garnet-in reaction line (+Grt) and garnet growth contours (volume 0.5% increments) are overlaid on each diagram. Each core diagram was created using the rock bulk compositions reported in Table 3 and the software program Theriak-Domino. Some mineral stability fields are labeled using abbreviations after de Capitani and Petrakakis (2010) and include quartz and H2O. For the core diagrams, isopleths of ±0.01-0.02 mole fraction spessartine (XMn), grossular (XCa), pyrope (XMg), almandine (XFe), and ±0.01-0.02 Mg-number (Mg/Fe+Mg, Mg#) of the compositional data point selected from the garnet's highest Mn content are overlain (Kohn et al., 2001). They intersect as indicated by the polygon and labeled as "T-D core." High-resolution P-T paths (DH17, n=2; DH19, n=2; DH22, n=1) were generated from garnet core-to-rim transects after the approach of Moynihan & Pattison (2013).

These are compared to the P-T paths obtained using the Gibb's method for the samples using the same data by Kohn et al. (2001). The starting point of the Gibb's P-T paths is labeled with "Gibb's core." Isochemical phase diagrams for the garnet rim were created using the final effective bulk composition generated by Theriak-Domino. In this case, isopleths for the garnet compositions reported for garnet rims are overlain on the diagram, as well as matrix mineral compositions isopleths for An-content for plagioclase, Mg-number for biotite and chlorite, (Mg/Fe+Mg, Mg#-bt and Mg#-chl) (Kohn et al. 2001), when available. They intersect as indicated by the polygon and labeled as "T-D rim." These are compared to the rim P-T conditions (GB-GBMP conditions) for the samples using the same data and conventional thermobarometric approaches by Kohn et al. (2001).

Figure 13. Isochemical phase diagrams from middle LHF samples DH23 (A) garnet core and (B) rim and DH26 (C) core and (D) rim. See Figures 4 and 5 for sample locations. Detailed caption is the same as in Figure 12. High-resolution P-T paths for sample DH23 were generated from two garnet core-to-rim transects after the approach of Moynihan & Pattison (2013). These are compared to the P-T paths obtained using the Gibb's method for the samples using the same data by Kohn et al. (2001). No data was available for the garnet transect for sample DH26, so a high-resolution P-T path was not created. In this case, the rock bulk composition (Table 3) was used for both core and rim panels.

Figure 14. Isochemical phase diagrams from middle LHF samples DH75A (A) garnet core and (B) rim and DH75B (C) core and (D) rim. See Figures 4 and 5 for sample locations. Detailed caption is the same as in Figure 12. High-resolution P-T paths for sample DH75B were generated from garnet core-to-rim transects after the approach of Moynihan & Pattison (2013). These are compared to the P-T paths obtained using the Gibb's method for the samples using the same data by Kohn et al. (2001). The Gibb's path was also reported for sample DH75A. The starting point of the Gibb's P-T paths is labeled with "Gibb's core." The isochemical phase diagram for the garnet rim in sample DH75B was created using the final effective bulk composition generated by Theriak-Domino. In this case, isopleths for the garnet compositions reported for garnet rims are overlain on the diagram, as well as matrix mineral compositions isopleths for ±0.01 An-content for plagioclase (Kohn et al. 2001). Intersecting isopleths are indicated by the polygon and labeled as "T-D rim." No data was available for the garnet transect for sample DH75A, so a high-resolution P-T path was not created, and the rock bulk composition (Table 3) was used for both core and rim panels. In the rim panels, data are compared to the conventional P-T conditions for the samples (grey polygon) using the same data reported by Kohn et al. (2001).

Figure 15. Isochemical phase diagrams from upper LHF samples DH58 (A) garnet core and (B) rim and (E) DH51 showing the mineral reactions only. The figure also includes isochemical phase diagrams from GHC sample DH61 (C) core and (D) rim, and DH60 (F) garnet rim data only. See Figures 4 and 5 for sample locations. Garnet-in reaction line (+Grt) and garnet growth contours (volume 0.5% increments) are overlaid on each diagram. Each diagram was created using the rock bulk compositions reported in Table 3 and the software program Theriak-Domino. Detailed caption is the same as in Figure 12. All labeled stability fields include quartz and H2O, except in panel (B), where the quartz-out reaction line is noted. The isopleths did not intersect in panels (B) and (F) but did in panel (D), as indicated by the polygon labeled as "T-D rim." In the rim panels, data are compared to the rim P-T conditions for the samples (labeled polygon) using the same data and conventional thermobarometric approaches by Kohn et al. (2001). No mineral data is available for sample DH51, so the isochemical phase diagram in panel (E) shows only

reaction lines with staurolite, sillimanite, garnet, and kyanite reaction lines in bold. This sample has co-existing kyanite and staurolite, so the shaded area indicates the field where both of these minerals are stable.

Figure 16. Isochemical phase diagrams from GHC samples (A) DH63, (B) DH66, and (C) DH67. See Figures 4 and 5 for sample locations. Garnet-in reaction line (+Grt) and garnet growth contours (volume 0.5% increments) are overlaid on each diagram. Each diagram was created using the rock bulk compositions reported in Table 3 and the software program Theriak-Domino. Some mineral stability fields are labeled using abbreviations after de Capitani and Petrakakis (2010). All labeled stability fields include quartz and H2O. For each diagram, isopleths of ±0.01-0.02 mole fraction spessartine (XMn), grossular (XCa), pyrope (XMg), almandine (XFe), and ±0.01-0.02 Mg-number (Mg/Fe+Mg, Mg#) of the compositional data point selected from the garnet's rim are overlain (Kohn et al., 2001). Isopleths of An-content for matrix plagioclase (A) and Mg# for matrix chlorite are also overlaid on the diagrams in panels (A) and (C), respectively. Mineral isopleths intersect in panels (A) and (B) as indicated by the polygon and labeled as "T-D rim." These isopleths did not intersect in panel (C). In each panel, data are compared to the rim P-T conditions for the samples (grey polygon) using the same data and conventional thermobarometric approaches by Kohn et al. (2001).

Figure 17. Summary of the P-T conditions and paths reported in Figures 12-16. In panels (A), (C), and (E), Gibb's P-T paths are shown as bold arrows and high-resolution P-T paths are labeled with core and rim points. In panels (B), (D), and (F), rim data generated using isopleth (white polygons) and conventional thermobarometry (grey polygons) are compared. Uncertainty scales in T (±25°C) and P (±1 kbar) are shown as insets in each panel.

Figure 18. (A) Thermal-kinematic model cross-section after Catlos et al. (2018) showing the MCT (dark line) and MBT (white line) from 25 to 8 Ma. The MCT and MBT sole into the MHT at depth. Isothermal sections in degree increments are indicated by the scale bar. The isotherms show the thermal situation at 18 Ma after MCT slip. Example sample trajectories on the diagram are represented by arrows with dots at the initial and heads at the final position. The MCT is active from 25 to 18 Ma, whereas slip transfers to the MBT from 15 to 8 Ma. (B) The model cross-section of the reactivation of the MCT shear zone from 8 to 2 Ma. Both the MCT and MCT-I sole into the MHT at depth. This panel represents the thermal situation at 6 Ma right before the development of MCT shear zone inverted metamorphism. Example sample trajectories are shown. (C) P-T diagram showing the trajectories of the model predictions for samples panels A and B and high-resolution P-T paths for the Darondi Khola samples. Sample DH75B is identified. Panels (D) and (E) show the same model predictions but high-resolution P-T paths from the Marsyangdi River (Catlos et al., 2018) and Bhagirathi River transects (Catlos et al., 2020).

Acknowledgments

I appreciate Matt Kohn (Boise State University) for supplying the data from the Darondi Khola samples and Mark Harrison (UCLA) for access to the rock samples so they could be subjected to further analysis. Discussions and assistance from Eric D. Kelly helped to refine the ideas in the manuscript. I thank Theresa Perez (UT Austin), who helped in generating some of the P-T diagrams and Jeffrey Horowitz (UT Austin) for drafting assistance. Comments from two reviewers improved the original version.

Data Availability Statement

Supplementary data used in the paper will be made available in the Texas Data Repository, a platform for publishing and sharing datasets, and is included here for review purposes only.

References

Abrajevitch, A.V., Ali, J., Aitchison, J.C., Badengzhu, Davis, A.M., Liu, J. & Ziabrev, S.V. (2005). Neotethys and the India–Asia collision: insights from a palaeomagnetic study of the Dazhuqu ophiolite, southern Tibet. Earth and Planetary Science Letters, 233, 87–102.

Acharyya, S.K. (1994). The Cenozoic foreland basin and tectonics of the eastern sub-Himalaya: problems and prospects. Himalayan Geology, 15, 3– 21.

Aharon, P., Schidlowski, M. & Singh, I. (1987). Chronostratigraphic markers in the end-Precambrian carbon isotope record of the Lesser Himalaya. Nature, 327, 699–702. https://doi.org/10.1038/327699a0

Ahmad, T., Harris, N., Bickle, M., Chapman, H., Bunbury, J., & Prince, C. (2000). Isotopic constraints on the structural relationships between the Lesser Himalayan Series and High Himalayan Crystalline Series, Garhwal Himalaya. Geological Society of America Bulletin, 112, 467-477.

Ahmad, T., Mukherjee P.K., & Trivedi, J.R. (1999). Geochemistry of Precambrian mafic magmatic rocks of the Western Himalaya, India: petrogenetic and tectonic implications. Chemical Geology, 160, 103-119.

Aikman, A.B., Harrison, T.M., & Lin, D. (2008). Evidence for Early (>44 Ma) Himalayan crustal thickening, Tethyan Himalaya, southeastern Tibet. Earth and Planetary Science Letters, 274, 14-23. https://doi.org/10.1016/j.epsl.2008.06.038

Aitchison, J.C., & Badengzhu, Davis, A.M., Liu. J., Luo,H., Malpas J.G., McDermid, I.R.C., Wu, H., Ziabrev, S.V., & Zhou, M-f. (2000). Remnants of a Cretaceous intra-oceanic subduction system within the Yarlung–Zangbo suture (southern Tibet). Earth and Planetary Science Letters, 183, 231–244.

Aitchison, J.C., Ali, J.R., & Davis, A.M. (2007). When and where did India and Asia collide? Journal of Geophysical Research, 112, B05423. https://doi.org/10.1029/2006JB004706

Allègre, C.J., et al. (1984). Structure and evolution of the Himalayan–Tibet orogenic belt. Nature, 307, 17-22.

Anczkiewicz, R., Chakraborty, S., Dasgupta, S., Mukhopadhyay, D., & Kołtonik, K. (2014). Timing, duration and inversion of prograde Barrovian metamorphism constrained by high resolution Lu–Hf garnet dating: A case study from the Sikkim Himalaya, NE India. Earth and Planetary Science Letters, 407, 70-81. https://doi.org/10.1016/j.epsl.2014.09.035

Arita, K. (1983). Origin of the inverted metamorphism of the Lower Himalaya, central Nepal. Tectonophysics, 95, 43-60.

Auden, M.A. (1937). The structure of the Himalaya in Garhwal. Records of the Geological Survey of India, 71, 407-433.

Bai, L., Liu, H.B., Ritsema, J. Mori, J., Zhang, T.Z., Ishikawa, Y., & Li, G.H. (2016). Faulting structure above the Main Himalayan Thrust as shown by relocated aftershocks of the 2015 Mw7.8 Gorkha, Nepal, earthquake. Geophysical Research Letters, 43, 637-642. https://doi.org/101002/2015GL066473

Bassoullet, J.P., Colchen, M., Juteau, T., Marcoux, J., & Mascle, G. (1980). L'edifice de nappes du Zanskar (Ladakh, Himalaya). Comptes rendus de l'Académie des Sciences, Series D, 290, 389-392.

1198 Baxter, A.T., Aitchison, J.C., Ali, J.R., Chan, J.S.-L., & Chan, G.H.N. (2016). Detrital chrome
1199 spinel evidence for a Neotethyan intra-oceanic island arc collision with India in the
1200 Paleocene. Journal of Asian Earth Sciences, 128, 90–104.
1201 Beaumont, C., Nguyen, M., Jamieson, R., & Ellis, S. (2006). Crustal flow modes in large hot
1202 orogens. In: Law, R.D., & Searle, M.P., & Godin, L. (Eds). Channel Flow, Ductile
1203 Extrusion and Exhumation in Continental Collision Zones. Geological Society, London,
1204 Special Publications, 268, 91–146.
1205 Beaumont, C., & Jamieson, R.A. (2010). Himalayan-Tibetan orogeny: channel flow versus
1206 (critical) wedge models, afalse dichotomy, in Leech, M.L., and others, eds., Proceedings
1207 for the 25th Himalaya-Karakoram-Tibet Workshop : U.S. Geological Survey, Open-File
1208 Report 2010-1099, 2p. http://pubs.usgs.gov/of/2010/1099/beaumont
1209 Beaumont, C., Jamieson, R.A., Nguyen, M.H., & Lee, B. (2001). Himalayan tectonics explained
1210 by extrusion of a low-viscosity crustal channel coupled to focused surface denudation.
1211 Nature, 414, 738– 742.
1212 Beaumont, C., Jamieson, R.A., Nguyen, M.H., & Medvedev, S. (2004). Crustal channel flows: 1.
1213 Numerical models with applications to the tectonics of the Himalayan–Tibetan orogen.
1214 Journal of Geophysical Research, 109. https://doi.org/10.1029/2003JB002809
1215 Benetti, B., Montomoli,C., Iaccarino, S., Langone, A., & Carosi, R. (2021). Mapping tectono-
1216 metamorphic discontinuities in orogenic belts: implications for mid-crust exhumation in
1217 NW Himalaya. Lithos, 392–393. https://doi.org/10.1016/j.lithos.2021.106129.
1218 Berman, R.G. (1990). Mixing properties of Ca-Mg-Fe-Mn garnets. American Mineralogist, 75,
1219 328-344.
1220 Bhandari, S., Xiao, W., Ao, S., Windley, B.F., Zhu, R., Li, R., Wang, H.Y.C., & Esmaeili, R.
1221 (2019). Rifting of the northern margin of the Indian craton in the Early Cretaceous:
1222 Insight from the Aulis Trachyte of the Lesser Himalaya (Nepal). Lithosphere, 11(5), 643–
1223 651. https://doi.org/10.1130/L1058.1
1224 Bhargava, O.N., & Bassi, U.K. (1994). The crystalline thrust sheets of the Himachal Himalaya
1225 and the age of amphibolite facies metamorphism. Journal of the Geological Society of
1226 India, 43, 343-352.
1227 Bhargava, O.N., & Singh, B.P. (2020). Geological evolution of the Tethys Himalaya. Episodes,
1228 43(1), 404-416. https://doi.org/10.18814/epiiugs/2020/020025
1229 Bhargava, O.N., Frank, W., & Bertle, R. (2011). Late Cambrian deformation in the Lesser
1230 Himalaya. Journal Asian Earth Sciences, 40, 201–212.
1231 Bhutani, R., Pande, K. & Venkatesan, T.R. (2004). Tectono-thermal evolution of India–Asia
1232 collision zone based on ^{40}Ar–^{39}Ar thermochronology in Ladakh, India. Proceedings of the
1233 Indian Academy of Sciences (Earth and Planetary Sciences), 113, 737–754.
1234 Bilham, R., Larson, K., Freymueller, J., & Project Idylhim members (1997). GPS measurements
1235 of present-day convergence across the Nepal Himalaya. Nature, 386, 61-64.
1236 Bodenhausen, J.W.A., DeBooy, T., Egelar, C.G., & Nijhuis, H.J. (1964). On the geology of
1237 Central west Nepal- A preliminary note. 22nd International Geological Congress, New
1238 Delhi. Special publication, 11, 101–122.
1239 Bollinger, L., Avouac, J., Cartin, R., & Pandey, M.R. (2004). Stress buildup in the Himalaya.
1240 Journal of Geophysical Research, 109, 1-8. https://doi.org/10.1029/2003JB002911
1241 Bollinger, L., Henry, P., & Avouac, J.P. (2006). Mountain building in the Nepal Himalaya:
1242 Thermal and kinematic model. Earth and Planetary Science Letters, 244, 58–71.

1243 Bollinger, L., Soma Nath Sapkota, S.N., P. Tapponnier, P., Yann Klinger, Y., Magali Rizza, M.,
1244 et al. (2014). Estimating the return times of great Himalayan earthquakes in eastern
1245 Nepal: Evidence from the Patu and Bardibas strands of the Main Frontal Thrust. Journal
1246 of Geophysical Research, 119(9), 7123-7163.
1247 Bora, D. S., & Shukla, U. K. (2005). Petrofacies implication for the Lower Siwalik Foreland
1248 Basin evolution, Kumaun Himalaya, India. Special Publication of the Palaeontological
1249 Society of India, 2, 163–179.
1250 Bordet, P., Colchen, M., & LeFort. P. (1971). Esquisse géologique = Geological sketch map Nyi-
1251 Shang (Népal central) / Mission géologiques du centre national de la recherche
1252 scientifique (R.C.P. Nepal) avec le patronage de la Fédération française de la montagne et
1253 du Club Alpin ; les contours géologiques ont été levés par P. Bordet, M. Colchen, P. Le
1254 Fort, ca. 1:75 000 (E 83°50'--E 84°15'/N 28°49'--N 28°32').
1255 https://www.sudoc.fr/131377973
1256 Bordet, P., Colchen, M., & LeFort. P. (1975). Recherches geologiques dans l'Himalaya du Nepal,
1257 region du Nyi-Shang. Paris Centre National de la Recherche Scientifique, 138pp.
1258 Braden, Z., Godin, L., & Cottle, J.M. (2017). Segmentation and rejuvenation of the Greater
1259 Himalayan sequence in western Nepal revealed by in situ U–Th/Pb monazite
1260 petrochronology, Lithos, 284–285, 751-765. https://doi.org/10.1016/j.lithos.2017.04.023
1261 Braden, Z., Godin, L., Cottle, J., & Yakymchuk, C. (2018). Renewed late Miocene (< 8 Ma),
1262 hinterland ductile thrusting, western Nepal Himalaya. Geology, 46, 503-506.
1263 Brookfield, M.E. (1993). The Himalayan passive margin from Precambrian to Cretaceous.
1264 Sedimentary Geology, 84, 1–35.
1265 Brookfield, M.E., & Reynolds, P.H. (1981). Late Cretaceous emplacement of the Indus suture
1266 zone ophiolitic melanges and an Eocene–Oligocene magmatic arc on the northern edge of
1267 the Indian plate. Earth and Planetary Science Letters, 55, 157–162.
1268 Brunel, M. & Kienast, J.R. (1986). Etude pétro-structurale des chevauchements ductiles
1269 himalayens sur la transversale de l'Everest-Makalu (Nepal oriental). Canadian Journal of
1270 Earth Sciences, 23, 1117-1137.
1271 Burchfiel, C.B., Zhiliang C., Hodges K.V., Yuping L., Royden L.H., Changrong D., & Jiene X.
1272 (1992). The South Tibetan Detachment System, Himalayan orogen: extension
1273 contemporaneous with and parallel to shortening in a collisional mountain belt. USGS
1274 Special Paper, 269, 1-40.
1275 Burg, J.-P. (2011). The Asia–Kohistan–India collision: Review and discussion. In: Brown, D. &
1276 Ryan, P.D. (eds) Arc–Continent Collision. Frontiers in Earth Sciences. Springer, Berlin,
1277 279–309.
1278 Burg, J.-P., Brunel, M., Gapais, D., Chen G.M., & Liu, G.H. (1984). Deformation of
1279 leucogranites of the crystalline Main Central Sheet in southern Tibet (China). Journal of
1280 Structural Geology, 6, 535-542.
1281 Burg, J.-P., Leyreloup, A., Girardeau, J., & Chen, G.M. (1987). Structure and metamorphism of
1282 a tectonically thickened continental crust—the Yalu Tsangpo suture zone (Tibet).
1283 Philosophical Transactions of the Royal Society of London Series A, 321, 67– 86.
1284 Burgess, W.P., Yin, A., Dubey, C.S., Shen, Z-K., & Kelty, T.K. (2012). Holocene shortening
1285 across the Main Frontal Thrust zone in the eastern Himalaya. Earth and Planetary Science
1286 Letters, 357–358, 152-167. https://doi.org/10.1016/j.epsl.2012.09.040
1287 Caddick, M.J., Bickle, M.J., Harris, N.B.W., Holland, T.J.B., Horstwood, M.S.A., Parrish, R.R.,
1288 & Ahmad, T. (2007). Burial and exhumation history of a Lesser Himalayan schist:

recording the formation of an inverted metamorphic sequence in NW India. Earth and Planetary Science Letters, 264, 375-90. https://doi.org/10.1016/j.epsl.2007.09.011

Caldwell, W.B., Klemperer, S.L., Lawrence, J.F., & Rai, S.S. (2013). Characterizing the Main Himalayan Thrust in the Garhwal Himalaya, India with receiver function CCP stacking. Earth and Planetary Science Letters, 367, 15-27. https://doi.org/10.1016/j.epsl.2013.02.009

Cao, H., Huang, Y., Li, G., Zhang, L., Wu, J., Dong, L., Dai, Z., & Lu, L. (2018). Late Triassic sedimentary records in the northern Tethyan Himalaya: Tectonic link with Greater India. Geoscience Frontiers, 9(1), 273-291. https://doi.org/10.1016/j.gsf.2017.04.001

Carlson, W. D. (1989). The significance of intergranular diffusion to the mechanisms and kinetics of porphyroblast crystallization. Contributions to Mineralogy and Petrology, 103, 1–24.

Carlson, W. D. (2002). Scales of disequilibrium and rates of equilibration during metamorphism. American Mineralogist, 87, 185–204.

Carosi, R., Lombardo, B., Molli, G., Musumeci, G., & Pertusati, P.C. (1998).The South Tibetan Detachment System in the Rongbuk valley, Everest region. Deformation and geological implications. Journal of Asian Earth Sciences, 16, 299-311.

Carosi, R., Lombardo, B., Musumeci, G., & Pertusati, P.C. (1999a).Geology of the Higher Himalayan Crystallines in Khumbu Himal (eastern Nepal). Journal of Asian Earth Sciences, 17, 785-803.

Carosi, R., Montomoli, C., & Iaccarino, S. (2018). 20 years of geological mapping of the metamorphic core across Central and Eastern Himalayas. Earth-Science Reviews, 177, 124–138. https://doi.org/10.1016/j.earscirev.2017.11.006

Carosi, R., Montomoli, C., Iaccarino, S., Massonne, H. J., Rubatto, D., Langone, A., et al. (2016). Middle to late Eocene exhumation of the Greater Himalayan sequence in the central Himalayas: Progressive accretion from the Indian plate. Bulletin of the Geological Society of America, 128, 1571–1592. https://doi.org/10.1130/B31471.1

Carosi, R., Montomoli, C., Rubatto, D., & Visonà, D. (2010). Late Oligocene high-temperature shear zones in the core of the Higher Himalayan Crystallines (Lower Dolpo, western Nepal), Tectonics, 29, TC4029. https://doi.org/10.1029/2008TC002400

Carosi, R., Montomoli, C., Rubatto, D., & Visonà, D. (2013).Leucogranite intruding the South Tibetan Detachment in western Nepal: implications for exhumation models in the Himalayas. Terra Nova, 25, 478– 489, 2013

Carosi, R., Musumeci, G., & Pertusati, P.C. (1999b). Extensional tectonics in the higher Himalayan crystallines of Khumbu Himal, Eastern Nepal. In Macfarlane, A., Sorkhabai, R.B., and Quade, J. (Eds.), Himalaya and Tibet: Mountain roots to mountain tops. Geological Society of America Special Paper, 328, pp. 211-223.

Catlos, E.J. (2013). Versatile Monazite: resolving geological records and solving challenges in materials science: Generalizations about monazite: Implications for geochronologic studies. American Mineralogist, 98 (5-6), 819–832. https://doi.org/10.2138/am.2013.4336

Catlos, E.J., Dubey, C.S., Marston, R.A., & Harrison, T.M. (2007). Geochronologic constraints across the Main Central Thrust shear zone, Bhagirathi River (NW India): Implications for Himalayan tectonics. In M. Cloos, W.D. Carlson, M.C. Gilbert, J.G. Liou, S.S. Sorensen, Eds., Convergent Margin Terranes and Associated Regions: A Tribute to W.G. Ernst. Geological Society of America Bulletin, 419, 135-151. https://doi.org/10.1130/SPE419.

Catlos, E. J., Perez, T. J., Lovera, O. M., Dubey, C. S., Schmitt, A. K., & Etzel, T. M. (2020). High-resolution P-T-Time paths across Himalayan faults exposed along the Bhagirathi transect NW India: Implications for the construction of the Himalayan orogen and ongoing deformation. Geochemistry, Geophysics, Geosystems, 21, e2020GC009353. https://doi.org/10.1029/2020GC009353

Catlos, E.J., Harrison, T.M., Kohn, F.J., Grove, Z.M., Ryerson, F.J., Manning, C.E., & Upreti, B.N. (2001). Geochronologic and thermobarometric constraints on the evolution of the Main Central Thrust, central Nepal Himalaya. Journal of Geophysical Research, 106, 16177-16204. https://doi.org/10.1029/2000JB900375

Catlos, E.J., Harrison, T.M., Manning, C.E., Grove, M., Rai, S.M., Hubbard, M.S., & Upreti, B.N. (2002). Records of the evolution of the Himalayan Orogen from in situ Th-Pb ion microprobe dating of monazite; eastern Nepal and western Garhwal. Journal of Asian Earth Sciences, 20, 459-479. https://doi.org/10.1016/S1367-9120(01)00039-6

Catlos, E.J., Lovera, O.M., Kelly, E.D., Ashley, K.T., Harrison, T.M., & Etzel, T. (2018). Modeling High-resolution Pressure-Temperature paths across the Himalayan Main Central Thrust (central Nepal): Implications for the dynamics of collision. Tectonics, 37, 2363-2388.

Catlos, E.J., Pease, E.C., Dygert, N., Brookfield, M., Schwarz, W.H., Bhutani, R., Pande, K., & Schmitt, A.K. (2019). Nature, age and emplacement of the Spongtang ophiolite, Ladakh, NW India. Journal of the Geological Society, 176, 284-305. https://doi.org/10.1144/jgs2018-085

Cattin, R., & Avouac, J. (2000). Modeling mountain building and the seismic cycle in the Himalaya of Nepal. Journal of Geophysical Research, 105, 13389-13407. https://doi.org/10.1029/2000JB900032

Cawood, P.A., Johnson, M.R.W., & Nemchin, A.A. (2007).Early Palaeozoic orogenesis along the Indian margin of Gondwana: Tectonic response to Gondwana assembly. Earth and Planetary Science Letters, 255, 70-84. https://doi.org/10.1016/j.epsl.2006.12.006

Chakraborty, S., Anczkiewicz, R., Gaidies, F., Rubatto, D., Sorcar, N., Faak, K., Mukhopadhyay, D., & Dasgupta D. (2016).A review of thermal history and timescales of tectonometamorphic processes in Sikkim Himalaya (NE India).and implications for rates of metamorphic processes. Journal of Metamorphic Geology, 34, 785-803. https://doi.org/10.1111/jmg.12200

Chakraborty, S., Mukul, M., Mathew, G., & Pande, K. (2019).Major shear zone within the Greater Himalayan Sequence and sequential evolution of the metamorphic core in Sikkim, India. Tectonophysics, 770, 228183. https://doi.org/10.1016/j.tecto.2019.228183

Chen, X., Schertl, H-P., Gu, P., Zheng, Y., Xu, R., Zhang, J., Cai, P., & Lin, C. (2021).Newly discovered MORB-Type HP garnet amphibolites from the Indus-Yarlung Tsangpo suture zone: Implications for the Cenozoic India–Asia collision, Gondwana Research, 90, 102-117. https://doi.org/10.1016/j.gr.2020.11.006

Chirouze, F., Dupont-Nivet, G., Huyghe, P., van der Beek, P., Chakraborti, T., Bernet, M., & Erens, V. (2012).Magnetostratigraphy of the Neogene Siwalik Group in the far eastern Himalaya: Kameng section, Arunachal Pradesh, India. Journal of Asian Earth Sciences, 44, 117-135. https://doi.org/10.1016/j.jseaes.2011.05.016

Colchen, M., Le Fort, P., and Pêcher, A. (1980). Annapurna-Manaslu-Ganesh Himal,Centre National de la Recherches Scientifiques, Paris, 136pp.

1379 Coleman, M.E. (1996). Orogen-parallel and orogen-perpendicular extension in the central
1380 Nepalese Himalayas. Geological Society of America Bulletin, 108, 1594-1607.
1381 Coleman, M.E., & Hodges, K.V. (1998). Contrasting Oligocene and Miocene thermal histories
1382 from the hanging wall and footwall of the South Tibetan detachment in the central
1383 Himalaya from $^{40}Ar/^{39}Ar$ thermochronology, Marsyandi Valley, central Nepal. Tectonics,
1384 17(5), 726– 740. https://doi.org/10.1029/98TC02777.
1385 Cooper, F.J., Adams, B.A., Edwards, C.S., & Hodges, K.V. (2012). Large normal-sense
1386 displacement on the South Tibetan fault system in the eastern Himalaya. Geology, 40
1387 (11), 971–974. https://doi.org/10.1130/G33318.1
1388 Copley, A., Avouac, J.-P., & Royer, J.-Y. (2010). India-Asia collision and the Cenozoic
1389 slowdown of the Indian plate: Implications for the forces driving plate motions. Journal
1390 of Geophysical Research, 115, B03410. https://doi.org/10.1029/2009JB006634
1391 Corfield, R.L., & Seale, M.P. (2000). Crustal shortening across the north Indian continental
1392 margin, Ladakh, India. In: Khan, M.A., Treloar, P.J., Searle, M.P., Jan, M.Q. (Eds.),
1393 Tectonics of the Nanga Parbat syntaxis and the Western Himalaya. The Geological
1394 Society Special Publication, vol. 170, pp. 395– 410.
1395 Corrie, S.L., & Kohn, M.J. (2011). Metamorphic history of the central Him alaya, Annapurna
1396 region, Nepal, and implications for tectonic models, Geological Society of America
1397 Bulletion, 123(9–10), 1863– 1879.
1398 Corrie, S.L., Kohn, M.J., McQuarrie, N., & Long S. (2012). Flattening the Bhutan Himalaya.
1399 Earth and Planetary Science Letters, 349-350, 67-74.
1400 Corrie, S.L., Kohn, M.J., & Vervoort, J.D. (2010). Young eclogite from the Greater Himalayan
1401 Sequence, Arun Valley, eastern Nepal; P-T-t path and tectonic implications. Earth and
1402 Planetary Science Letters, 289, 406-416. https://doi.org/10.1016/j.epsl.2009.11.029
1403 Cottle, J.M., Larson, K.P., & Kellett, D.A. (2015).How does the mid-crust accommodate
1404 deformation in large, hot collisional orogens? A review of recent research in the
1405 Himalayan orogen. Journal of Structural Geology, 78, 119-133.
1406 https://doi.org/10.1016/j.jsg.2015.06.008
1407 Cottle, J.M., Searle, M.P., Horstwood, M.S.A. & Waters, D. (2009). Timing of midcrustal
1408 metamorphism, melting, and deformation in the Mount Everest region of south Tibet
1409 revealed by U(-Th)-Pb geochronology. The Journal of Geology, 117, 643–664.
1410 Craddock Affinati, A., Hoisch, T.D., Wells, M.L., & Vervoort, J.D. (2020). Pressure-
1411 temperature-time paths from the Funeral Mountains, California, reveal Jurassic retroarc
1412 underthrusting during early Sevier orogenesis. Geological Society of America Bulletin,
1413 132 (5-6), 1047–1065. https://doi.org/10.1130/B35095.1
1414 Crouzet, C., Dunkl, I., Paudel, L., Árkai, P., Rainer, T.M., Balogh, K., & Appel, E. (2007).
1415 Temperature and age constraints on the metamorphism of the Tethyan Himalaya in
1416 Central Nepal: A multidisciplinary approach. Journal of Asian Earth Sciences, 30(1),
1417 113-130. https://doi.org/10.1016/j.jseaes.2006.07.014
1418 Dai, J.-G., Wang, C.-S., Hébert, R., Santosh, M., Li, Y.-L. & Xu, J.-Y. (2011). Petrology and
1419 geochemistry of peridotites in the Zhongba ophiolite, Yarlung Zangbo Suture Zone:
1420 Implications for the Early Cretaceous intra-oceanic subduction zone within the Neo-
1421 Tethys. Chemical Geology, 288, 133–148.
1422 Daniel, C.G., Hollister, L.S., Parrish, R.R., & Grujic, D. (2003). Exhumation of the Main Central
1423 Thrust from lower crustal depths, eastern Bhutan Himalaya. Journal of Metamorphic
1424 Geology, 21(4), 317–334. https://doi.org/10.1046/j.1525-1314.2003.00445.x

Dasgupta, S., Ganguly, J., & Neogi, S. (2004). Inverted metamorphic sequence in the Sikkim Himalayas: crystallization history, P–T gradient and implications. Journal of Metamorphic Geology, 22, 395-412. https://doi.org/10.1111/j.1525-1314.2004.00522.x

de Capitani, C., & Brown, T.H. (1987).The computation of chemical equilibrium in complex systems containing non-ideal solutions. Geochimica et Cosmochimica Acta, 51, 2639–2652.

de Capitani, C., & Petrakakis, K. (2010). The computation of equilibrium assemblage diagrams with Theriak/Domino software. American Mineralogist, 95, 1006-1016. https://doi.org/10.2138/am.2010.3354

DeCelles, P.G. (2015). Structural-kinematic setting of the 2015 Gorkha, Nepal earthquakes: Lessons from a critically tapered orogenic wedge. 2015 GSA Annual Meeting in Baltimore, Maryland, USA (1-4 November 2015), Paper No. 105-9. https://gsa.confex.com/gsa/2015AM/webprogram/Paper266639.html

DeCelles, P.G., Carrapa, B., Ojha, T.P., Gehrels, G.E., & Collins, D. (2020). Structural and Thermal Evolution of the Himalayan Thrust Belt in Midwestern Nepal. Geological Society of America Special Paper, 547, 1-77. https://doi.org/10.1130/2020.2547(01)

DeCelles, P.G., Gehrels, G.E., Najman, Y., Martin, A.J., Carter, A., & Garzanti, E. (2004). Detrital geochronology and geochemistry of Cretaceous–Early Miocene strata of Nepal: implications for timing and diachroneity of initial Himalayan orogenesis. Earth and Planetary Science Letters, 227, 313– 330.

DeCelles, P.G., Gehrels, G.E., Quade, J., LaReau, B., & Spurlin, M. (2000). Tectonic implications of U–PL zircon ages of the Himalayan orogenic belt in Nepal. Science 288, 497–499.DeCelles, P.G., Robinson, D.M., Quade, J., Ojha, T.P., Garzione, C.N., Copeland, P., Upreti, B.N., 2001. Stratigraphy, structure, and tectonic evolution of the Himalayan fold-thrust belt in western Nepal. Tectonics, 20, 487–509.

Denolle, M.A., Fan, W., & Shearer, M. (2015). Dynamics of the 2015 M7.8 Nepal earthquake. Geophysical Research Letters, 42, 7467-7475. https://doi.org/10.1002/2015GL065336

Dewey, J.F., & Bird, J.M. (1970). Mountain belts and new global tectonics. Journal of Geophysical Research, 75, 2625– 2685.

Dey, S., Dasgupta, P., Das, K., & Matin, A. (2020). Neoproterozoic Blaini Formation of Lesser Himalaya, India: Fiction and Fact. Geological Society of America Bulletin, 132 (11-12), 2267–2281. https://doi.org/10.1130/B35483.1

Dhamodharan, S., Rawat, G., Kumar, S., & Bagri, D.S. (2020). Sedimentary thickness of the northern Indo-Gangetic plain inferred from magnetotelluric studies. Journal of Earth System Sciences, 129, 156-168. https://doi.org/10.1007/s12040-020-01422-z

Ding, L., Kapp, P., & Wan, X.Q. (2005). Paleocene–Eocene record of ophiolite obduction and initial India–Asia collision, south central Tibet. Tectonics 24, TC3001. https://doi.org/10.1029/2004TC001729

DiPietro, J.A., & Pogue, K.R. (2004). Tectonostratigraphic subdivisions of the Himalaya: a view from the west. Tectonics 23, TC5001. https://doi.org/10.1029/2003TC001554

Dubey, A.K. (1997). Simultaneous development of noncylindrical folds, frontal ramps and transfer faults in a compressional regime-experimental investigation of Himalayan examples. Tectonics, 16, 336–346.

Dunkl, I., AntolÍn, B., Wemmer, K., Rantitsch, G., Kienast, M., Montomoli, C., Ding, L., Carosi, R., Appel, E., El Bay, R., Xu, Q., & Von Eynatten, H. (2011). Metamorphic evolution of

1470 the Tethyan Himalayan flysch in SE Tibet. Geological Society, London, Special
1471 Publications, 353, 45-69. https://doi.org/10.1144/SP353.4
1472 Duputel, Z., Vergne, J., Rivera, L., Wittlinger, G., Farra, V., & Hetényi, G. (2016). The 2015
1473 Gorkha earthquake: A large event illuminating the Main Himalayan Thrust fault.
1474 Geophysical Research Letters, 43, 2517-2525. https://doi.org/10.1002/2016GL068083
1475 Dyck, B., St-Onge, M., & Searle, M.P., Rayner, N., Waters, D., & Weller, O.M. (2018). Protolith
1476 lithostratigraphy of the Greater Himalayan Series in Langtang, Nepal: implications for
1477 the architecture of the northern Indian margin. Geological Society, London, Special
1478 Publications, 483, 281-304. https://doi.org/10.1144/SP483.9
1479 Elliott, J., Jolivet, R., González, P.J., Avouac, J-P., Hollingsworth, J., Searle, M., & Stevens, L.
1480 (2016). Himalayan megathrust geometry and relation to topography revealed by the
1481 Gorkha earthquake. Nature Geoscience, 9, 174-180. https://doi.org/10.1038/ngeo2623
1482 England, P.C., & Molnar, P. (1993). The interpretation of inverted metamorphic isograds using
1483 simple physical calculations. Tectonics, 12, 145-157.
1484 England, P.C., Le Fort P., Molnar P., & Pêcher, A. (1992). Heat sources for Tertiary
1485 metamorphism and anatexis in the Annapurna-Manaslu region, central Nepal. Journal of
1486 Geophysical Research, 97, 2107-2128.
1487 Ernst, W.G. (1973). Blueschist metamorphism and P-T regimes in active subduction zones.
1488 Tectonophysics, 17, 255.
1489 Etzel, T. M., Catlos, E. J., Ataktürk, K., Lovera, O. M., Kelly, E. D., Çemen, I., & Diniz, E.
1490 (2019). Implications for thrust-related shortening punctuated by extension from P-T paths
1491 and geochronology of garnet-bearing schists, Southern (Çine) Menderes Massif, SW
1492 Turkey. Tectonics, 38, 1974– 1998. https://doi.org/10.1029/2018TC005335
1493 Ferry, J.M., & Spear, F.S. (1978). Experimental calibration of partitioning of Fe and Mg between
1494 biotite and garnet. Contributions to Mineralogy and Petrology, 66, 113-117.
1495 Fuchs, G. (1987). The Geology of southern Zanskar (Ladakh) - Evidence for the autochthony of
1496 the Tethys Zone of the Himalaya. Jahrbuch der Geologischen Bundesanstalt-A, 130, 465-
1497 491.
1498 Fuchs, G., & Linner, M. (1995). Geological traverse across the western Himalaya- a contribution
1499 to the geology of eastern Ladakh, Lahul, and Chamba. Jahrbuch der Geologischen
1500 Bundesanstalt-A., 138, 655-685.
1501 Fuchs, G., Widder, R.W., & Tuladhar, R. (1988). Contributions to the Geology of the Annapurna
1502 Range [Manang Area, Nepal]. Jahrbuch der Geologischen Bundesanstalt-A, 131, 593-
1503 607.
1504 Gaidies, F., de Capitani, C. & Abart, R. (2008). THERIA_G: a software program to numerically
1505 model prograde garnet growth. Contributions to Mineralogy and Petrology, 155, 657–
1506 671. https://doi.org/10.1007/s00410-007-0263-z
1507 Gaidies, F., Petley-Ragan, A., Chakraborty, S., Dasgupta, S., & Jones, P. (2015). Constraining
1508 the conditions of barrovian metamorphism in Sikkim, India: P-T-t paths of garnet
1509 crystallization in the Lesser Himalayan Belt. Journal of Metamorphic Geology, 33(1),
1510 23–44. https://doi.org/10.1111/jmg.12108
1511 Gansser, A. (1964). The Geology of the Himalayas. Wiley Interscience, New York, 289 pp.
1512 Gansser, A. (1981). The geodynamic history of the Himalaya. In Gupta, H.K., and Delany, F.M.,
1513 (Eds.), Zagros, Hindu Kush, Himalayan Geodynamic Evolution. American Geophysical
1514 Union, 3, pp. 111-121.

1515 Gao, L-E., Zeng, L., Gao, J., Shang, Z., Hou, K., & Wang, Q. (2016). Oligocene crustal anatexis
1516 in the Tethyan Himalaya, southern Tibet. Lithos, 264, 201-209.
1517 https://doi.org/10.1016/j.lithos.2016.08.038
1518 Garzanti, E. (1999). Stratigraphy and sedimentary history of the Nepal Tethys Himalaya passive
1519 margin. Journal Asian Earth Science, 17, 805–827.
1520 Garzanti, E., & Pagni Frette, M. (1991). Stratigraphic succession of the Thakkhola region
1521 (central Nepal)- Comparison with the Northwestern Tethys Himalaya. Rivista Italiana di
1522 Paleontologia e Stratigrafia, 97(1). https://doi.org/10.13130/2039-4942/8980
1523 Gehrels, G.E., DeCelles, P.G., Martin, A., Ojha, T.P., Pinhassi, G., & Upreti, B.N. (2003).
1524 Initiation of the Himalayan Orogen as an early Paleozoic thin-skinned thrust belt.
1525 Geological Society of America Today, 13, 4-9.
1526 Gehrels, G.E., P.G. DeCelles, T.P. Ojha, & B. N. Upreti (2006). Geologic and U-Th-Pb
1527 geochronologic evidence for early Paleozoic tectonism in the Kathmandu thrust sheet,
1528 central Nepal Himalaya. Geological Society of America Bulletin, 118, 185–198.
1529 Gervais, F., & Brown, R.L. (2011). Testing modes of exhumation in collisional orogens:
1530 Synconvergent channel flow in the southeastern Canadian Cordillera. Lithosphere, 3, 55–
1531 75. https://doi.org/10.1130/L98.1
1532 Ghosh, S., Sanyal, P., Sangode, S.J., & Nanda, A.C. (2018). Substrate control of C4 plant
1533 abundance in the Himalayan foreland: A study based on inter-basinal records from Plio-
1534 Pleistocene Siwalik Group sediments. Palaeogeography, Palaeoclimatology,
1535 Palaeoecology, 511, 341–351.
1536 Gibson, R., Godin, L., Kellett, D.A., Cottle, J.M., & Archibald, D. (2016). Diachronous
1537 deformation along the base of the Himalayan metamorphic core, west-central Nepal.
1538 GSA Bulletin, 128 (5-6), 860–878. https://doi-org/10.1130/B31328.1
1539 Gnos, E., Immenhauser, A., Peters, Tj. (1997). Late Cretaceous/early Tertiary convergence
1540 between the Indian and Arabian plates recorded in ophiolites and related sediments.
1541 Tectonophysics, 271(1–2), 1-19. https://doi.org/10.1016/S0040-1951(96)00249-1
1542 Godin, L., Brown, R.L., & Hanmer, S. (1999b). High strain zone in the hanging wall of the
1543 Annapurna detachment, central Nepal Himalaya. In Macfarlane, A., Sorkhabi, R.B., &
1544 Quade, J., (Eds.), Himalaya and Tibet: Mountain roots to mountain tops. Geological
1545 Society of America Special Paper, 328, pp. 199-210.
1546 Godin, L., Brown, R.L., Hanmer, S., & Parrish, R.R. (1999a). Back folds in the Himalayan
1547 orogen: an alternative interpretation. Geology, 27, 151-154.
1548 Goscombe, B., & Hand, M. (2000). Contrasting P-T paths in the eastern Himalaya, Nepal:
1549 Inverted isograds in a paired metamorphic mountain belt. Journal of Petrology, 41(12),
1550 1673–1719. https://doi.org/10.1093/petrology/41.12.1673
1551 Goscombe, B., Gray, D., & Hand, M. (2006). Crustal architecture of the Himalayan metamorphic
1552 front in eastern Nepal. Gondwana Research, 10(3–4), 232-255.
1553 https://doi.org/10.1016/j.gr.2006.05.003.
1554 Goswami, P.K., & Deopa, T. (2017). Petrotectonic setting of the provenance of Lower Siwalik
1555 sandstones of the Himalayan foreland basin, southeastern Kumaun Himalaya, India.
1556 Island Arc, 27:e12242. https://doi.org/10.1111/iar.12242
1557 Goswami-Banerjee, S., Bhowmik, S. K., Dasgupta, S., & Pant, N. C. (2014). Burial of thermally
1558 perturbed Lesser Himalayan mid-crust: Evidence from petrochemistry and P-T estimation
1559 of the western Arunachal Himalaya, India. Lithos, 208-209, 298–311.
1560 https://doi.org/10.1016/j.lithos.2014.09.015

1561 Graham, C.M., & England, P.C. (1976). Thermal regimes and regional metamorphism in the
1562 vicinity of overthrust faults: an example of shear heating and inverted metamorphic
1563 zonation from southern California. Earth and Planetary Science Letters, 31, 142-152.
1564 Graham, C.M., & Powell, R. (1984). A garnet-hornblende geothermometer; calibration, testing,
1565 and application to the Pelona Schist, Southern California. Journal of Metamorphic
1566 Geology, 2, 13-31.
1567 Grasemann B., & Vannay J-C. (1999). Flow controlled inverted metamorphism in shear zones.
1568 Journal of Structural Geology, 21, 743-750.
1569 Groppo, C., Rolfo, F., & Lombardo, B. (2009). P-T evolution across the Main Central Thrust
1570 Zone (eastern Nepal): Hidden discontinuities revealed by petrology. Journal of Petrology,
1571 50(6), 1149–1180. https://doi.org/10.1093/petrology/egp036
1572 Groppo, C., Rubatto, D., Rolfo, F., & Lombardo, B. (2010). Early Oligocene partial melting in
1573 the Main Central Thrust Zone (Arun valley, eastern Nepal Himalaya). Lithos, 118(3-4),
1574 287–301. https://doi.org/10.1016/j.lithos.2010.05.003
1575 Grujic, D., Casey, M., Davidson, C., Hollister, L.D., Kündig, R., Pavlis, T., & Schmid, S. (1996).
1576 Ductile extrusion of the Higher Himalayan Crystalline in Bhutan: evidence from quartz
1577 microfabrics. Tectonophysics, 260(1–3), 21-43. https://doi.org/10.1016/0040-
1578 1951(96)00074-1
1579 Guillot, S. (1999). An overview of the metamorphic evolution in Central Nepal. Journal of Asian
1580 Earth Sciences, 17, 713-725.
1581 Guillot, S., Cosca, M., Allemand, P., & LeFort, P. (1999). Contrasting metamorphic and
1582 geochronologic evolution along the Himalayan belt. In: Macfarlane, A., Sorkhabi, R.B.,
1583 Quade, J. (Eds.), Himalaya and Tibet: Mountain Roots to Mountain Tops. Geological
1584 Society of America Special Papers, vol. 328, pp. 117– 128.
1585 Guillot, S., LeFort, P., Peˆcher, A., Barman, M.R., & Aprahmaian, J. (1995). Contact-
1586 metamorphism and depth of emplacement of the Manaslu granite (Central Nepal)—
1587 implications for Himalayan orogenesis. Tectonophysics, 241, 99– 119.
1588 Guillot, S., Mahéo, G., de Sigoyer, J., Hattori, K.H., & Pêcher, A. (2008). Tethyan and Indian
1589 subduction viewed from the Himalayan high- to ultrahigh-pressure metamorphic rocks.
1590 Tectonophysics, 451, 225-241.
1591 Gupta, D.K., Bhowmick, D., & Roy, N.S. (2015). Himalayan hazard study on the basis of stress
1592 and strain state of 1991 Uttarkashi earthquake using Coulomb stress transfer model.
1593 Geomatics, Natural Hazards and Risk, 6, 131-148.
1594 https://doi.org/10.1080/19475705.2013.820797
1595 Guynn, J.H., Kapp, P., Pullen, A., Gehrels, G., Heizler, M. & Ding, L. (2006). Tibetan basement
1596 rocks near Amdo reveal “missing” Mesozoic tectonism along the Bangong suture, central
1597 Tibet. Geology, 34, 505-508.
1598 Harris, N., Inger, S., & Massey, J. (1993). The role of fluids in the formation of High Himalayan
1599 leucogranites. In Trealor, P.J., & Searle, M.P., (Eds.), Himalayan Tectonics. Geological
1600 Society Special Publication, 74, pp. 391-400.
1601 Harris, N., & Massey, J. (1994).Decompression and anatexis of Himalayan metapelites.
1602 Tectonics, 13(6), 1537– 1546. https://doi.org/10.1029/94TC01611
1603 Harrison, T.M., Grove M., Lovera O.M., & Catlos E.J. (1998). A model for the origin on
1604 Himalayan anatexis and inverted metamorphism. Journal of Geophysical Research, 103,
1605 27017-27032.

Harrison, T.M., Grove, M., Lovera, O.M., Catlos, E.J., & D'Andrea, J. (1999). The origin of Himalayan anatexis and inverted metamorphism: Models and constraints. Journal of Asian Earth Sciences, 17, 755-772.

Harrison, T.M., McKeegan, K.D., & LeFort, P. (1995). Detection of inherited monazite in the Manaslu leucogranite by 208Pb232Th ion microprobe dating: Crystallization age and tectonic implications. Earth and Planetary Science Letters, 133(3–4), 271-282. https://doi.org/10.1016/0012-821X(95)00091-P.

Hazarika, D., Wadhawan M., Paul, A., Kumar, N., & Borah, K. (2017). Geometry of the Main Himalayan Thrust and Moho beneath Satluj valley, northwest Himalaya: Constraints from receiver function analysis. Journal of Geophysical Research, 122, 2929-2945. https://doi.org/10.1002/2016JB013783

He, P., Lei, J., Yuan, X., Xu, X., Xu, Q., Liu, Z., Mi, Q., & Zhou, L. (2018). Lateral Moho variations and the geometry of the Main Himalayan Thrust beneath the Nepal Himalayan orogen revealed by teleseismic receiver functions. Geophysical Journal International, 214, 1004-1017. https://doi.org/10.1093/gji/ggy192

Hébert, R., Bezard, R., Guilmette, C., Dostal, J., Wang, C.S. & Liu, Z.F. (2012). The Indus–Yarlung Zangbo ophiolites from Nanga Parbat to Namche Barwa syntaxes, southern Tibet: First synthesis of petrology, geochemistry, and geochronology with incidences on geodynamic reconstructions of Neo-Tethys. Gondwana Research, 22, 337–397.

Heim, A.A., & Gansser, A. (1939) The Throne of the Gods; An Account of the First Swiss Expedition to the Himalayas. New York: The Macmillan Company, 262 pp. ASIN:B000856X12

Henry, P., Le Pichon, X., & Goffe, B. (1997). Kinematic, thermal and petrological model of the Himalayas: Constraints related to metamorphism within the underthrust Indian crust and topographic elevation. Tectonophysics, 273, 31-56.

Herman, F., Copeland, P., Avouac, J. , Bollinger, L., Mahéo, G., Le Fort, P., et al. (2010). Exhumation, crustal deformation, and thermal structure of the Nepal Himalaya derived from the inversion of thermochronological and thermobarometric data and modeling of the topography. Journal of Geophysical Research, 115, B06407. https://doi.org/10.1029/2008JB006126

Hirschmiller, J., Grujic, D., Bookhagen, B., Coutand, I., Huyghe, P., Mugnier, J-L., & Ojha, T. (2014). What controls the growth of the Himalayan foreland fold-and-thrust belt? Geology, 42 (3), 247–250. https://doi.org/10.1130/G35057.1

Hodges, K.V. (2000). Tectonics of the Himalaya and southern Tibet from two perspectives. Geological Society of America Bulletin, 112, 324–350.

Hodges, K.V., & Silverberg, D.S. (1988). Thermal evolution of the Greater Himalaya, Garhwal, India. Tectonics, 7, 583-600.

Hodges, K.V., Burchfiel, B.C., Royden, L.H., Chen, Z., & Liu, Y. (1993). The metamorphic signature of contemporaneous extension and shortening in the central Himalayan orogen: data from the Nyalam transect, southern Tibet. Journal of Metamorphic Geology, 11, 721-737.

Hodges, K.V., Hames, W.E., Olszewski, W.J., Burchfiel, B.C., Royden, L.H., & Chen, Z. (1994). Thermobarometric and $^{40}Ar/^{39}Ar$ geochronologic constraints on Eohimalayan metamorphism in the Dinggy area, southern Tibet. Contributions to Mineralogy Petrology, 117, 151– 163.

Hodges, K.V., Le Fort, P., & Pêcher, A. (1988). Possible thermal buffering by crustal anatexis in collisional orogens: thermobarometric evidence from the Nepalese Himalaya. Geology, 16, 707-710.

Hodges, K.V., Parrish, R.R., & Searle, M.P. (1996). Tectonic evolution of the central Annapurna Range, Nepalese Himalayas. Tectonics, 15, 1264-1291.

Hoisch, T.D. (1990). Empirical calibration of six geobarometers for the mineral assemblage quartz + muscovite + biotite + plagioclase + garnet. Contributions to Mineralogy and Petrology, 104, 225-234.

Holland, T. J. B., Baker, J. M., & Powell, R. (1998). Mixing properties and activity—Composition relationships of chlorites in the system MgO-FeO-Al2O3-SiO2-H2O. European Journal of Mineralogy, 10(3), 395–406. https://doi.org/10.1127/ejm/10/3/0395

Hopkinson, T.N., Harris, N.B.W., Warren, C.J., Spencer, C.J., Roberts, N.M.W., Horstwood, M.S.A., Parrish, R.R., & EIMF (2017). The identification and significance of pure sediment-derived granites. Earth and Planetary Science Letters, 467, 57-63. https://doi.org/10.1016/j.epsl.2017.03.018

Hu, X., Garzanti, E., Wang, J., Huang, W., An, Q. & Webb, A. 2016. The timing of India–Asia collision onset – Facts, theories, controversies. Earth-Science Reviews, 160, 264–299.

Hu, X., Jansa, L., Chen, L., Griffin, W.L., O'Reilly, S.Y. & Wang, J. (2010). Provenance of Lower Cretaceous Wölong volcaniclastics in the Tibetan Tethyan Himalaya: Implications for the final breakup of Eastern Gondwana. Sedimentary Geology, 223, 193–205. https://doi.org/10.1016/j.sedgeo.2009.11.008

Hubbard, M.S. (1989). Thermobarometric constraints on the thermal history of the Main Central Thrust Zone and Tibet Slab, eastern Nepal Himalaya. Journal of Metamorphic Geology, 7, 19-30.

Hubbard, M.S. (1996). Ductile shear as a cause of inverted metamorphism: example from the Nepal Himalaya. Journal of Geology, 104, 493-499.

Hughes, 2016). Harrison, T.M., Grove M., & Lovera O.M. (1997). New insights into the origin of two contrasting Himalayan granite belts. Geology, 25, 899-902.

Hughes, N.C., Myrow, P.M., Peng, S., Banerjee, D.M. (2018). The Parahio Formation of the Tethyan Himalaya: The type section, thickness, lithostratigraphy and biostratigraphy of the best characterised Cambrian succession in the Indian subcontinent. Journal of the Palaeontological Society of India, 63(1), 1-18.

Hughes, N.C., Peng, S., Bhargava, O.N., Ahulwalia, A.D., Walia, S., Myrow, P.M., & Parcha, S.K. (2005). The Cambrian biostratigraphy of the Tal Group, Lesser Himalaya, India, and early Tsanglangpuan (late early Cambrian) trilobites from the Nigali Dhar Syncline. Geological Magazine, 142, 57–80.

Iaccarino, S., Montomoli, C., Carosi, R., Massonne, H.-J., & Visonà, D. (2017). Geology and tectono-metamorphic evolution of the Himalayan metamorphic core: Insights from the Mugu Karnali transect, western Nepal (central Himalaya). Journal of Metamorphic Geology, 35(3), 301–325. https://doi.org/10.1111/jmg.12233

Iaccarino, S., Montomoli, C., Montemagni, C., Massonne, H-J., Langone, A., Jain, A.K., Visonà, D., & Carosi, R. (2020). The Main Central Thrust zone along the Alaknanda and Dhauli Ganga valleys (Garhwal Himalaya, NW India): Insights into an inverted metamorphic sequence. Lithos, 372–373. https://doi.org/10.1016/j.lithos.2020.105669

Imayama, T., Takeshita, T., & Arita, K. (2010). Metamorphic P-T profile and P-T path discontinuity across the far-eastern Nepal Himalaya: Investigation of channel flow

models. Journal of Metamorphic Geology, 28, 527-549. https://doi.org/10.1111/j.1525-1314.2010.00879.x

Inger, S. & Harris, N.B.W. (1992). Tectonothermal evolution of the High Himalaya Crystalline sequence, Langtang Valley, northern Nepal. Journal of Metamorphic Geology, 10, 439-452

Jadoul, F., Berra, F., & Garzanti, E. (1998). The Tethys Himalayan passive margin from Late Triassic to Early Cretaceous (South Tibet): Journal of Asian Earth Sciences, 16, 173–194. https://doi.org/10.1016/S0743-9547(98)00013-0

Jain, A.K., & Chander, R. (1995). Geodynamic models for Uttarkashi earthquake of October 20, 1991. Memoirs of the Geological Society of India, Bangalore, 225-233.

Jamieson, R.A., & Beaumont, C. (2013). On the origin of orogens. Geological Society of America Bulletin, 11-12, 1671-1702.

Jamieson, R.A., Beaumont, C., Hamilton, J., & Fullsack, P. (1996). Tectonic assembly of inverted metamorphic sequences. Geology, 24, 839–842.

Jamieson, R.A., Beaumont, C., Medvedev, S., Nguyen, M.H. (2004). Crustal channel flows: 2. Numerical models with implications for metamorphism in the Himalayan–Tibetan orogen. Journal of Geophysical Research, 109. https://doi.org/10.1029/2003JB002811

Jamieson, R.A., Beaumont, C., Nguyen, M.H., & Grujic, D. (2006). Provenance of the Greater Himalayan Sequence and associated rocks: predictions of channel flow models. Geological Society, London, Special Publications, 268, 165-182, 1 January 2006. https://doi.org/10.1144/GSL.SP.2006.268.01.07

Jharendra, K.C., & Paudyal, K.R. (2019). Characteristics and field relation of Ulleri Augen Gneiss to country rocks in the Lesser Himalaya: A case study from Syaprubesi-Chhyamthali area, central Nepal. Journal of Nepal Geological Society, 58, 89-96. https://doi.org/10.3126/jngs.v58i0.24577

Kaneko, Y. (1995). Thermal structure in the Annapurna region, central Nepal Himalaya: implication for the inverted metamorphism. J. Mineral. Petrol. Econ. Geol., 90, 143-154.

Kaneoka, I. & Kono, M. (1981). $^{40}Ar/^{39}Ar$ dating of Himalayan rocks from the Mount Everest Region. Journal of Geophysics, 49, 207-211.

Kapp, P., DeCelles, P.G., Gehrels, G.E., Heizler, M. & Ding, L. 2007. Geological records of the Lhasa–Qiangtang and Indo-Asian collisions in the Nima area of central Tibet. Geological Society of America Bulletin, 119, 917–932.

Kapp, P., Murphy, M.A., Yin, A., Harrison, T.M., Ding, L. & Guo, J.R. 2003. Mesozoic and Cenozoic tectonic evolution of the Shiquanhe area of western Tibet. Tectonics, 22. https://doi.org/10.1029/2001TC001332

Kawakami, T., Sakai, H., & Sato, K. (2019). Syn-metamorphic B-bearing fluid infiltrations deduced from tourmaline in the Main Central Thrust zone, Eastern Nepal Himalayas. Lithos, 348–349, 105175. https://doi.org/10.1016/j.lithos.2019.105175

Kayal, J.R. (1996). Precursor seismicity, foreshocks and aftershocks of the Uttarkashi earthquake of October 20, 1991 at Garhwal Himalaya. Tectonophysics, 263, 339-345.

Kellett, S.A., Cottle, J.M., & Larson, K.P. (2018). The South Tibetan Detachment System: history, advances, definition and future directions. Geological Society, London, Special Publications, 483, 377-400. https://doi.org/10.1144/SP483.2

Kelly, E. D., Hoisch, T. D., Wells, M. L., Vervoort, J. D. & Beyene, M. A. (2015). An Early Cretaceous garnet pressure–temperature path recording synconvergent burial and

exhumation from the hinterland of the Sevier orogenic belt, Albion Mountains, Idaho. Contributions to Mineralogy and Petrology 170, 1–22.

Khan, M.A., Bera, M., Spicer, R.A., Spicer, T.E.V., & Bera, S. (2019). Palaeoclimatic estimates for a latest Miocene-Pliocene flora from the Siwalik Group of Bhutan: Evidence for the development of the South Asian Monsoon in the eastern Himalaya, Palaeogeography, Palaeoclimatology, Palaeoecology, 514, 326-335. https://doi.org/10.1016/j.palaeo.2018.10.019

Khanal, S., Robinson, D.M., Mandal, S., & Simkhada, P. (2014). Structural, geochronological and geochemical evidence for two distinct thrust sheets in the 'Main Central thrust zone', the Main Central thrust and Ramgarh–Munsiari thrust: implications for upper crustal shortening in central Nepal Geological Society, London, Special Publications, 412, 221-245. https://doi.org/10.1144/SP412.2

Khattri, K.N. and Tyagi, A.K. (1983). Seismicity patterns in the Himalayan plate boundary and identification of areas of high seismic potential. Tectonophysics, 96, 281-297.

Kidder, S.B., Herman, F., Saleeby, J., Avouac, J-P., Ducea, M.N., & Chapman, A. (2013). Shear heating not a cause of inverted metamorphism. Geology, 41, 899–902. https://doi.org/10.1130/G34289.1

Klootwijk, C.T., Gee, J.S., Peirce, J.W., Smith, G.M., & McFadden, P.L. (1992). An early India-Asia contact: Paleomagnetic constraints from Ninetyeast Ridge, ODP Leg 121. Geology, 20(5), 395–398. https://doi.org/10.1130/0091-7613(1992)020<0395:AEIACP>2.3.CO;2

Kohn, M. J., M. Wieland, C. D. Parkinson, & B. N. Upreti (2004). Miocene faulting at plate tectonic velocity in the Himalaya of central Nepal, Earth and Planetary Science Letters, 228, 299–310.

Kohn, M. J., S. K. Paul, & S. L. Corrie (2010). The lower Lesser Himalayan sequence: A Paleoproterozoic arc on the northern margin of theIndian plate, Geological Society of America Bulletin, 122, 323–335.

Kohn, M.J. (1993). Uncertainties in differential thermodynamic (Gibbs' method) P-T paths. Contributions to Mineralogy and Petrology, 113, 24–39. https://doi.org/10.1007/BF00320829

Kohn, M.J. (2008). P-T-t data from central Nepal support critical taper and repudiate large-scale channel flow of the Greater Himalayan Sequence. Geological Society of America Bulletin, 120, 259-273. https://doi.org/10.1130/B26252.1

Kohn, M.J. (2014). Himalayan metamorphism and its tectonic implications. Annual Review of Earth and Planetary Sciences, 42(1), 381-419.

Kohn, M.J. (2016). Metamorphic chronology—a tool for all ages: Past achievements and future prospects. American Mineralogist, 101, 25–42. https://doi.org/10.2138/am-2016-5146

Kohn, M.J., & Spear, F. (2000). Retrograde net transfer reaction insurance for pressure-temperature estimates. Geology, 28, 1127–1130. https://doi.org/10.1130/0091-7613(2000)28<1127:RNTRIF>2.0.CO;2

Kohn, M.J., & Spear, F.S. (1990). Two new barometers for garnet amphibolites with applications to southeastern Vermont: American Mineralogist, 75, p. 89–96.

Kohn, M.J., & Spear, F.S. (1991). Error propagation for barometers: 2. Application to rocks. American Mineralogist, 76 (1-2), 138–147.

Kohn, M.J., Catlos, E.J., Ryerson, F.J., & Harrison, T.M. (2001). Pressure-temperature-time path discontinuity in the Main Central thrust zone, central Nepal. Geology, 29 (7), 571–574. https://doi.org/10.1130/0091-7613(2001)029<0571:PTTPDI>2.0.CO;2

1788 Kohn, M.J., Catlos, E.J., Ryerson, F.J., & Harrison, T.M. (2001). Pressure–temperature–time
1789 path discontinuity in the Main Central thrust zone, central Nepal. Geology, 29, 571–574.
1790 Lanari, P. & Duesterhoeft, E. (2019). Modeling metamorphic rocks using equilibrium
1791 thermodynamics and internally consistent databases: Past achievements, problems and
1792 perspectives. Journal of Petrology, 60, 19–56. https://doi.org/10.1093/petrology/egy105
1793 Lanari, P., & Engi, M. (2017). Local bulk composition effects on metamorphic mineral
1794 assemblages. Reviews in Mineralogy and Geochemistry, 83, 55– 102.
1795 https://doi.org/10.2138/rmg.2017.83.3
1796 Larson, K.P., Godin, L., & Price, R.A. (2010). Relationships between displacement and
1797 distortion in orogens: Linking the Himalayan foreland and hinterland in central Nepal.
1798 Geological Society of America Bulletin, 122 (7-8), 1116–1134.
1799 https://doi.org/10.1130/B30073.1
1800 Larson K.P., Kellet, D.A., Cottle, J.M., Camacho, A., & Brubacher, A.D. (2019). Mid-Miocene
1801 initiation of E-W extension and recoupling of the Himalayan Orogen. Terra Nova 12443,
1802 1–8.
1803 Larson, K., Gervais, F., & Kellett, D. A. (2013). A P-T-t-D discontinuity in east-central Nepal:
1804 Implications for the evolution of the Himalayan mid-crust. Lithos, 179, 275-292.
1805 https://doi.org/10.1016/j.lithos.2013.08.012
1806 Larson, K.P., Ambrose, T.K., Webb, A.A.G., Cottle, J.M., & Shrestha, S. (2015). Reconciling
1807 Himalayan midcrustal discontinuities: The Main Central thrust system. Earth and
1808 Planetary Science Letters, 429, 139-146. https://doi.org/10.1016/j.epsl.2015.07.070
1809 Laskowski, A.K., Kapp, P., Vervoort, J.D., & Ding, L. (2016). High-pressure Tethyan Himalaya
1810 rocks along the India-Asia suture zone in southern Tibet. Lithosphere, 8 (5), 574–582.
1811 https://doi.org/10.1130/L544.1
1812 Lawver, L.A., Norton, I.O., Dalziel, I.W.D., Davis, J.K. & Gahagan, L.M. (2018). The PLATES
1813 2017 Atlas of Plate Reconstructions (550 Ma to Present Day). PLATES Progress Report,
1814 390-0318.
1815 Le Fort, P. (1975). Himalaya, the collided range, Present knowledge of the continental arc.
1816 American Journal of Science, 275A, 1-44.
1817 Le Fort, P. (1996). Evolution of the Himalaya. In Yin, A., and Harrison, T.M., (Eds.), The
1818 Tectonic Evolution of Asia. Cambridge University Press, pp. 95-109.
1819 Lee, J., Hacker, B., & Wang, Y. (2004). Evolution of North Himalayan gneiss domes: structural
1820 and metamorphic studies in Mabja Dome, southern Tibet. Journal of Structural Geology,
1821 26, 2297–316.
1822 LeFort, P., & Rai, S.M. (1999). Pre-Tertiary felsic magmatism of the Nepal Himalaya: recycling
1823 of continental crust. Journal of Asian Earth Sciences, 17, 607– 628.
1824 Lihter, I., Larson, K.P., Shrestha, S., Cottle, J.M., & Brubacher, A.D. (2020). Contact
1825 metamorphism of the Tethyan Sedimentary Sequence, Upper Mustang region, west-
1826 central Nepal. Geological Magazine, 157(11), 1917–1932.
1827 https://doi.org/10.1017/S0016756820000229
1828 Liu, G., & Einsele, G. (1994). Sedimentary history of the Tethyan basin in the Tibetan
1829 Himalayas. Geologische Rundschau, 82, 32– 61.
1830 Liu, J-H., Xie, C-M., Li, C., Wang, M., Wu, H., Li, X-K., Liu, Y-M., Zhang, T-Y. (2018). Early
1831 Carboniferous adakite-like and I-type granites in central Qiangtang, northern Tibet:
1832 Implications for intra-oceanic subduction and back-arc basin formation within the Paleo-
1833 Tethys Ocean. Lithos, 296–299, 265-280. https://doi.org/10.1016/j.lithos.2017.11.005

1834 Liu, Z.C., Wu, F.Y., Ding, L., Liu, X.C., Wang, J.G., & Ji, W.Q. (2016). Highly fractionated
1835 Late Eocene (~ 35 Ma). leucogranites in the Xiaru Dome, Tethyan Himalaya, South
1836 Tibet. Lithos, 240-243, 337-354.
1837 Lombardo B., Pertusati, P., & Borghi, S. (1993). Geology and tectonomagmatic evolution of the
1838 eastern Himalaya along the Chomolungma-Makalu transect. In Trealor, P.J., & Searle,
1839 M.P., (Eds.), Himalayan Tectonics. Geological Society Special Publication, 74, pp. 341-
1840 355.
1841 Lombardo, B., Rolfo, F., 2000. Two contrasting eclogite types in the Himalayas: implications for
1842 the Himalayan orogeny. Journal of Geodynamics, 30, 37-60.
1843 Long, S., & McQuarrie, N. (2010). Placing limits on channel flow: Insights from the Bhutan
1844 Himalaya. Earth and Planetary Science Letters, 290, 475-390.
1845 Long, S., McQuarrie, N., Tobgay, T., & Grujic, D. (2011). Geometry and crustal shortening of
1846 the Himalayan fold-thrust belt, eastern and central Bhutan. Geological Society of
1847 America Bulletin, 123 (7-8), 1427–1447. https://doi.org/10.1130/B30203.1
1848 Long, S.P., Gordon, S.M., & Soignard, E., 2017, Distributed north-vergent shear and flattening
1849 through Greater and Tethyan Himalayan rocks: Insights from metamorphic and strain
1850 data from the Dang Chu region, central Bhutan. Lithosphere, 9, 774–795.
1851 https://doi.org/10.1130/L655.1
1852 Long, S.P., Mullady, C.L., Starnes, J.K., Gordon, S.M., Larson, K.P., Pianowski, L.S., Miller,
1853 R.B., & Soignard, E. (2019). A structural model for the South Tibetan detachment system
1854 in northwestern Bhutan from integration of temperature, fabric, strain, and kinematic
1855 data. Lithosphere, 11 (4), 465–487. https://doi.org/10.1130/L1049.1
1856 Macfarlane, A.M. (1995). An evaluation of the inverted metamorphic gradient at Langtang
1857 National Park, central Nepal Himalaya. Journal of Metamorphic Geology, 13, 595-612.
1858 Mahajan, A.K., Thakur, C., Sharma, M.L., & Chauhan, M. (2010). Probabilistic seismic hazard
1859 map of NW Himalaya and its adjoining area, India. Natural Hazards, 53, 443-457.
1860 https://doi.org/10.1007/s11069-009-9439-3
1861 Maiti, G., & Mandal, N. (2021) Early Miocene exhumation of high-pressure rocks in the
1862 Himalaya: A response to reduced India-Asia convergence velocity. Frontiers in Earth
1863 Science, https://doi.org/10.3389/feart.2021.632806.
1864 Maiti, G., Mandal, N., & Misra, S. (2020). Insights into the dynamics of an orogenic wedge from
1865 lubrication theory: Implications for the Himalayan tectonics. Tectonophysics, 776,
1866 228335. https://doi.org/10.1016/j.tecto.2020.228335
1867 Makovsky, Y., Klemperer, S. L., Huang, L., Lu, D., & Project INDEPTH Team (1996).
1868 Structural elements of the southern Tethyan Himalaya crust from wide-angle seismic
1869 data, Tectonics, 15(5), 997– 1005. https://doi.org/10.1029/96TC00310
1870 Makovsky, Y., Klemperer, S.L., Ratschbacher, L., & Alsdorf, D. (1999). Midcrustal reflector on
1871 INDEPTH wide-angle profiles: an ophiolitic slab beneath the India–Asia suture in
1872 southern Tibet? Tectonics, 18, 793–808.
1873 Mandal, S., Robinson, D.M., Khanal, S., & Das, O. (2015). Redefining the tectonostratigraphic
1874 and structural architecture of the Almora klippe and the Ramgarh–Munsiari thrust sheet
1875 in NW India. In: Mukherjee, S., Carosi, R., van der Beek, P.A., Mukherjee, B.K., &
1876 Robinson, D.M. (Eds.) Tectonics of the Himalaya, Geological Society of America
1877 Special Publications, 412, 247–269.
1878 Mandal, S.. Robinson, D.M., Kohn, M.J., Khanal,S., Das, O., & Bose S. (2016). Zircon U-Pb
1879 ages and Hf isotopes of the Askot klippe, Kumaun, northwest India: Implications for

Paleoproterozoic tectonics, basin evolution and associated metallogeny of the northern Indian cratonic margin, Tectonics, 35. https://doi.org/10.1002/2015TC004064

Manickavasagam, R.M., Jain, A.K., Singh, S., & Asokan, A. (1999). Metamorphic evolution of the northwest Himalaya, India: Pressure-temperature data, inverted metamorphism, and exhumation in the Kashmir, Himachal, and Garhwal Himalayas. In Macfarlane, A., Sorkhabai, R.B., and Quade, J. (Eds.), Himalaya and Tibet: Mountain roots to mountain tops. Geological Society of America Special Paper, 328, 179-198.

Martin, A. J., Ganguly, J., & DeCelles, P.G. (2010). Metamorphism of Greater and Lesser Himalayan rocks exposed in the Modi Khola valley, central Nepal. Contributions to Mineralogy and Petrology, 159, 203–223.

Martin, A.J. (2017a). A review of Himalayan stratigraphy, magmatism, and structure. Gondwana Research, 49, 42-80. https://doi.org/10.1016/j.gr.2017.04.031

Martin, A.J. (2017b). A review of definitions of the Himalayan Main Central Thrust. International Journal of Earth Sciences, 106, 2131-45. https://doi.org/10.1007/s00531-016-1419-8

Martin, A.J. Burgy, K.D., Kaufman, A.J., & Gehrels, G.E. (2011). Stratigraphic and tectonic implications of field and isotopic constraints on depositional ages of Proterozoic Lesser Himalayan rocks in central Nepal. Precambrian Research, 185, 1-17.

Martin, A.J., DeCelles, P.G., Gehrels, G.E., Patchett, P.J., & Isachsen, C. (2005). Isotopic and structural constraints on the location of the MainCentral Thrust in the Annapurna Range, central Nepal Himalaya. Geological Society of America Bulletin, 117(7-8), 926–944.

Matin, A., & Mukul, M. (2010). Phases of deformation from cross-cutting structural relationships in external thrust sheets: Insights from small-scale structures in the Ramgarh thrust sheet, Darjiling Himalaya, West Bengal. Current Science, 99(10), 1369-1377.

Matsuoka, A., Yang, Q., Kobayashi, K., Takei, M., Nagahashi, T., Zeng, Q., & Wang, Y. (2002). Jurassic–Cretaceous radiolarian biostratigraphy and sedimentary environments of the Ceno-Tethys: records from the Xialu Chert in the Yarlung-Zangbo Suture Zone, southern Tibet. Journal of Asian Earth Sciences, 20(3), 277-287. https://doi.org/10.1016/S1367-9120(01)00044-X

McKenzie, N.R., Hughes, N.C., Myrow, P.M., Xiao, S., & Sharma, M. (2011). Correlation of Precambrian–Cambrian sedimentary successions across northern India and the utility of isotopic signatures of Himalayan lithotectonic zones. Earth and Planetary Science Letters, 312(3–4), 471-483. https://doi.org/10.1016/j.epsl.2011.10.027

Medicott, H.B. (1864). On the geologic structure and relations of the southern portion of the Himalayan range between the rivers Ganges and Ravee. Memoirs of the Geological Survey of India, 3, 1-206.

Meigs, A.J., Burbank, D.W., & Beck, R.A. (1995). Middle-late Miocene [>10 Ma] formation of the Main Boundary Thrust in the Western Himalaya. Geology, 23, 423-426.

Metcalfe, I. (1999). The Tethys; How many? How old? How deep? How wide? In: Ratanasthien, B. & Rieb, S. L. (eds) Proceedings of the International Symposium on Shallow Tethys, 5, 1-15.

Metcalfe, I. (2009). Late Palaeozoic and Mesozoic tectonic and palaeogeographic evolution of SE Asia. Geological Society of London, Special Publication, 315, 7-23.

Metcalfe, I. 2013. Gondwana dispersion and Asian accretion: Tectonic and palaeogeographic evolution of eastern Tethys. Journal of Asian Earth Sciences, 66, 1-33.

Metcalfe, R.P. (1993). Pressure, temperature and time constraints on metamorphism across the Main Central Thrust zone and High Himalaya Slab in the Garhwal Himalaya. In Trealor, P.J., and Searle, M.P., (Eds.), Himalayan Tectonics. Geological Society Special Publication, 74, 485-509.

Middlemiss, C.S. (1887). Physical geology of West British Garhwal; with notes on a route traverse through Jaunsar Bawar and Tiri-Garhwal. Records of the Geological Survey of India, 20, 26-40.

Miller, C., Klotzli, U., Frank, W., Thoni, M., & Grasemann, B. (2000). Proterozoic crustal evolution in the NW Himalaya (India) as recorded by circa 1.80 Ga mafic and 1.84 Ga granitic magmatism. Precambrian Research, 103 (3–4), 191– 206.

Molnar, P., & England, P. Late Cenozoic uplift of mountain ranges and global climate change: chicken or egg?. Nature, 346, 29–34. https://doi.org/10.1038/346029a0

Molnar, P. & Stock, J.M. (2009). Slowing of India's convergence with Eurasia since 20 Ma and its implications for Tibetan mantle dynamics. Tectonics, 28. https://doi.org/10.1029/2008TC002271

Montemagni, C, Carosi, R, Fusi, N, Iaccarino, S., Montomoli, C., Villa, I.M., & Zancehtta, S. (2020) Three-dimensional vorticity and time-constrained evolution of the Main Central Thrust zone, Garhwal Himalaya (NW India). Terra Nova. 2020; 32: 215– 224. https://doi.org/10.1111/ter.12450

Montemagni, C., Montomoli, C., Iaccarino, S., Carosi, R., Jain, A.K., Massonne, H-K., & Villa, I.M. (2018) Dating protracted fault activities: microstructures, microchemistry and geochronology of the Vaikrita Thrust, Main Central Thrust zone, Garhwal Himalaya, NW India. Geological Society, London, Special Publications, 481, 127-146, https://doi.org/10.1144/SP481.3

Montomoli, C., Carosi, R., & Iaccarino, S. (2015). Tectonometamorphic discontinuities in the Greater Himalayan Sequence: a local or a regional feature? Geological Society Special Publication, 412, 25-41.

Montomoli, C., Carosi, R., Rubatto, D., Visonà, D., & S. Iaccarino (2017). Tectonic activity along the inner margin of the South Tibetan Detachment constrained by syntectonic leucogranite emplacement in Western Bhutan. Italian Journal of Geosciences, 136(1), 5–14. https://doi.org/10.3301/IJG.2015.26

Montomoli, C., Iaccarino, S., Carosi, R., Langone, A., & Visonà, D. (2013). Tectonometamorphic discontinuities within the Greater Himalayan Sequence in Western Nepal (Central Himalaya): insights on the exhumation of crystalline rocks. Tectonophysics, 608, 1349-1370.

Mosca, P., Groppo, C., & Rolfo, F. (2012). Structural and metamorphic features of the Main Central Thrust Zone and its contiguous domains in the eastern Nepalese Himalaya, in Zucali, M., Spalla, M.I., & Gosso, G., eds., Multiscale structures and tectonic trajectories in active margins. Journal of the Virtual Explorer, 41, 1-34, Clayton, Victoria, Australia: Australian Crustal Research Centre, Monash University. https://doi.org/10.3809/jvirtex.2011.00294

Mottram, C.M., Warren, C.J., Regis, D., Roberts, N.M.W., Harris, N.B.W. Argles, T.W., & Parrish, R.R. (2014). Developing an inverted Barrovian sequence; insights from monazite petrochronology. Earth and Planetary Science Letters, 403, 418-431. https://doi.org/10.1016/j.epsl.2014.07.006

1971 Moynihan, D., & Pattison, D.R.M. (2013). An automated method for the calculation of P-T paths
1972 from garnet zoning, with application to metapelitic schist from the Kootenay Arc, British
1973 Columbia, Canada. Journal of Metamorphic Geology, 31, 525-548.
1974 https://doi.org/10.1111/jmg.12032
1975 Mugnier, J.L., Huyghe, P., Chalaron, E., & Mascle, G. (1994). Recent movements along the
1976 Main Boundary Thrust of the Himalayas: Normal faulting in an over-critical thrust
1977 wedge? Tectonophysics, 238(1–4), 199-215. https://doi.org/10.1016/0040-
1978 1951(94)90056-6
1979 Mugnier, J.L., Leturmy, P., Mascle, G., Huyghe, P., Chalaron, E., Vidal, G., Husson, L., &
1980 Delcaillau, B. (1999). The Siwaliks of western Nepal: I. Geometry and kinematics.
1981 Journal of Asian Earth Sciences, 17(5-6), 629-642. https://doi.org/10.1016/S1367-
1982 9120(99)00038-3
1983 Mukherjee, S. (2013). Higher Himalaya in the Bhagirathi section (NW Himalaya, India): its
1984 structures, backthrusts and extrusion mechanism by both channel flow and critical taper
1985 mechanisms. International Journal of Earth Sciences (Geol Rundsch) 102, 1851–1870.
1986 https://doi.org/10.1007/s00531-012-0861-5
1987 Mukherjee, S., Koyi, H.A. & Talbot, C.J. (2012). Implications of channel flow analogue models
1988 for extrusion of the Higher Himalayan Shear Zone with special reference to the out-of-
1989 sequence thrusting. International Journal of Earth Sciences (Geol Rundsch) 101, 253–
1990 272. https://doi.org/10.1007/s00531-011-0650-6
1991 Mukhopadhyay, D. K., Chakraborty, S., Trepmann, C., Rubatto, D., Anczkiewicz, R., Gaidies,
1992 F., et al. (2017). The nature and evolution of the Main Central Thrust: Structural and
1993 geochronological constraints from the Sikkim Himalaya, NE India. Lithos, 282–283,
1994 447–463. https://doi.org/10.1016/j.lithos.2017.01.015
1995 Mukul, M. (2000). The geometry and kinematics of the Main Boundary Thrust and related
1996 neotectonics in the Darjiling Himalayan Fold-and-Thrust belt, West Bengal, India.
1997 Journal of Structural Geology, 22, 1261–1283.
1998 Mukul, M., Jaiswal, M., & Singhvi, A.K. (2007). Timing of recent out-of-sequence active
1999 deformation in the frontal Himalayan wedge: Insights from the Darjiling sub-Himalaya,
2000 India. Geology, 35 (11), 999–1002. https://doi.org/ https://doi.org/10.1130/G23869A.1
2001 Myrow, P.M., Hughes, N.C., Derry, L.A., McKenzie, N.R., Jiang, G., Webb, A.A.G., Banerjee,
2002 D.M., Paulsen, T.S., & Singh, B.P. (2015). Neogene marine isotopic evolution and the
2003 erosion of Lesser Himalayan strata: implications for Cenozoic tectonic history. Earth
2004 Planetary Science Letters, 417, 142–150.
2005 Myrow, P.M., Hughes, N.C., Paulsen, T.S., Williams, I.S., Parcha, S.K., Thompson, K.R.,
2006 Bowring, S.A., Peng, S.C., & Ahluwalia, A.D. (2003). Integrated tectonostratigraphic
2007 analysis of the Himalaya and implications for its tectonic reconstruction. Earth and
2008 Planetary Science Letters, 212, 433-441.
2009 Myrow, P.M., Hughes, N.C., Searle, M.P., Fanning, C.M., Peng, S., & Parcha, S.K. (2009).
2010 Stratigraphic correlation of Cambrian-Ordovician deposits along the Himalaya:
2011 implications for the age and nature of rocks in the Mt. Everest region. Geological Society
2012 of America Bulletin, 120, 323–332.
2013 Myrow, P.M., Snell, K., Hughes, N.C., Paulsen, T.S., Heim, N.A., & Parcha, S.K. (2006).
2014 Cambrian depositional history of the Zanskar Valley region of Indian Himalaya: Tectonic
2015 implications: Journal of Sedimentary Research, 76, 364-381.

2016 Nábělek, J., Hetenyi, G., Vergne, J., Sapkota, S., Kafle, B., Jiang, M., Su, H., Chen, J., Huang,
2017 B.S., & Hi, C.T. (2009). Underplating in the Himalaya-Tibet collision zone revealed by
2018 the Hi-CLIMB experiment. Science, 325, 1371-1374.
2019 https://doi.org/10.1126/science.1167719
2020 Najman, Y., Garzanti, E., Pringle, M., Bickle, M., Stix, J., & Khan, I. (2003). Early–middle
2021 Miocene paleodrainage and tectonics in the Pakistan Himalaya. Geological Society of
2022 America Bulletin, 115, 1265–1277.
2023 Najman, Y., Jenks, D. et al. (2017). The Tethyan Himalayan detrital record shows that India–
2024 Asia terminal collision occurred by 54 Ma in the Western Himalaya. Earth and Planetary
2025 Science Letters, 459, 301–310.
2026 Najman, Y., Pringle, M., Godin, L., & Oliver, G. (2001). Dating of the oldest continental
2027 sediments from the Himalayan foreland basin. Nature, 410, 194– 197.
2028 Najman, Y., Pringle, M., Godin, L., & Oliver, G. (2002). A reinterpretation of the Balakot
2029 formation: implications for the tectonics of the NW Himalaya, Pakistan. Tectonics, 21
2030 (Art. No. 1045).
2031 Nelson, K.D., Zhao, W., Brown, L.D., & others (1996). Partially molten crust beneath Southern
2032 Tibet: synthesis of project INDEPTH results. Science, 274, 1684-1688.
2033 Ni, J. & Barazangi, M. (1984). Seismotectonics of the Himalayan collision zone; geometry of the
2034 underthrusting Indian Plate beneath the Himalaya. Journal of Geophyscial Research, 89,
2035 1147-1163.
2036 Oldham, R.D. (1883). The geology of Jaunsar and the Lower Himalayas. Records of the
2037 Geological Survey of India, 16, 193-198.
2038 Pandey, M.R., Lavé, J., & Massot, J.P. (1995). Interseismic strain accumulation on the
2039 Himalayan Crustal Ramp (Nepal). Geophysical Research Letters, 22, 751-754.
2040 Parrish, R.R., & Hodges, K.V. (1996). Isotopic constraints on the age and provenance of the
2041 Lesser and Greater Himalaya sequences, Nepalese Himalaya. Geological Society of
2042 America Bulletin, 108, 904-911.
2043 Parsons, A. J., Law, R. D., Lloyd, G. E., Phillips, R. J., & Searle, M. P. (2016). Thermo-
2044 kinematic evolution of the Annapurna-Dhaulagiri Himalaya, central Nepal: The
2045 Composite Orogenic System. Geochemistry, Geophysics, Geosystems, 17, 1511–1539.
2046 https://doi.org/10.1002/2015GC006184
2047 Patel, R.C., Singh, S., Asokan, A., Manickavasagam, R.M., & Jain, A.K. (1993). Extensional
2048 tectonics in the Himalayan orogen, Zanskar, NW India. In Trealor, P.J., & Searle, M.P.,
2049 (Eds.), Himalayan Tectonics. Geological Society Special Publication, 74, 445-459.
2050 Patra, A., & Saha, D. (2019). Stress regime changes in the Main Boundary Thrust zone, Eastern
2051 Himalaya, decoded from fault-slip analysis. Journal of Structural Geology, 120, 29-47.
2052 https://doi.org/10.1016/j.jsg.2018.12.010
2053 Patriat, P., & Achache, J. (1984). India–Eurasia collision chronology has implications for crustal
2054 shortening and driving mechanism of plates. Nature, 311, 615– 621.
2055 Pearson, O. N., & DeCelles, P.G. (2005). Structural geology and regional tectonic significance of
2056 the Ramgarh thrust, Himalayan fold-thrust belt of Nepal, Tectonics, 24, TC4008.
2057 https://doi.org/10.1029/2003TC001617
2058 Pêcher, A. (1989). The metamorphism in the central Himalaya. Journal of Metamorphic
2059 Geology, 7, 31-41.
2060 Pêcher, A. (1991). The contact between the Higher Himalayan crystallines and the Tibetan
2061 sedimentary series: Miocene large-scale dextral shearing. Tectonics, 10, 587-598.

Pêcher, A., & Le Fort, P. (1986). The metamorphism in central Himalaya, its relations with the thrust tectonic. In P. Le Fort, M. Colchen, & C. Montenat, (Eds.), Évolution des domains orogéniques d'Asie méridionale (de la Turquie à l'Indoneasie). Science de la Terre, 47, pp. 285-309.

Phukon, P., Sen, K., Singh, P.C., Sen, A., Srivastava, H.B., & Singhal, S. (2019). Characterizing anatexis in the Greater Himalayan Sequence (Kumaun, NW India) in terms of pressure, temperature, time and deformation, Lithos, 344–345, 22-50. https://doi.org/10.1016/j.lithos.2019.04.018

Pilgrim, G.E. & West, W.D. (1928). The structure and correlation of the Simla Rocks. Memoirs of the Geological Survey of India, 53, 1-138.

Pognante, U., & Benna, P. (1993). Metamorphic zonation, migmitization and leucogranites along the Everest transect of Eastern Nepal and Tibet: Record of an exhumation history. In Trealor, P.J., and Searle, M.P., (Eds.), Himalayan Tectonics. Geological Society Special Publication, 74, pp. 323-340.

Powers, P.M., Lillie, R.J., & Yeats, R.S. (1998). Structure and shortening of the Kangra and Dehra Dun reentrants, Sub-Himalaya, India. Geological Society of America Bulletin, 110, 1010-1027.

Quade, J., Cater, J.M.L., Ohja, T.P., Adam, J., & Harrison, T.M. (1995). Late Miocene environmental change in Nepal and the northern Indian subcontinent: stable isotopic evidence from paleosols. Geological Society of America Bulletin, 107, 1381-1397

Quade, J., Cerling, T. & Bowman, J. (1989). Development of Asian monsoon revealed by marked ecological shift during the latest Miocene in northern Pakistan. Nature 342, 163–166. https://doi.org/10.1038/342163a0

Quidelleur, X., Grove, M., Lovera, O.M., Harrison, T. M., Yin, A., & Ryerson F.J. (1997). The thermal evolution and slip history of the Renbu Zedong Thrust, southeastern Tibet. Journal of Geophysical Research, 102, 2659-2679.

Raiverman, V., Kunte, S. V., & Mukherjea, A. (1983). Basin geometry, Cenozoic sedimentation, and hydrocarbon prospects in northwestern Himalaya and Indo-Gangetic plains. Petroleum Asia Journal, 6, 67–92.

Rajendran, K., Parameswaran, R.M., & Rajendran, C. (2017). Seismotectonic perspectives on the Himalayan arc and contiguous areas: Inferences from past and recent earthquakes. Earth-Science Reviews, 173, 1-30. https://doi.org/10.1016/j.earscire2017.08.003

Rapa, G., Mosca, P., Groppo, C., & Rolfo, F. (2018). Detection of tectonometamorphic discontinuities within the Himalayan orogen: Structural and petrological constraints from the Rasuwa district, central Nepal Himalaya. Journal of Asian Earth Sciences, 158, 266-286. https://doi.org/10.1016/j.jseaes.2018.02.021

Ray, S. (1947). Zonal metamorphism in the eastern Himalayas and some aspects of local geology. The Quarterly journal of the Geological, Mining, and Metallurgical Society of India, 19, 117-140.

Reuber, I. (1986). Two peridotite units superposed by intra-oceanic thrusting in the Spongtang Klippe (Ladakh-Himalaya). Sciences Geologiques [Bulletin], 39, 391-402.

Roberts, A. G., Weinberg, R. F., Hunter, N. J. R., & Ganade, C. E. (2020). Large-scale rotational motion within the Main Central Thrust Zone in the Darjeeling-Sikkim Himalaya, India. Tectonics, 39, e2019TC005949. https://doi.org/10.1029/2019TC005949

Robinson, D.M., DeCelles, P.G., & Copeland, P. (2006). Tectonic evolution of the Himalayan thrust belt in western Nepal: Implications for channel flow models, Geological Society of America Bulletin, 118, 865–885. https://doi.org/10.1130/B25911.1

Robinson, D.M., DeCelles, P.G., Garzione, C.N., Pearson, O.N., Harrison, T.M., Catlos, E.J. (2003). Kinematic model for the Main Central Thrust in Nepal. Geology 31, 359– 362.

Robinson, D.M., DeCelles, P.G., Patchett, P.J., & Garzione, C.N. (2001). The kinematic evolution of the Nepalese Himalaya interpreted from Nd isotopes. Earth and Planetary Science Letters 192, 507– 521.

Robyr, M., & Lanari, P. (2020). Kinematic, metamorphic, and age constraints on the Miyar Thrust Zone: Implications for the Eohimalayan history of the High Himalayan Crystalline of NW India. Tectonics, 39, e2020TC006379. https://doi.org/10.1029/2020TC006379

Rolfo, F., Groppo, C. & Mosca, P. (2014). Petrological constraints of the 'Channel Flow' model in eastern Nepal. In: Mukherjee, S., Carosi, R., van der Beek, P. A., Mukherjee, B. K. & Robinson, D. M. (eds) Tectonics of the Himalaya. Geological Society, London, Special Publications, 412. https://doi.org/10.1144/SP412.4

Rolland, Y., Picard, C., Pecher, A., Lapierre, H., Bosch, D., & Keller, F. (2002). The cretaceous Ladakh arc of NW himalaya—slab melting and melt–mantle interaction during fast northward drift of Indian Plate. Chemical Geology, 182(2–4), 139-178. https://doi.org/10.1016/S0009-2541(01)00286-8

Rowley, D.B. (1996). Age of collision between India and Asia: A review of the stratigraphic data. Earth and Planetary Science Letters, 145, 1-13.

Sachan, H.K., Kohn, M.J., Saxena, A., & Corrie, S.L. (2010). The Malari leucogranite, Garhwal Himalaya, northern India: Chemistry, age, and tectonic implications. Geological Society of America Bulletin, 122, 1865-1876. https://doi.org/10.1130/B30153.1

Sakai, H., Iwano, H., Danhara, T., Takigami, Y., Rai, S.M., Upreti, B.N. & Hirata, T. (2013). Rift-related origin of Kuncha Formation. Island Arc, 22, 338-360. https://doi.org/10.1111/iar.12021

Sanyal, P., & Sinha, R. (2010). Evolution of the Indian summer monsoon: synthesis of continental records. Geological Society, London, Special Publications, 342, 153-183. https://doi.org/10.1144/SP342.11

Saxena, M.N. (1971). The crystalline axis of the Himalaya: The Indian shield and continental drift. Tectonophysics, 12(6), 433-447. https://doi.org/10.1016/0040-1951(71)90044-8

Schelling, D. & Arita, K. (1991). Thrust tectonics, crustal shortening, and the structure of the far-eastern Nepal Himalayas. Tectonics, 10, 851-862.

Schelling, D. (1992). The tectonostratigraphy and structure of the Eastern Nepal Himalaya. Tectonics, 11, 925-943.

Schmalholz, S. M., & Podladchikov, Y. Y. (2013). Tectonic overpressure in weak crustal-scale shear zones and implications for the exhumation of high-pressure rocks. Geophysical Research Letters, 40, 1984–1988. https://doi.org/10.1002/grl.50417

Schneider, C., & Masch, L. (1993). The metamorphism of the Tibet Series from the Manang area, Marsyandi Valley, central Nepal. In Trealor, P.J., Searle, M.P., (Eds.), Himalayan Tectonics. Geological Society Special Publication, 74, pp. 357-374.

Scotese, C.R., Gahagan, L.M. & Larson, R.L. (1988). Plate tectonic reconstructions of the Cretaceous and Cenozoic ocean basins. Tectonophysics, 155, 27-48.

Searle, M.P. (1999). Extensional and compressional faults in the Everest-Lhotse massif, Khumbu Himalaya, Nepal. Journal of the Geological Society London, 156, 227-240.

2152 Searle, M., Avouac, J.-, Elliott, J., & Dyck, B. (2017). Ductile shearing to brittle thrusting along
2153 the Nepal Himalaya: Linking Miocene channel flow and critical wedge tectonics to April
2154 25 2015 Gorkha earthquake. Tectonophysics, 714-715, 117-124.
2155 https://doi.org/10.1016/j.tecto.2016.08.003
2156 Searle, M. P., Law, R.D., Godin, L., Larson, L.P., Streule, M.J., Cottle, J.M., & Jessup, M.J.
2157 (2008). Defining the Himalayan Main Central Thrust in Nepal. Journal of the Geological
2158 Society, 165(2), 523–534.
2159 Searle, M.P., Law, R.D., & Jessup, M.J. (2006). Crustal structure, restoration and evolution of
2160 the Greater Himalaya in Nepal-South Tibet: implications for channel flow and ductile
2161 extrusion of the middle crust. Geological Society, London, Special Publications, 268,
2162 355-378. https://doi.org/10.1144/GSL.SP.2006.268.01.17
2163 Searle, M.P., Metcalfe, R.P., Rex, A.J., & Norry, M.J. (1993). Field relations, petrogenesis and
2164 emplacement of the Bhagirathi leucogranite, Garhwal Himalayas. In Trealor, P.J., &
2165 Searle, M.P., (Eds.), Himalayan Tectonics. Geological Society Special Publication, 74,
2166 pp. 429-444.
2167 Searle, M.P. & Rex, A.J. (1989). Thermal model for the Zanskar Himalaya. Journal of
2168 Metamorphic Geology, 7, 127-134.
2169 Şengör, A.M.C. & Atayman, S. (2009). The Permian extinction and the Tethys; an exercise in
2170 global geology. Special Paper - Geological Society of America, 448.
2171 https://doi.org/10.1130/2009.2448
2172 Siddiqui, R.H., Jan, M.Q. & Khan, M.A. (2012). Petrogenesis of Late Cretaceous lava flows
2173 from a Ceno-Tethyan Island Arc: the Raskoh Arc, Balochistan, Pakistan. Journal of
2174 Asian Earth Sciences, 59, 24-28.
2175 Siddiqui, R.H., Jan, M.Q., Khan, M.A., Kakar, M.I. & Foden, J.D. (2017). Petrogenesis of the
2176 Late Cretaceous Tholeiitic volcanism and ocean island arc affinity of the Chagai arc,
2177 western Pakistan. Acta Geologica Sinica, 91, 1248-1263.
2178 Simpson, R.L., Parrish, R.R., Searle, M.P., & Waters, D.J. (2000). Two episodes of monazite
2179 crystallization during metamorphism and crustal melting in the Everest region of the
2180 Nepalese Himalaya. Geology, 28, 403-406.
2181 Sinha-Roy, S. (1982). Interactions of Tethyan blocks and the evolution of Asian fold belts.
2182 Tectonophysics, 82, 271-297.
2183 Spear, F. S. (1993). Metamorphic Phase Equilibria and Pressure–Temperature–Time Paths.
2184 Washington, DC: Mineralogical Society of America.
2185 Spear, F. S., & Daniel, C. G. (1998). Three-dimensional imaging of garnet porphyroblast sizes
2186 and chemical zoning: Nucleation and growth history in the garnet zone. Geological
2187 Materials Research, 1, 44.
2188 Spear, F. S., & Peacock, S. M. (1989). Metamorphic pressure-temperature-time paths. American
2189 Geophysical Union Short Course in Geology, 7, 102.
2190 Spear, F.S. & Rumble, D., III (1986). Pressure, temperature and structural evolution of the
2191 Orfordville Belt, west-central New Hampshire. Journal of Petrology, 27, 1071-1093.
2192 Spear, F.S. (1986). P-T PATH:A FORTRAN program to calculate pressure-temperature paths
2193 from zoned metamorphic garnets. Computers in Geoscience, 12, 247-266.
2194 Spear, F.S., & Selverstone, J. (1983). Quantitative P-T paths from zoned minerals: Theory and
2195 tectonic applications. Contributions to Mineralogy and Petrology, 83, 348–357.

Spear, F.S., Kohn, M.J., & Paetzold, S. (1995). Petrology of the regional sillimanite zone, west-central New Hampshire, USA, with implications for the development of inverted isograds. American Mineralogist, 80, 361-376.

Spear, F.S., Selverstone, J., Hickmott, D., Crowley, P. and Hodges, K.V. (1984). P-T paths from garnet zoning: A new technique for deciphering tectonic processes in crystalline terranes. Geology, 12, 87-90.

Srivastava, V., Mukul, M., Barnes, J.B., & Mukul, M. (2018). Geometry and kinematics of Main Frontal thrust-related fault propagation folding in the Mohand Range, northwest Himalaya. Journal of Structural Geology, 115, 1-18. https://doi.org/10.1016/j.jsg.2018.06.022

Stäubli, A. (1989). Polyphase metamorphism and the development of the Main Central thrust: Journal of Metamorphic Geology, 7, 73–93.

Stephenson, B. J., Waters, D. J., & Searle, M. P. (2000). Inverted metamorphism and the Main Central Thrust: Field relations and thermobarometric constraints from the Kishtwar Window, NW Indian Himalaya. Journal of Metamorphic Geology, 18(5), 571–590. https://doi.org/10.1046/j.1525-1314.2000.00277.x

Stickroth, S. F., Carrapa, B., DeCelles, P. G., Gehrels, G. E., & Thomson, S. N. (2019). Tracking the growth of the Himalayan fold-and-thrust belt from lower Miocene foreland basin strata: Dumri Formation, western Nepal. Tectonics, 38, 3765– 3793. https://doi.org/10.1029/2018TC005390

Stöcklin, J. (1980). Geology of Nepal and its regional frame. Journal of the Geological Society, 137, 1-34.

Subedi, S., Hetényi, G., Vergne, J., Bollinger, L., Lyon-Caen, H., Farra, V., Adhikari, L.B., & Gupta, R.M. (2018). Imaging the Moho and the Main Himalayan Thrust in Western Nepal with receiver functions. Geophysical Research Letters, 45, 13,222– 13,230. https://doi.org/10.1029/2018GL080911

Thakur, C., & Kumar, S. (1994). Seismotectonics of the October 20 1991 Uttarkashi earthquake in Garhwal, Himalaya, North India. Terra Nova, 6, 90-94. https://doi.org/10.1111/j.1365-3121.1994.tb00637.x

Thakur, S.S., Patel, S.C., & Singh, A.K., (2015). A P–T pseudosection modelling approach to understand metamorphic evolution of the Main Central Thrust Zone in the Alaknanda valley, NW Himalaya. Contributions to Mineralogy and Petrology, 170:2. https://doi.org/10.1007/s00410-015-1159-y

Thakur, V.C., Jayangondaperumal, R., & Malik, M.A. (2010). Redefining Medlicott–Wadia's main boundary fault from Jhelum to Yamuna: An active fault strand of the main boundary thrust in northwest Himalaya, Tectonophysics, 489(1–4), 29-42. https://doi.org/10.1016/j.tecto.2010.03.014

Tobgay, T., McQuarrie, N., Long, S., Kohn, M.J., & Corrie, S.L. (2012). The age and rate of displacement along the Main Central Thrust in the western Bhutan Himalaya. Earth and Planetary Science Letters, 319–320, 146-158. https://doi.org/10.1016/j.epsl.2011.12.005

Tripathi, C., & Singh, G. (1987). Gondwana and associated rocks of the Himalaya and their significance. In: McKenzie, G.D., (Ed.), Gondwana Six; Stratigraphy, sedimentology, & paleontology. AGU Geophysical Monograph, 41, pp. 195-205.

Trivedi, J.R., Gopalan, K., & Valdiya, K.S. (1984). Rb-Sr ages of granitic rocks within the Lesser Himalaya nappes, Kumaun, India. Journal of the Geological Society India, 25, 641-654.

2242 Upreti, B.N. (1999). An overview of the stratigraphy and tectonics of the Nepal Himalaya.
2243 Journal of Asian Earth Sciences, 17, 741-753.
2244 Upreti, B.N., & Le Fort, P. (1999). Lesser Himalayan crystalline nappes of Nepal: Problems of
2245 their origin. In Macfarlane, A., Sorkhabai, R.B., & Quade, J. (Eds.), Himalaya and Tibet:
2246 Mountain roots to mountain tops. Geological Society of America Special Paper, 328, pp.
2247 225-238.
2248 Upreti, B.N., & Yoshida, M. (2005). Basement history and provenance of the Tethys sediments
2249 of the Himalaya: an appraisal based on recent geochronologic and tectonic data. Abstract.
2250 The 1st International Conference on the "Geology of Tethys, 2005",12–14 November
2251 2005, Cairo.
2252 Valdiya, K.S. (1980). Geology of the Kumaon Lesser Himalaya. Wadia Institute of Himalaya,
2253 Dehra Dun, India, 291 pp.
2254 Valdiya, K.S. (1988). Tectonics and the evolution of the central sector of the Himalaya.
2255 Philosophical Transactions of the Royal Society of London, A., 326, 151-175.
2256 Valdiya, K.S. (1992). The Main Boundary Thrust Zone of the Himalaya, India. Annales
2257 Tectonicae 6, suppl., 54-84.
2258 van Hinsbergen, D.J.J., Lippert, P. C.; Dupont-Nivet, G., McQuarrie, N., Doubrovine, P.V.,
2259 Spakman, W. & Torsvik, T.H. (2012). Greater India Basin hypothesis and two-stage
2260 Cenozoic collision between India and Asia. Proceedings of the National Academy of
2261 Sciences of the United States of America, 109, 7659-7664.
2262 Vannay, J.-C., & Grasemann, B. (1998). Inverted metamorphism in the High Himalaya of
2263 Himachal Pradesh (NW India): phase equilibria versus thermobarometry. Schweizerische
2264 Mineralogische und Petrographische Mitteilungen, 78, 107-132.
2265 Vannay, J.-C., & Steck, A. (1995). Tectonic evolution of the High Himalaya in upper Lahul (NW
2266 Himalaya, India). Tectonics, 14, 253-263.
2267 Vannay, J.-C., Grasemann, B., Rahn, M., Frank, W., Carter, A., Baudraz, V., Cosca, M. (2004).
2268 Miocene to Holocene exhumation of metamorphic crustal wedges in the NW Himalaya:
2269 Evidence for tectonic extrusion coupled to fluvial erosion. Tectonics 23, TC1014.
2270 Vannay, J-C., & Hodges, K.V. (1996). Tectonometamorphic evolution of the Himalayan
2271 metamorphic core between Annapurna and Dhaulagiri, central Nepal. Journal of
2272 Metamorphic Geology, 14, 635-656.
2273 Von Loczy, L. (1907). Beobachtungen im östlichen Himalaya (vom 8. his 28. Febr.. 1878).
2274 Foldt. Kozl.. 35(9): l-24
2275 Wakita, K. & Metcalfe, I. (2005). Ocean plate stratigraphy in East and Southeast Asia. Journal of
2276 Asian Earth Sciences, 24, 679-702.
2277 Wang, J.M., Zhang, J.J., & Wang, X.X. (2013). Structural kinematics, metamorphic P–T profiles
2278 and zircon geochronology across the Greater Himalayan Crystalline Complex in south-
2279 central Tibet: implication for a revised channel flow. J. Meta. Geol., 31, 607-628.
2280 https://doi.org/10.1111/jmg.12036
2281 Wang, J.-M., Zhang, J.-J., Liu, K., Zhang, B., Wang, X.-X., Rai, S., & Scheltens, M. (2016).
2282 Spatial and temporal evolution of tectonometamorphic discontinuities in the central
2283 Himalaya: Constraints from P-T paths and geochronology. Tectonophysics, 679, 41–60.
2284 https://doi.org/10.1016/j.tecto.2016.04.035
2285 Wang, X., Wei, S., & Wu, W. (2017). Double-ramp on the Main Himalayan Thrust revealed by
2286 broadband waveform modeling of the 2015 Gorkha earthquake sequence. Earth and
2287 Planetary Science Letters, 473, 83-93. https://doi.org/10.1016/j.epsl.2017.05.032

Waters D.J. (2019). Metamorphic constraints on the tectonic evolution of the High Himalaya in Nepal: the art of the possible, in Treloar J. and Searle M., eds., Himalayan Tectonics: A Modern Synthesis. Geological Society, London, Special Publications, 483. https://doi.org/10.1144/SP483-2018-187

Webb, A.G., Yin, A., Harrison, T.M., Célérier, J., & Burgess, W.P. (2007). The leading edge of the Greater Himalayan Crystalline complex revealed in the NW Indian Himalaya: Implications for the evolution of the Himalayan orogen. Geology, 35 (10), 955–958.https://doi.org/10.1130/G23931A.1

Webb, A.G., Schmitt, A.K., He, D., & Weigand, E.L. (2011). Structural and geochronological evidence for the leading edge of the Greater Himalayan Crystalline Complex in the central Nepal Himalaya. Earth and Planetary Science Letters, 304, 483-495. https://doi.org/10.1016/j.epsl.2011.02.024

Whipple, K.X., Shirzaei, M., Hodges, K., & Arrowsmith, J.R. (2016). Active shortening within the Himalayan orogenic wedge implied by the 2015 Gorkha earthquake. Nature Geoscience, 9, 711-716.

White, R.W., Powell, R., Holland, T.J.B., Johnson, T.E., & Green, E.C.R. (2014). New mineral activity-composition relations for thermodynamic calculations in metapelitic systems. Journal of Metamorphic Geology, 32, 261– 286.

Wiesmayr, G., & Grasemann, B. (2002). Eohimalayan fold and thrust belt: implications for the geodynamic evolution of the NW Himalaya (India). Tectonics 2, 1058.

Willems, H., Zhou, Z., Zhang, B., & Gräfe, K-U. (1996). Stratigraphy of the upper cretaceous and lower tertiary strata in the Tethyan Himalayas of Tibet (Tingri area, China). Geol Rundsch 85, 723. https://doi.org/10.1007/BF02440107

Wu, C., Nelson, K.D., Wortman, G., Samson, S., Yue, Y., Li, J., Kidd, W.S.F., & Edward, M.A. (1998). Yadong cross structure and South Tibetan Detachment in the east central Himalaya (89–90E). Tectonics 17, 28–45.

Wu, F-Y., Liu, X-C., Liu, Z-C., Wang, R-C., Xie, L., Wang, J-M., Ji, W-Q., Yang, L., Liu, C., Khanal, G.P., He, S-X. (2020). Highly fractionated Himalayan leucogranites and associated rare-metal mineralization, Lithos, 352–353, 105319. https://doi.org/10.1016/j.lithos.2019.105319

Yang, T., Ma, Y., Bian, W., Jin, J., Zhang, S., Wu, H., Li, H., Yang, Z., & Ding, J. (2015). Paleomagnetic results from the Early Cretaceous Lakang Formation lavas: Constraints on the paleolatitude of the Tethyan Himalaya and the India–Asia collision. Earth and Planetary Science Letters, 428, 120-133. https://doi.org/10.1016/j.epsl.2015.07.040

Ye, H., Zhang W., Yu Z., & Xia G. (1981). The seismicity and regional crustal movement in the Himalaya region. In Geological and ecological studies of the Qinghai-Xizang Plateau, 1, New York, 65-80.

Yeats, R.S., Nakata, T., Farah, A., Fort, M., Mirza, M.A., Pandey, M.R., & Stein, R.S. (1992). The Himalayan Frontal Fault System. Annales Tectonicae, 6 suppl., 85-98.

Yin, A. & Harrison, T.M. (2000). Geologic evolution of the Himalayan-Tibet orogen. Annual Reviews in Earth and Planetary Science, 28, 211-280.

Yin, A. (2006). Cenozoic tectonic evolution of the Himalayan orogen as constrained by along-strike variation of structural geometry, exhumation history, and foreland sedimentation. Earth-Science Reviews 76, 1 –131.

Yin, A., Harrison, T.M., Murphy, M.A., Grove, M., Nie, S., Ryerson, F.J., Feng, W.X., & Le, C.Z. (1999). Tertiary deformation history of southeastern and southwestern Tibet during the Indo-Asian collision. Geological Society of America Bulletin, 111, 1644–1664.

Yin, A., Harrison, T.M., Ryerson, F.J., Wenji, C., Kidd, W.S.F., & Copeland, P. (1994). Tertiary structural evolution of the Gangdese thrust system, southeastern Tibet. Journal of Geophysical Research, 99, 18175-18201.

Yoshida, M., & Upreti, B.N (2006). Neoproterozoic India within East Gondwana: Constraints from recent geochronologic data from Himalaya. Gondwana Research, 10(3-4), 349-356. https://doi.org/10.1016/j.gr.2006.04.011

Yuan, J., Yang, Z., Deng, C., Krijgsman, W., Hu, X., Li, S., Shen, Z., Qin, H., An, W., He, H., Ding, L., Guo, Z., & Zhu, R. (2020). Rapid drift of the Tethyan Himalaya terrane before two-stage India-Asia collision. National Science Review, 0, 1–13. Https://doi.org/10.1093/nsr/nwaa173

Zhang, H., Harris, N., Parrish, R., Zhang, L., & Zhao, Z. (2004). U-Pb ages of Kude and Sajia leucogranites in Sajia dome from North Himalaya and their geological implications. Chinese Science Bulletin, 49, 2087. https://doi.org/10.1360/04wd0198

Zhao, W., Nelson K.D., & Project INDEPTH (1993). Deep seismic reflection evidence for continental underthrusting beneath southern Tibet. Nature, 366, 557-559.

Zhou, Z., Kusky, T.M., & Tang, C-C. (2019). Coulomb stress change pattern and aftershock distributions associated with a blind low-angle megathrust fault, Nepalese Himalaya. Tectonophysics, 767, 228161. https://doi.org/10.1016/j.tecto.2019.228161

Zhu, B., Kidd, W.S.F., Rowley, D.B., Currie, B.S., & Shafique, N. (2005). Age of initiation of the India–Asia collision in the east-central Himalaya. Journal of Geology 113, 265–285.

Zhu, D.C., Zhao, Z.D., Niu, Y.L., Dilek, Y., Hou, Z.Q. & Mo, X.X. (2013). The origin and pre-Cenozoic evolution of the Tibetan Plateau. Gondwana Research, 23, 1429-1454.

Zyabrev, S.V., Kojima, S., & Ahmad, T. (2008). Radiolarian biostratigraphic constraints on the generation of the Nidar ophiolite and the onset of Dras arc volcanism: Tracing the evolution of the closing Tethys along the Indus – Yarlung-Tsangpo suture. Stratigraphy, 5(1), 99-112.

Table 1. Conventional P-T data from samples collected along the Darondi Khola.

Sample[a]	Gibbs Core P (±1kbar)	Gibbs Core T (±25°C)	Gibbs Rim P (± 1kbar)	Gibbs Rim T (±25°C)	Conv. Rim P (kbar, ±1σ)	Conv. Rim T (°C, ±1σ)
			Lower LHF			
DH16	-[b]	-	-	-	5.0±1.0	520±25
DH17	6.0	510	7.0	525	6.8±1.0	525±15
DH19	5.5	475	6.0	525	6.2±0.5	527±12
			Middle LHF			
DH22	6.0	498	5.0	525	5.2±1.0	520±25
DH23	7.0	525	7.3	575	7.2±2.0	540±35
DH26	6.5	500	5.5	520	5.5±1.0	524±25
DH30	-	-	-	-	8.5±2.0	570±20
DH75A	8.5	530	9.0	560	8.5±2.0	570±20
DH75B	8.0	500	8.0	560	8.5±2.0	570±20
			Upper LHF			
DH38	-	-	-	-	8.2±1.0	578±20
DH57	-	-	-	-	11.5±2.0	640±25
DH58	-	-	-	-	11.5±2.0	640±25
DH71	-	-	-	-	11.5±1.0	640±20
			GHC			
DH60	-	-	-	-	10.5±1.0	652±10
DH61	-	-	-	-	9.1±2.0	625±12
DH63	-	-	-	-	11.5±1.5	705±25
DH66	-	-	-	-	7.6±1.0	660±12
DH67	-	-	-	-	10.2±2.0	715±5

[a] See Figure 3 for samples location. Conditions estimated from Kohn et al. (2001).
[b] "-" not reported.

Table 2. P-T data generated from samples collected along the Darondi Khola using garnet isopleth thermobarometry.

Sample[a]	Isopleth Core P (±1kbar)	Isopleth Core T (±25°C)	Isopleth Rim P (±1kbar)	Isopleth Rim T (±25°C)
		Lower LHF		
DH17	4.5	540	4.5	560
DH19	4.0	520	4.8	550
		Middle LHF		
DH22	4.8	540	6.0	580
DH23	5.1	525	6.0	580
DH26	6.5	550	5.5	560
DH75A	6.8	540	6.5	580
DH75B	7.5	550	8.8	590
		Upper LHF		
DH51	-[b]	-	7.0	650
DH58	6.0	550	-	-
		GHC		
DH60	-	-	7.5	570
DH61	7.0	580	7.5	600
DH63	-	-	10.5	650
DH66			7.5	550

[a] See Figure 3 for sample locations.
[b] "-" not reported.

Table 3. Bulk rock compositions (wt%) from lower and middle LHF samples.

Analyte/Sample [a]	DH17	DH19	DH22/23	DH26	DH30	DH75A	DH75B
SiO_2	45.39	66.04	45.22	76.04	50.89	70.24	68.75
Al_2O_3	27.31	16.36	28.09	11.79	27.80	12.79	8.16
Fe_2O_3(T)	9.18	7.12	6.37	3.52	6.11	4.98	3.78
MnO	0.10	0.17	0.20	0.05	0.02	0.02	0.02
MgO	2.81	1.88	1.50	1.24	2.03	1.78	1.52
CaO	0.30	0.44	0.51	0.58	0.20	0.39	0.46
Na_2O	1.07	0.45	1.57	3.54	1.44	1.14	1.51
K_2O	7.72	5.14	7.26	1.22	6.12	2.97	1.99
TiO_2	0.86	0.52	0.86	0.40	0.79	0.49	0.35
P_2O_5	0.11	0.16	0.13	0.11	0.14	0.09	0.07
LOI	n.m.	2.15	n.m.	2.26	5.21	4.89	n.m.
Total	94.8	100.4	91.7	100.7	100.7	99.8	86.6

[a] See Figure 3 for sample locations.

2412 **Table 4.** Bulk rock compositions (wt%) from upper LHF and GHC samples.

Analyte/Sample [a]	DH51	DH58B	DH60	DH61	DH63	DH66	DH67
	LHF samples				GHC samples		
SiO_2	66.13	55.66	71.51	55.47	69.01	68.35	79.92
Al_2O_3	15.14	23.82	12.62	19.54	13.88	10.47	9.01
Fe_2O_3(T)	5.29	4.48	5.80	7.76	6.69	5.44	3.57
MnO	0.03	0.19	0.04	0.14	0.10	0.07	0.02
MgO	2.31	1.66	2.41	4.71	1.99	2.00	1.65
CaO	0.21	3.38	1.02	2.59	1.15	1.07	1.37
Na_2O	0.58	6.46	2.55	4.23	2.46	1.52	2.18
K_2O	3.78	2.08	2.68	3.84	2.32	2.53	1.22
TiO_2	0.52	0.67	0.65	0.99	0.68	0.54	0.62
P_2O_5	0.12	0.01	0.15	0.03	0.15	0.09	0.05
LOI	5.89	n.m.	n.m.	n.m.	n.m.	n.m.	1.28
Total	100	98.4	99.4	99.3	98.4	92.1	100.9

2413 [a] See Figure 3 for sample locations.

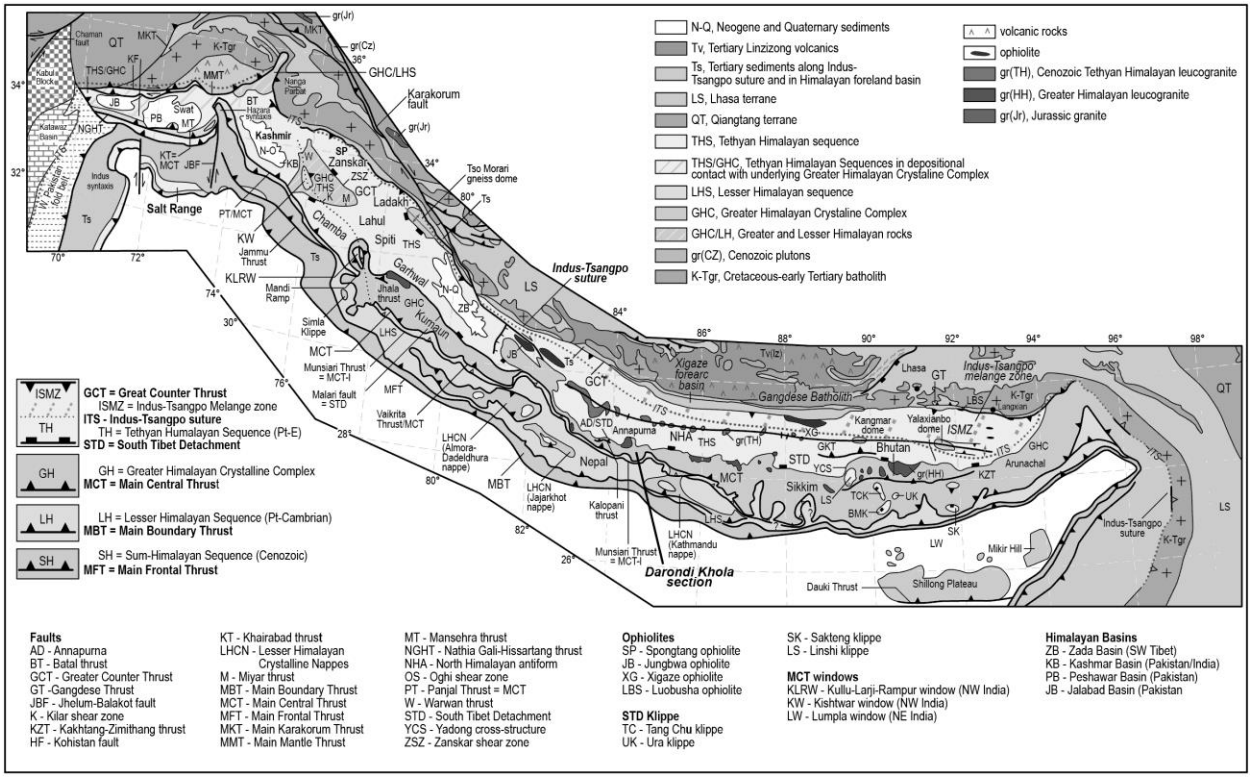

Figure 1. Geological map of the Himalayas after Yin (2006). Geological map of the Himalayas after Yin (2006). See Figure 2 for a cross-section through central Nepal and Figures 3-5 for the sample transect taken across the MCT shear zone along the Darondi Khola. See supplementary files for this figure in color.

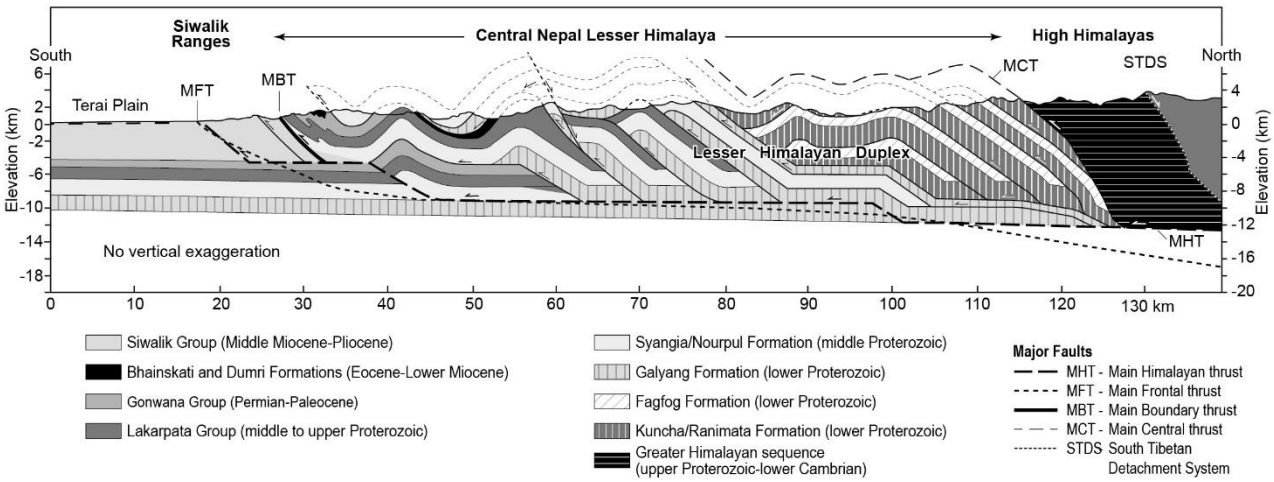

Figure 2. Generalized cross-section through the Himalayas in central Nepal after DeCelles (2015) and Robinson et al. (2006). See additional cross-sections in the range in DeCelles et al. (2020).

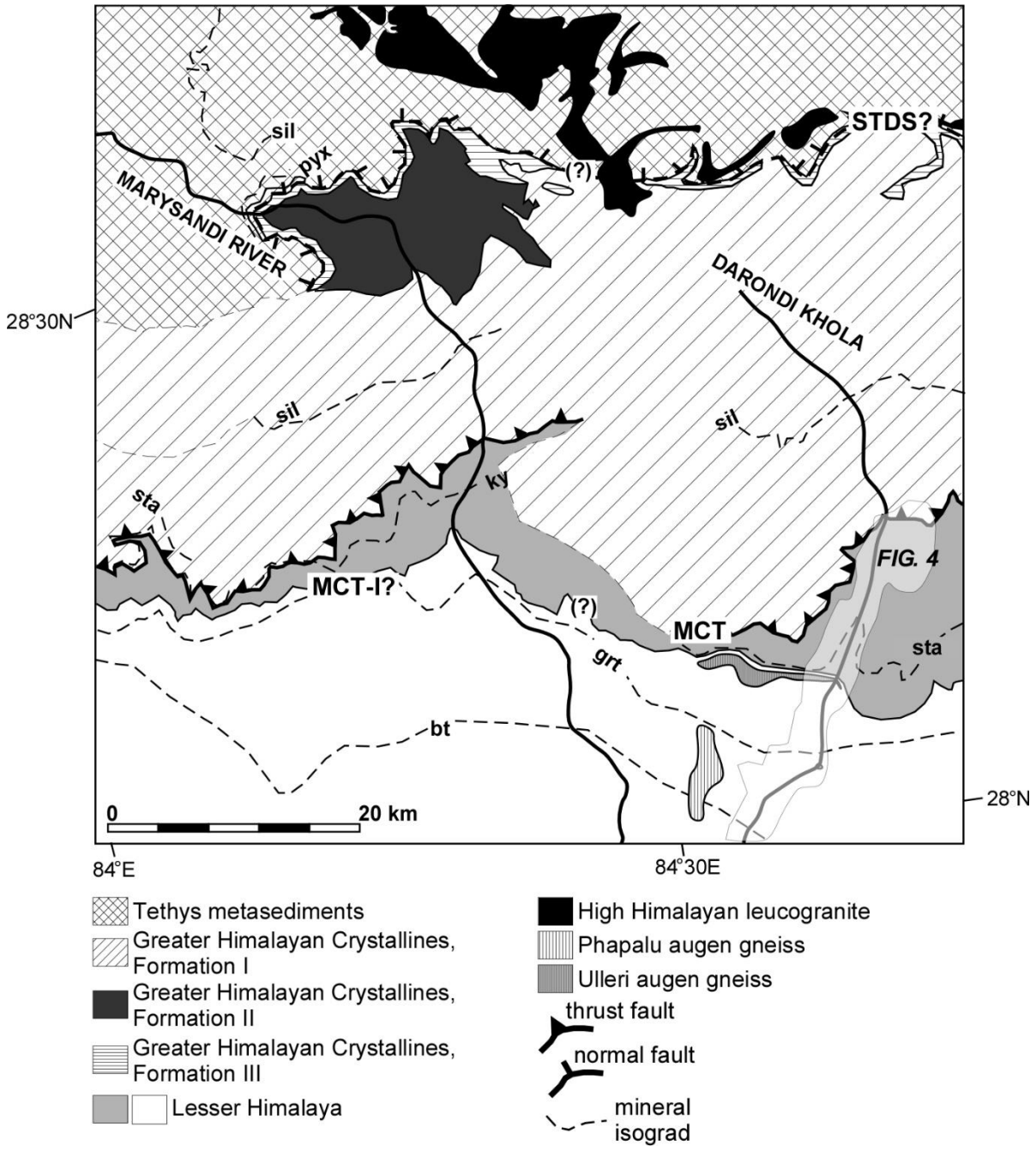

Figure 3. Generalized geological map of the Annapurna-Manaslu-Ganesh region of central Nepal after Colchen et al. (1980). Isograds are dashed and labeled: bt= biotite, grt= garnet; ky= kyanite; sta= staurolite; sil= sillimanite; pyx= pyroxene, carbonate lithologies. STDS? = the presence of the South Tibetan Detachment is debated; MCT= Main Central Thrust; MCT-I?= the presence of Arita's (1983) thrust at the base of the MCT shear zone is debated.

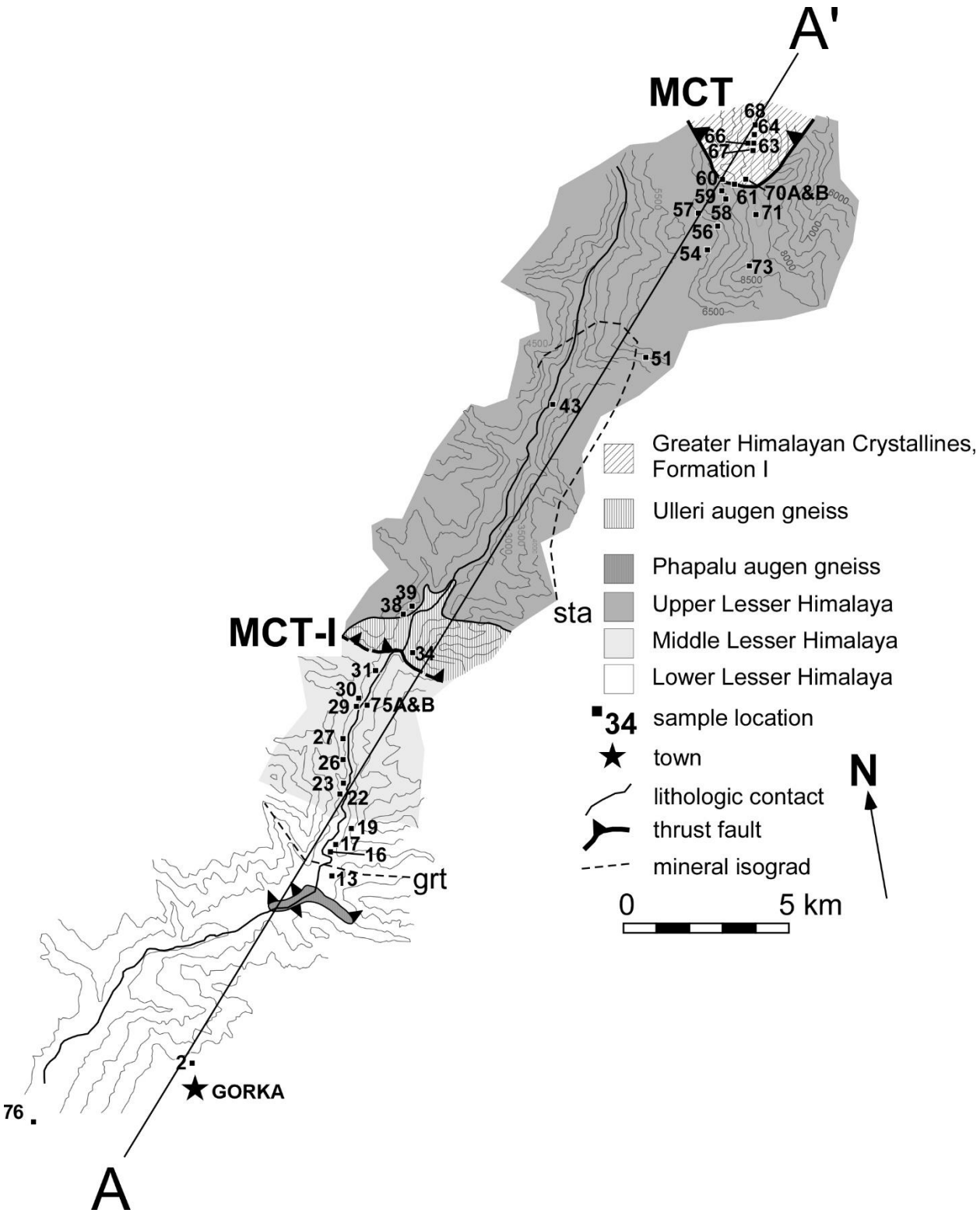

Figure 4. Sample location map from rocks collected along the Darondi Khola. The contour interval is 500 ft. See Figure 3 for the location of this transect on the geological map of the Himalayas. Samples are indicated by "DH#" in the text. Isograds are dashed and labeled (grt= garnet; stau= staurolite). See figure 5 for a cross-section along A-A'.

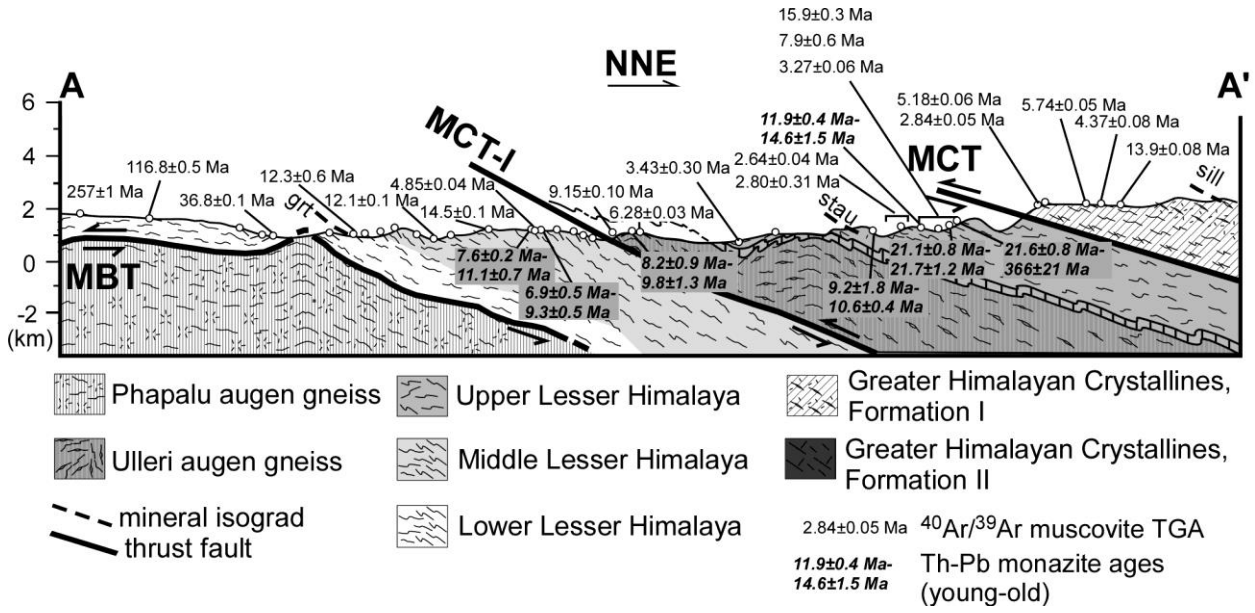

Figure 5. Cross-section across the Darondi Khola section showing available muscovite $^{40}Ar/^{39}Ar$ and Th-Pb ages after Catlos et al. (2001). See Figure 4 for line of section.

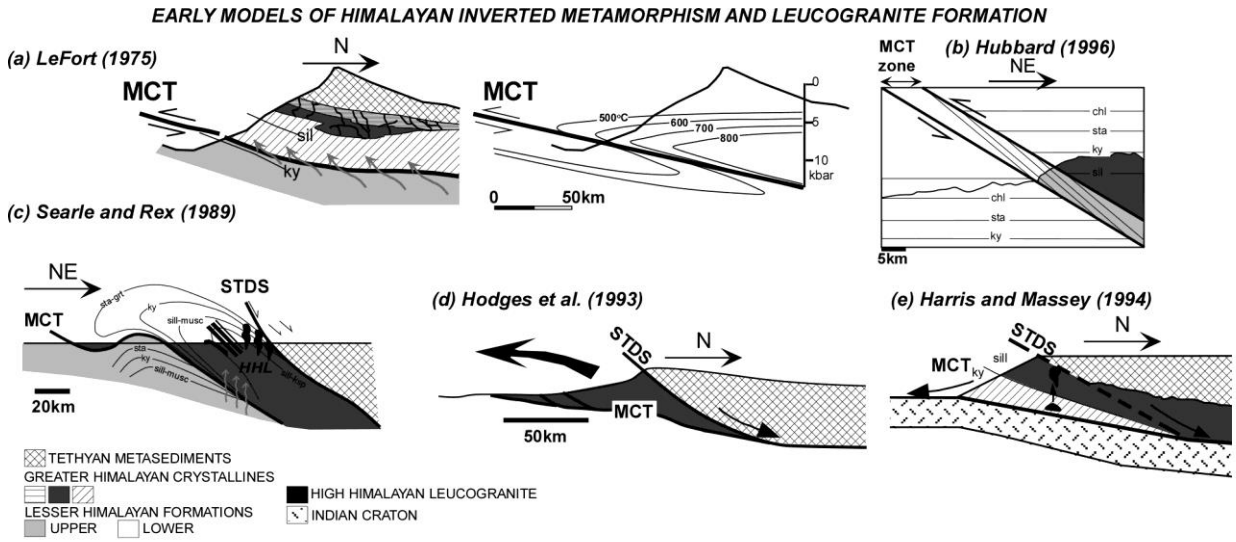

Figure 6. Cross-sections of early models of Himalayan inverted metamorphism and leucogranite formation. (A) The "hot-iron" model of LeFort 1975. (B) Juxtaposing right-way-up metamorphic isograds after Hubbard (1996). (C) A combination of models in panels (A) and (B) after Searle and Rex (1989). Wedge extrusion models after (D) Hodges et al. (1993) and (E) Harris & Massey (1994).

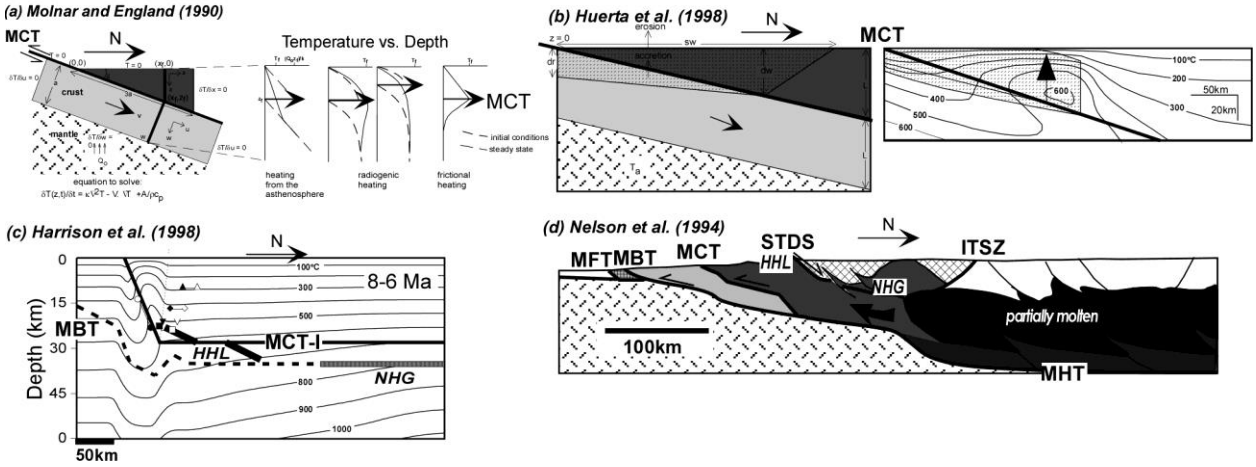

Figure 7. Cross-sections of early kinematic models of Himalayan inverted metamorphism and leucogranite formation. (A) After Molnar and England (1990). (B) After Huerta et al. (1998). (C) After Harrison et al. (1989). (D) After Nelson et al. (1996).

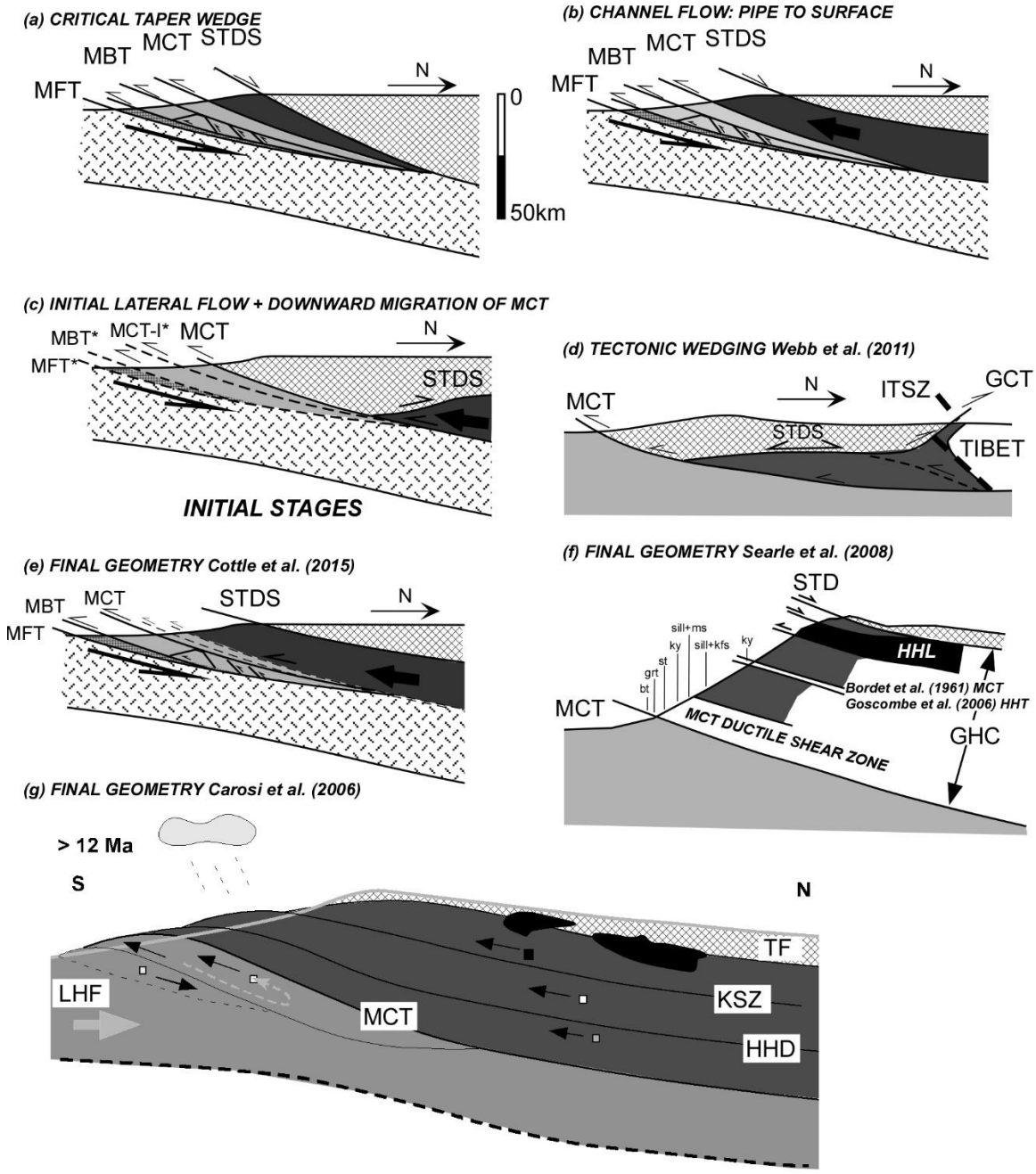

Figure 8. (A) An illustration of the critical taper model. (B) Schematic of channel flow and wedge extrusion. (C) A combination of critical taper and tectonic wedging of the GHC. A "*" indicates an incipient fault. (D) Illustration of GHC tectonic wedging after Webb et al. (2011). Panels (E) and (F) show the final geometry of the range, which has affected the position and definition of the MCT. Panel (G) showing the development of the MCT shear zone as rocks shown as squares within the footwall accrete to the hanging wall of the MCT. Faults within the GHC include the Kalopani shear zone (KSZ) and High Himalayan discontinuity (HHD). Panels (A), (B), (C), and (E) are after Cottle et al. (2015), panel (F) is after Searle et al. (2008), and panel (G) after Carosi et al. (2006).

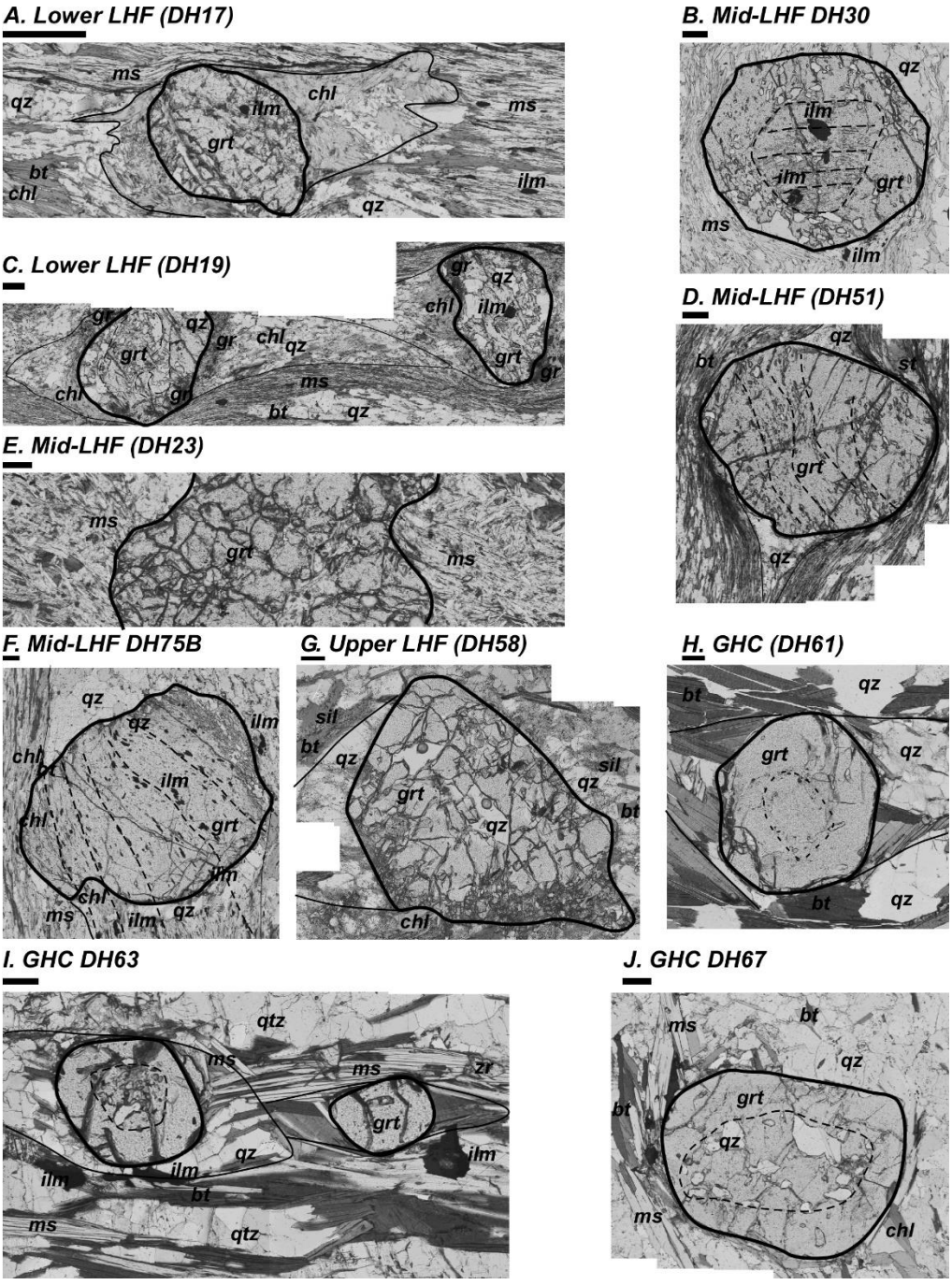

Figure 9. Selected petrographic (plane-polarized light) images of samples along the Darondi Khola showing the relationship of the garnet porphyroblasts and rock textures. Garnets are outlined using bold lines. Pressure shadows and inclusion trails are indicated by lighter and dashed lines, respectively. Mineral abbreviations after Whitney and Evans (2010). Panels are labeled with the sample numbers. The scale bar for each image is 200 um. See Figures 4 and 5 for sample locations. See supplementary files for this figure in color.

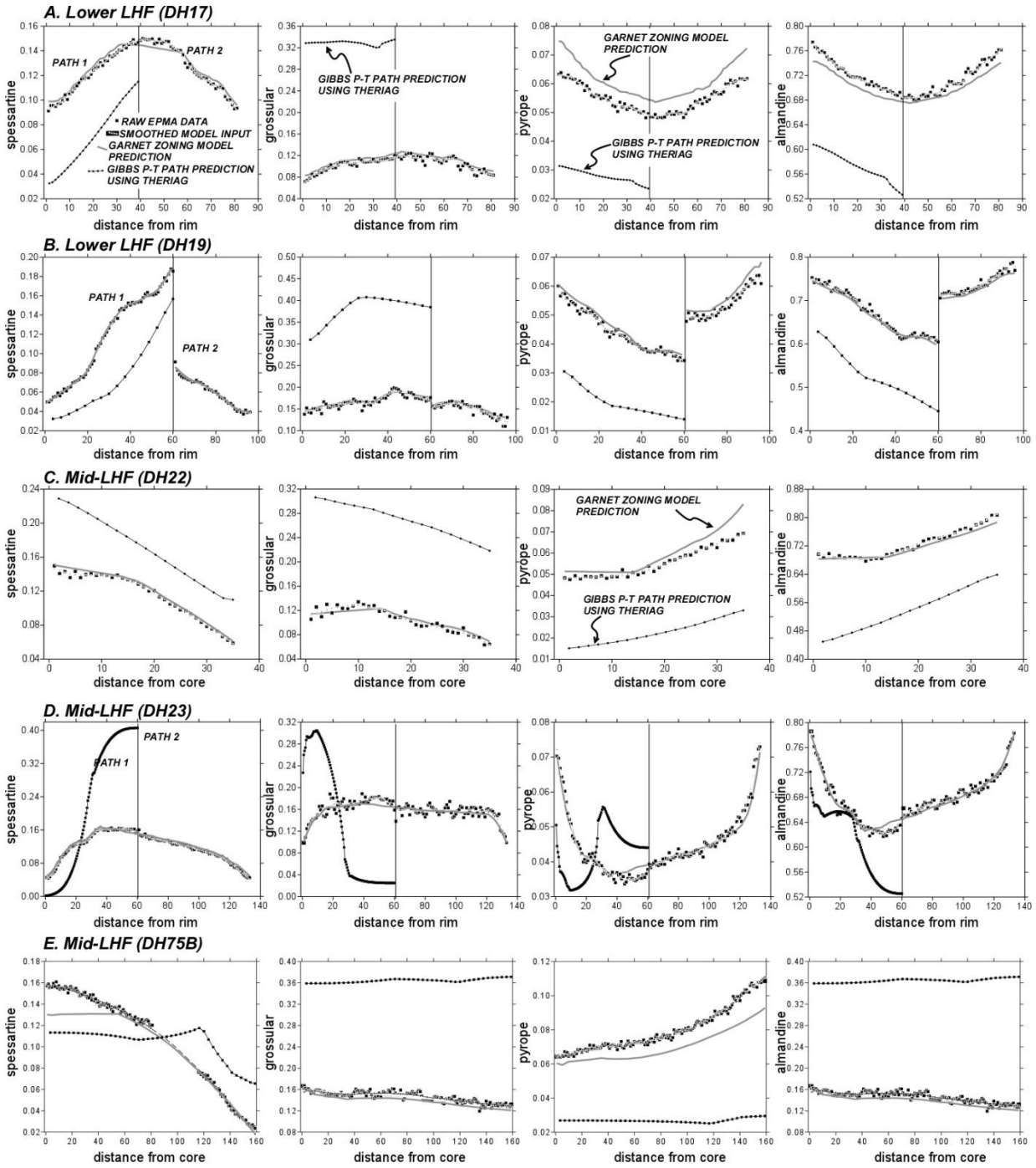

Figure 10. Compositional transects across garnets in lower LHF samples (A) DH17 and (B) DH19, and middle LHF samples (C) DH22, (D) DH23, and (E) DH75B. Distance is in analytical points, and the spacing between the points is ~20μm. The larger black squares are the raw electron microprobe data, whereas the smaller black squares near the EPMA data points are the smoothed data used for input into the model to generate the high-resolution P-T paths. The high-resolution P-T paths predict garnet zoning, which is shown by the bold gray lines. TheriaG was used to predict the garnet zoning for the Gibb's P-T paths, and these are also indicated.

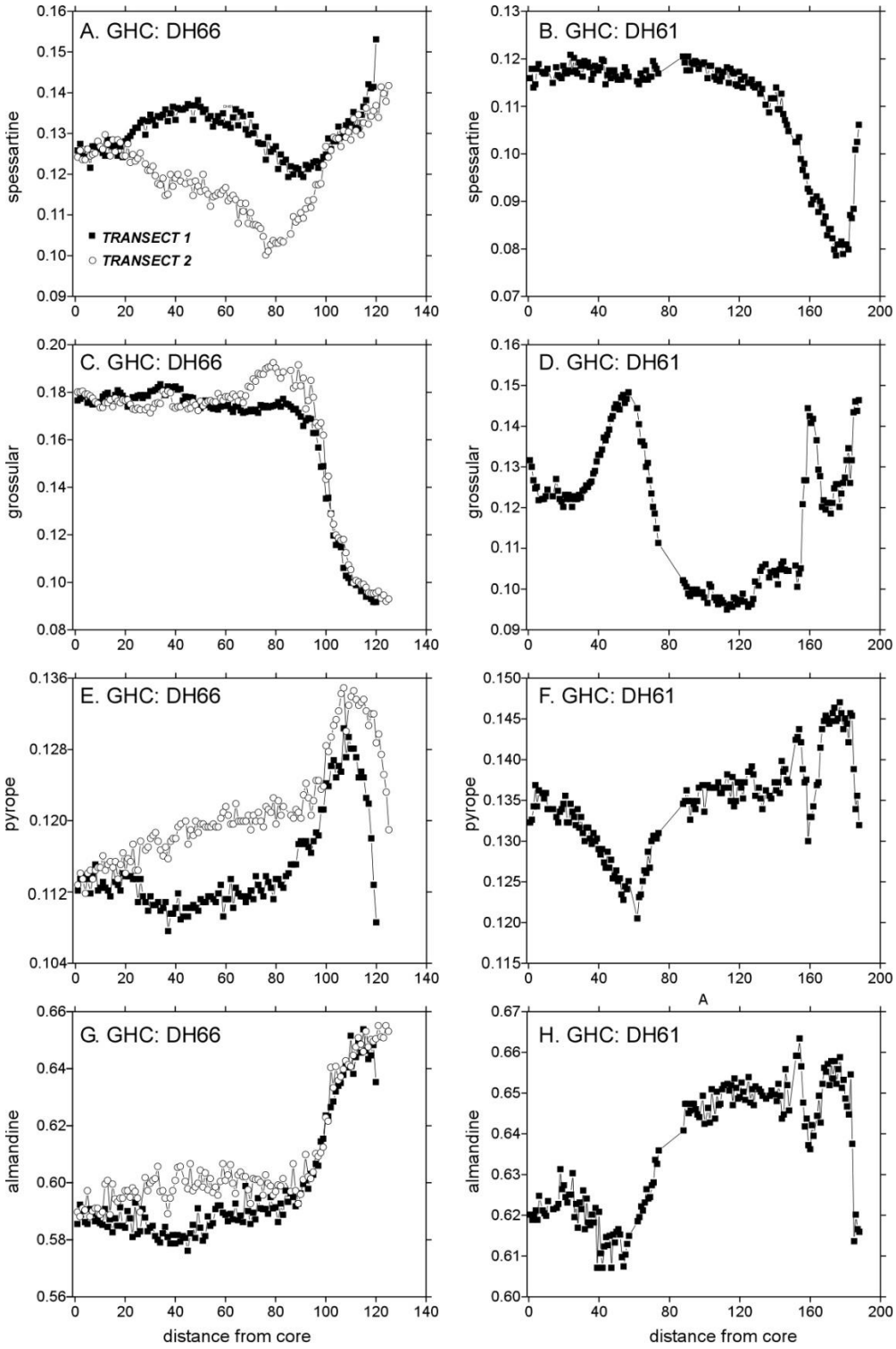

Figure 11. Compositional transects across garnets in GHC samples DH66 (two transects) in (A) spessartine, (C) grossular, (E) pyrope, and (G) almandine. Panels (B), (D), (F), and (H) are compositional transects in spessartine, grossular, pyrope, and almandine, respectively, across a garnet in sample DH61. Distance from the garnet core is in analytical points, and the spacing between the points is ~20μm.

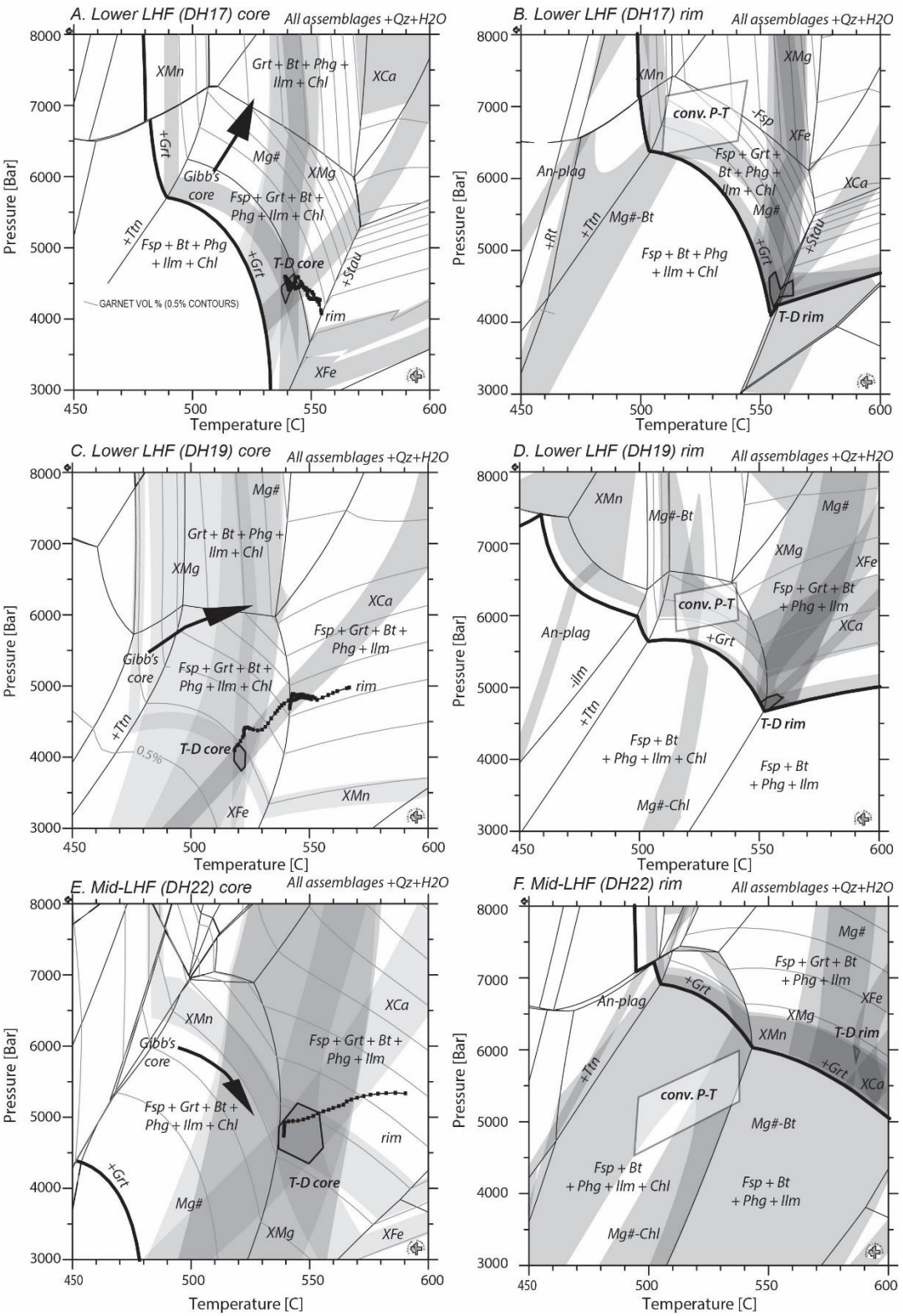

Figure 12. Isochemical phase diagrams from lower LHF samples DH17 (A) garnet core and (B) garnet rim, DH19 (C) core and D (rim), and mid-LHF sample DH22 (E) core and (F) rim. See text for entire figure caption.

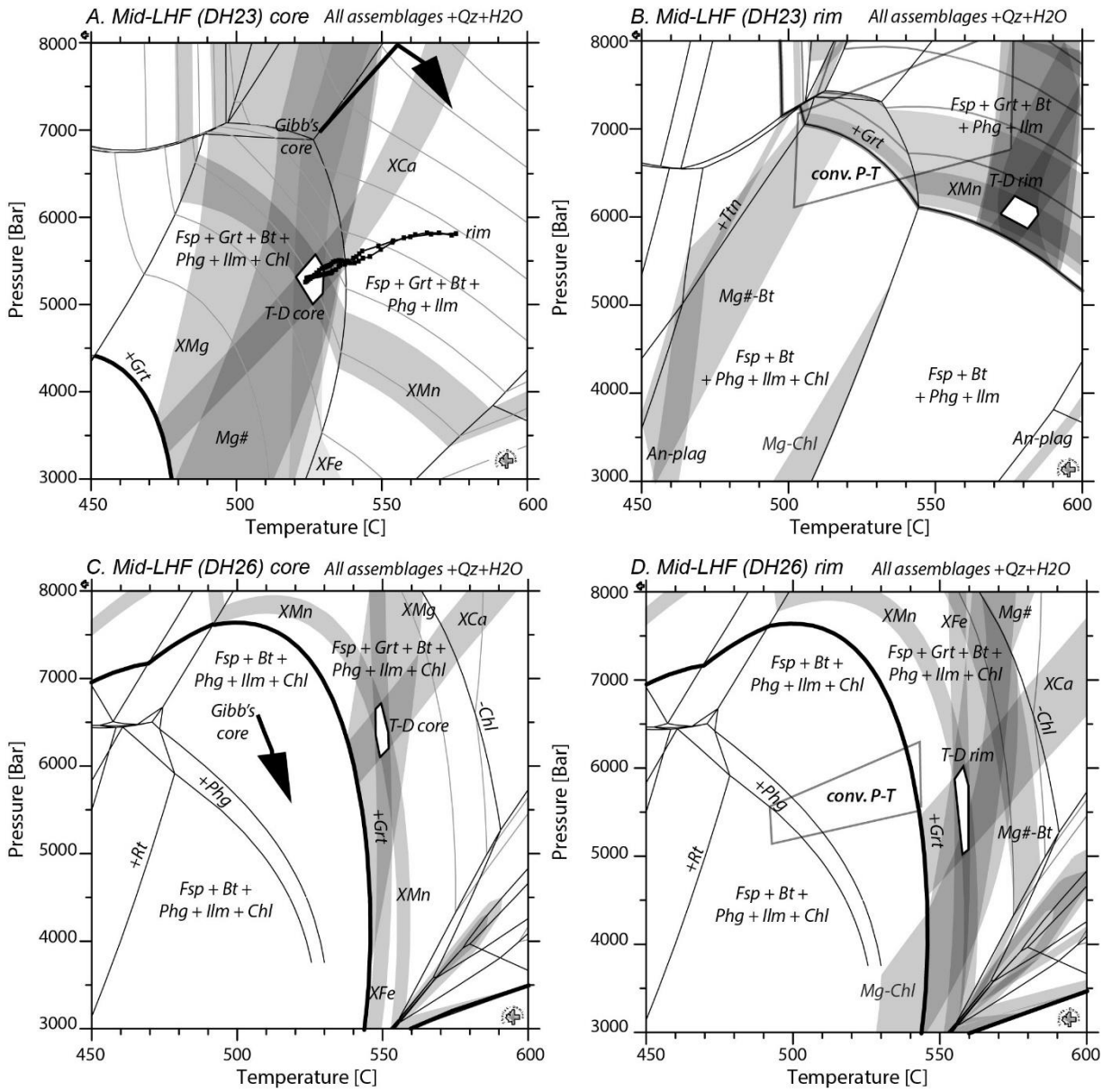

Figure 13. Isochemical phase diagrams from middle LHF samples DH23 (A) garnet core and (B) rim and DH26 (C) core and (D) rim. See Figures 4 and 5 for sample locations. Detailed caption is the same as in Figure 12. High-resolution P-T paths for sample DH23 were generated from two garnet core-to-rim transects after the approach of Moynihan & Pattison (2013). These are compared to the P-T paths obtained using the Gibb's method for the samples using the same data by Kohn et al. (2001). No data was available for the garnet transect for sample DH26, so a high-resolution P-T path was not created. In this case, the rock bulk composition (Table 3) was used for both core and rim panels.

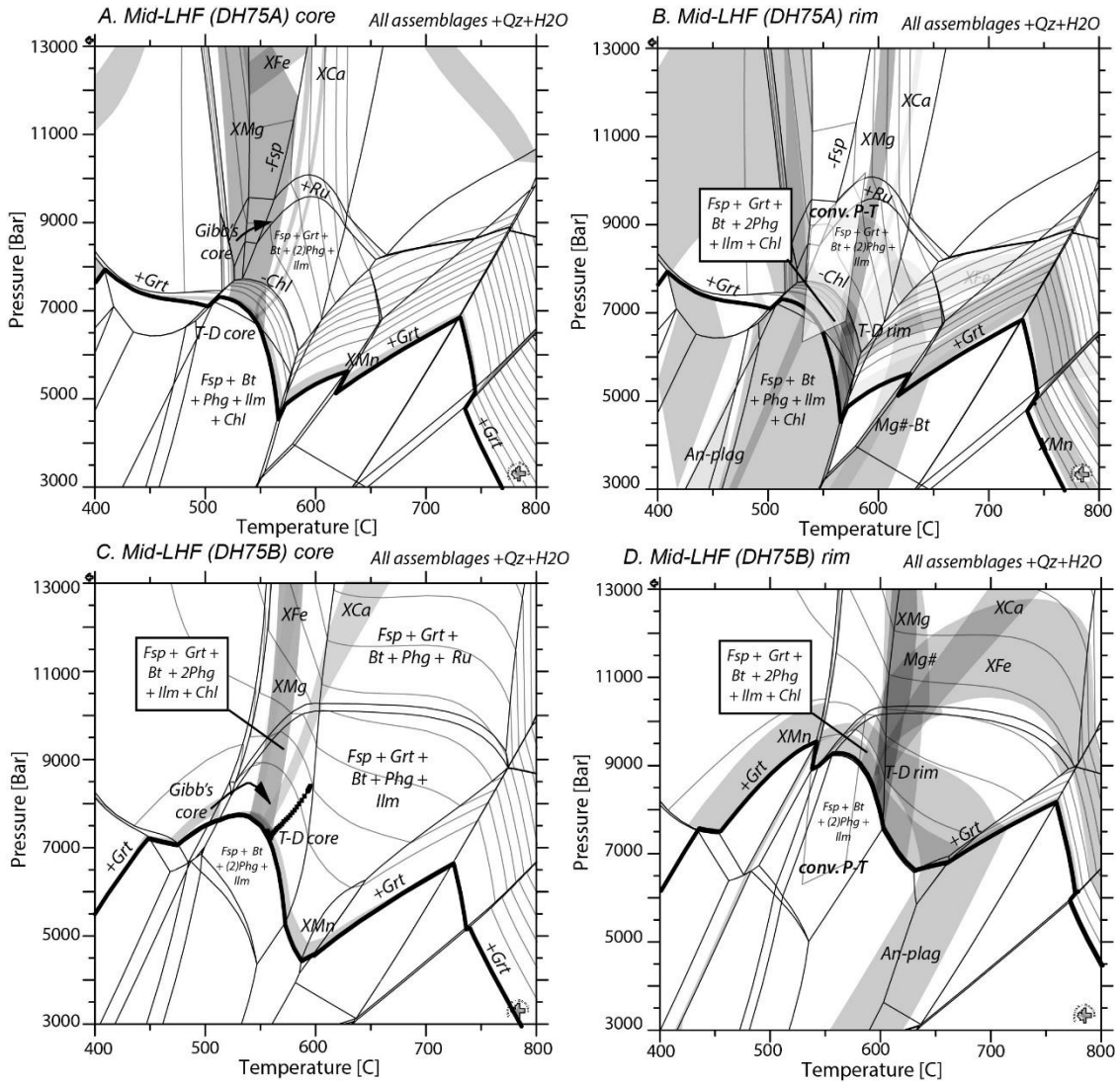

Figure 14. Isochemical phase diagrams from middle LHF samples DH75A (A) garnet core and (B) rim and DH75B (C) core and (D) rim. See Figures 4 and 5 for sample locations. Detailed caption is the same as in Figure 12. High-resolution P-T paths for sample DH75B were generated from garnet core-to-rim transects after the approach of Moynihan & Pattison (2013). These are compared to the P-T paths obtained using the Gibb's method for the samples using the same data by Kohn et al. (2001). The Gibb's path was also reported for sample DH75A. The starting point of the Gibb's P-T paths is labeled with "Gibb's core." The isochemical phase diagram for the garnet rim in sample DH75B was created using the final effective bulk composition generated by Theriak-Domino. In this case, isopleths for the garnet compositions reported for garnet rims are overlain on the diagram, as well as matrix mineral compositions isopleths for ±0.01 An-content for plagioclase (Kohn et al. 2001). Intersecting isopleths are indicated by the polygon and labeled as "T-D rim." No data was available for the garnet transect for sample DH75A, so a high-resolution P-T path was not created, and the rock bulk composition (Table 3) was used for both core and rim panels. In the rim panels, data are compared to the conventional P-T conditions for the samples (grey polygon) using the same data reported by Kohn et al. (2001).

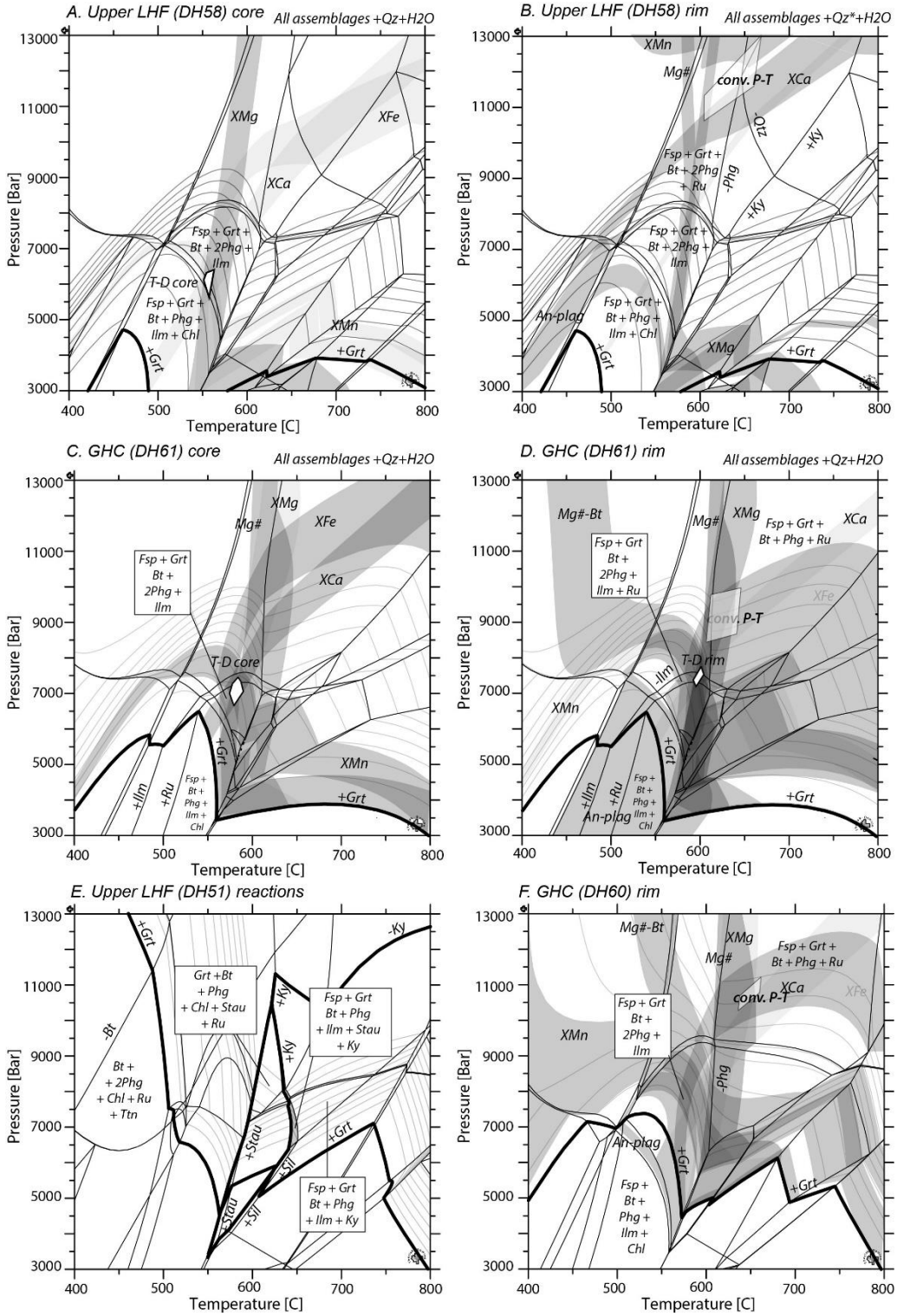

Figure 15. Isochemical phase diagrams from upper LHF samples DH58 (A) garnet core and (B) rim and (E) DH51 showing the mineral reactions only. The figure also includes isochemical phase diagrams from GHC sample DH61 (C) core and (D) rim, and DH60 (F) garnet rim data only. See text for detailed caption.

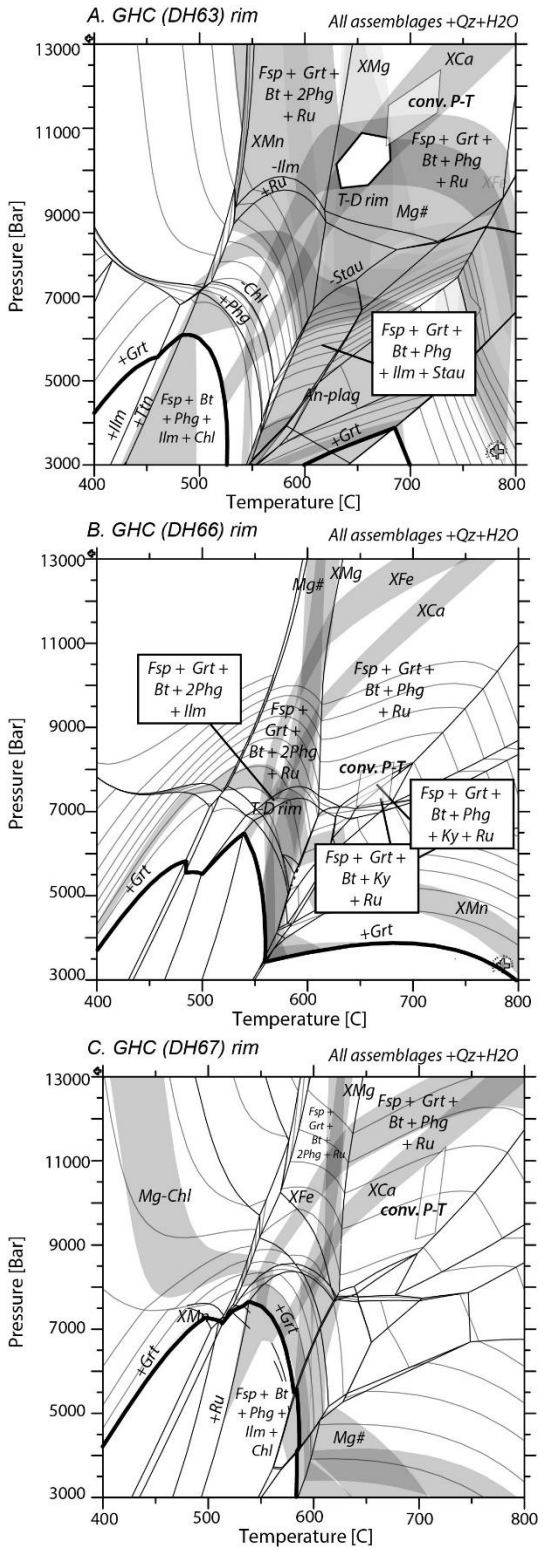

Figure 16. Isochemical phase diagrams from GHC samples (A) DH63, (B) DH66, and (C) DH67. See Figures 4 and 5 for sample locations. See manuscript text for detailed caption.

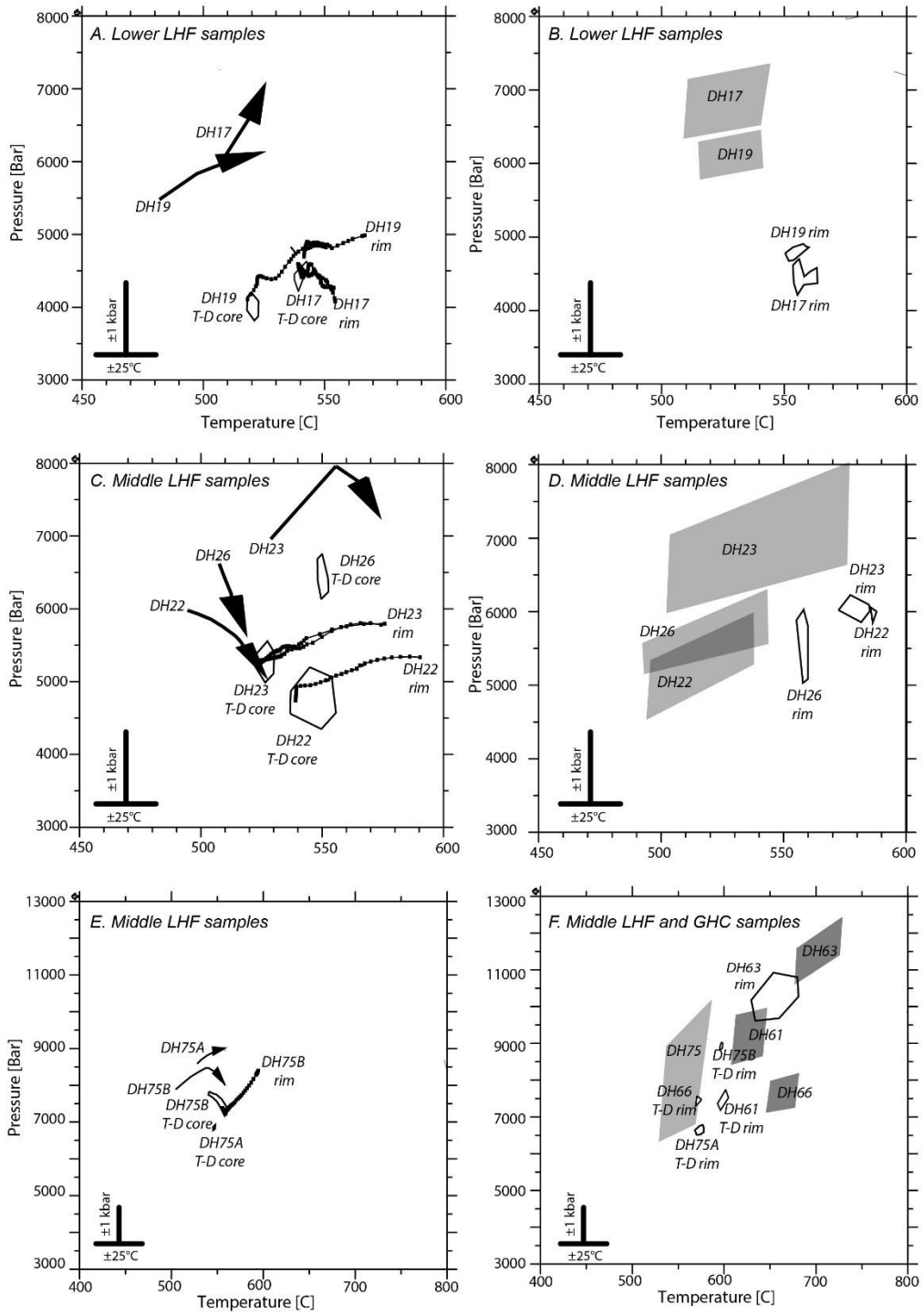

Figure 17. Summary of the P-T conditions and paths reported in Figures 12-16. In panels (A), (C), and (E), Gibb's P-T paths are shown as bold arrows and high-resolution P-T paths are labeled with core and rim points. In panels (B), (D), and (F), rim data generated using isopleth (white polygons) and conventional thermobarometry (grey polygons) are compared. Uncertainty scales in T (±25°C) and P (±1 kbar) are shown as insets in each panel.

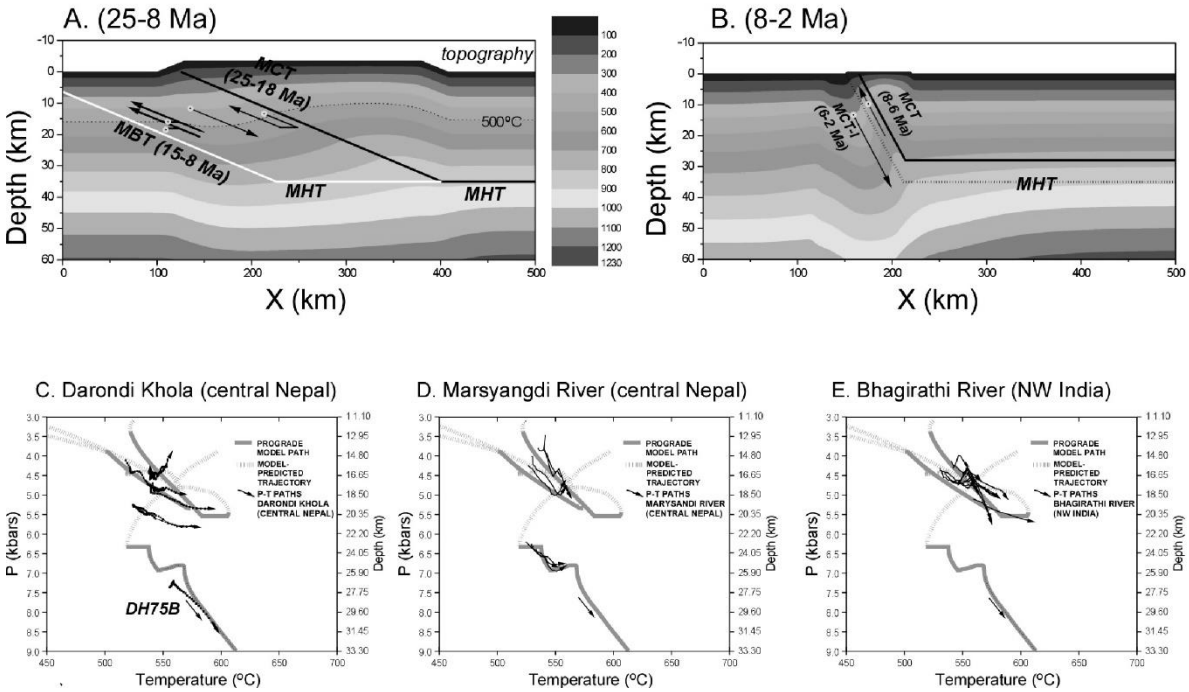

Figure 18. (A) Thermal-kinematic model cross-section after Catlos et al. (2018) showing the MCT (dark line) and MBT (white line) from 25 to 8 Ma. The MCT and MBT sole into the MHT at depth. Isothermal sections in degree increments are indicated by the scale bar. The isotherms show the thermal situation at 18 Ma after MCT slip. Example sample trajectories on the diagram are represented by arrows with dots at the initial and heads at the final position. The MCT is active from 25 to 18 Ma, whereas slip transfers to the MBT from 15 to 8 Ma. (B) The model cross-section of the reactivation of the MCT shear zone from 8 to 2 Ma. Both the MCT and MCT-I sole into the MHT at depth. This panel represents the thermal situation at 6 Ma right before the development of MCT shear zone inverted metamorphism. Example sample trajectories are shown. (C) P-T diagram showing the trajectories of the model predictions for samples panels A and B and high-resolution P-T paths for the Darondi Khola samples. Sample DH75B is identified. Panels (D) and (E) show the same model predictions but high-resolution P-T paths from the Marsyangdi River (Catlos et al., 2018) and Bhagirathi River transects (Catlos et al., 2020). See supplementary files for this figure in color.

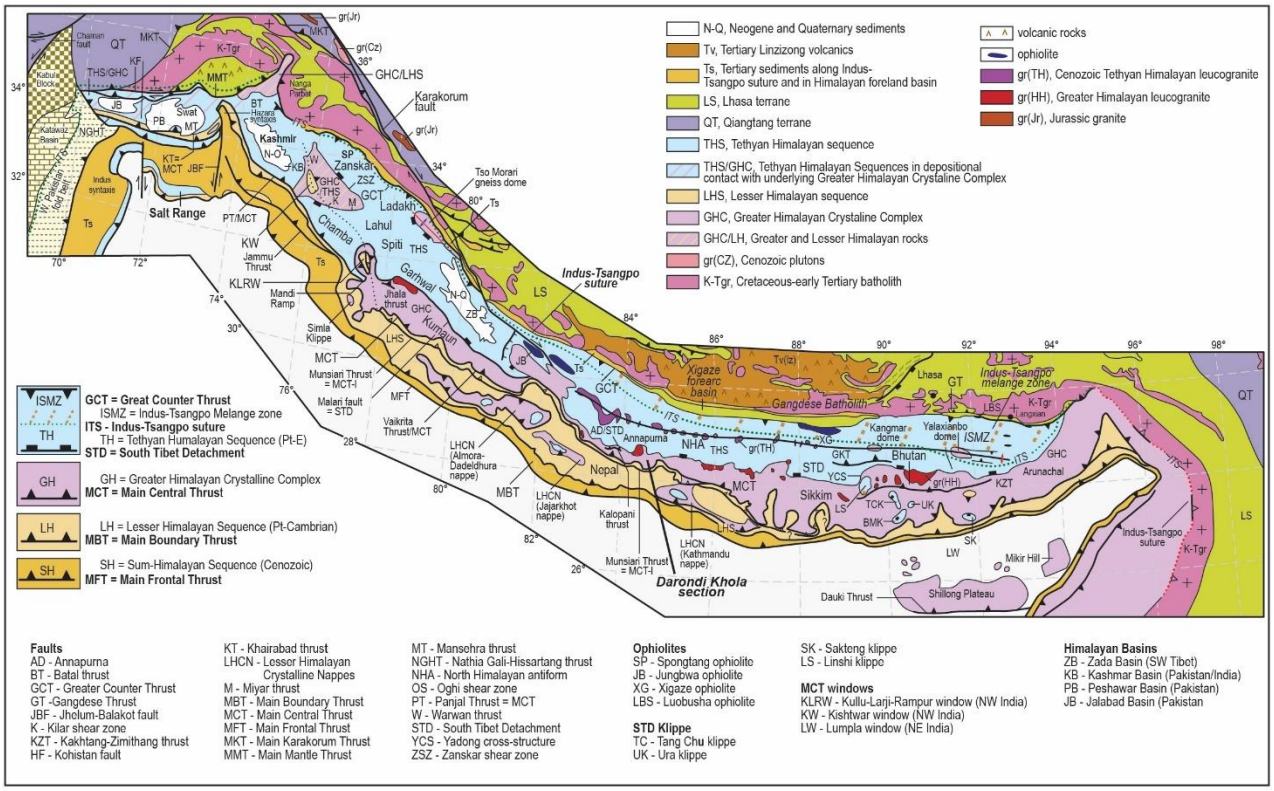

Figure S1. Geological map of the Himalayas after Yin (2006). Geological map of the Himalayas after Yin (2006). See Figure 2 for a cross-section through central Nepal and Figures 3-5 for the sample transect taken across the MCT shear zone along the Darondi Khola.

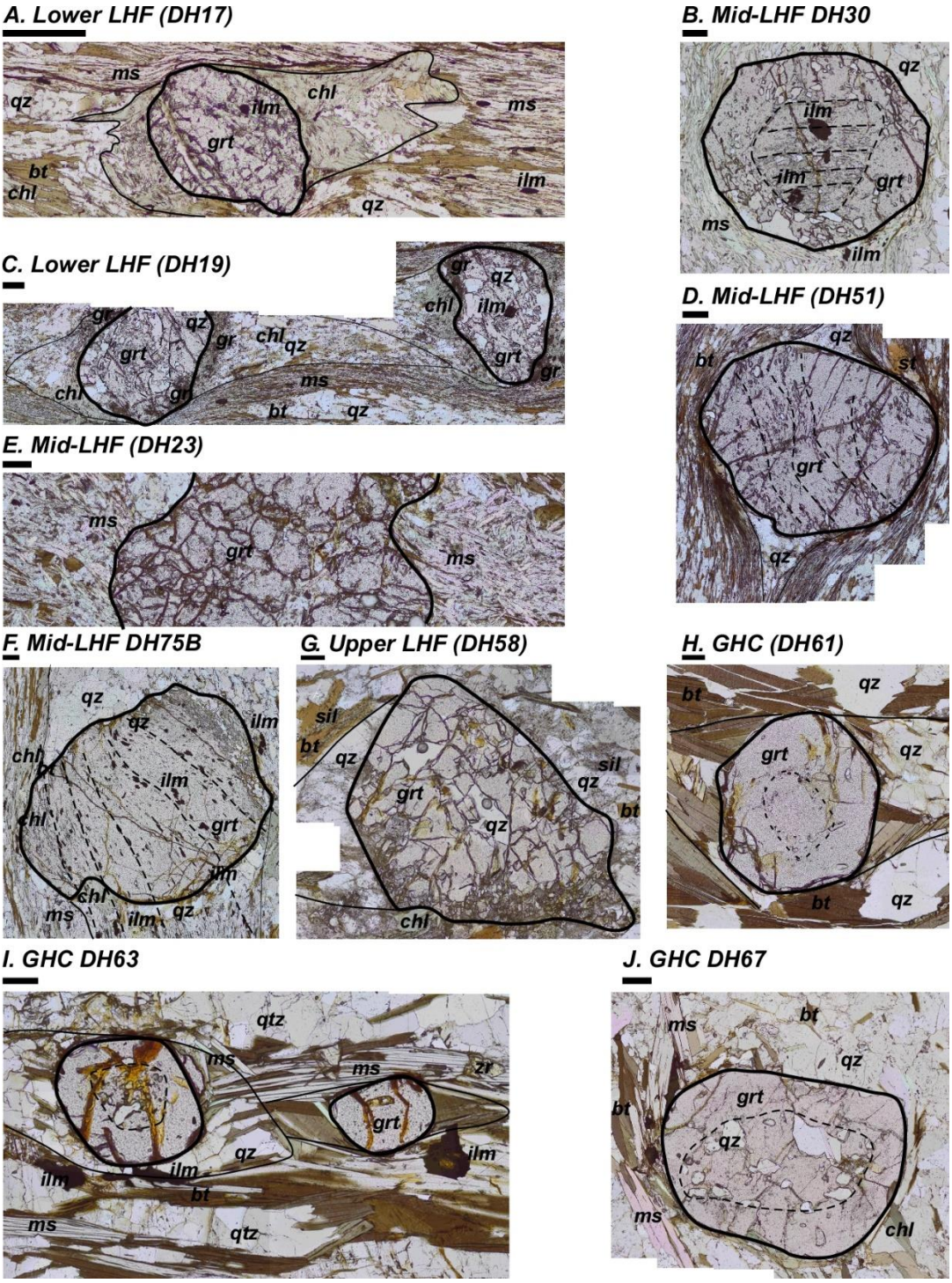

Figure S9. Selected petrographic (plane polarized light) images of samples along the Darondi Khola showing the relationship of the garnet porphyroblasts and rock textures. Garnets are outlined using bold lines. Pressure shadows and inclusion trails are indicates by lighter and dashed lines, respectively. Mineral abbreviations after Whitney and Evans (2010). Panels are labeled with sample number. The scale bar for each image is 200 μm. See Figures 4 and 5 for sample locations.

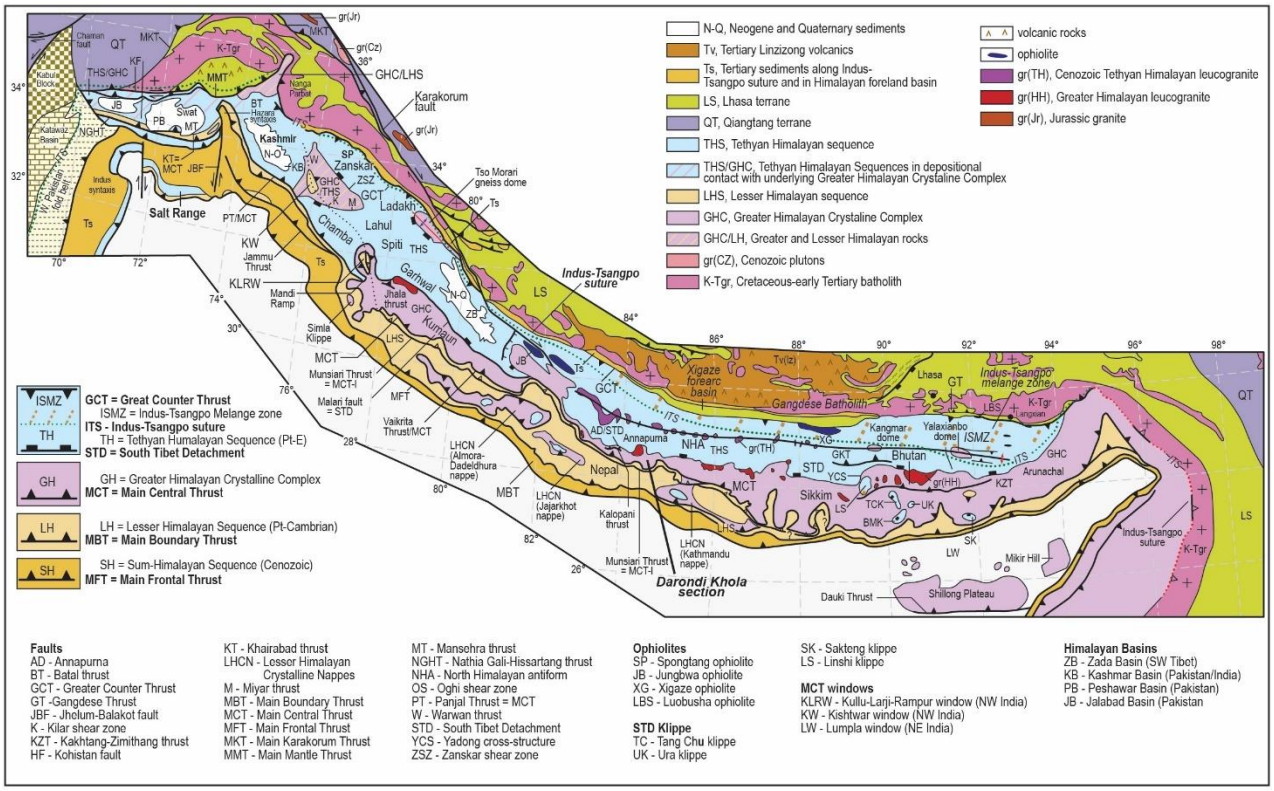

Figure S1. Geological map of the Himalayas after Yin (2006). Geological map of the Himalayas after Yin (2006). See Figure 2 for a cross-section through central Nepal and Figures 3-5 for the sample transect taken across the MCT shear zone along the Darondi Khola.

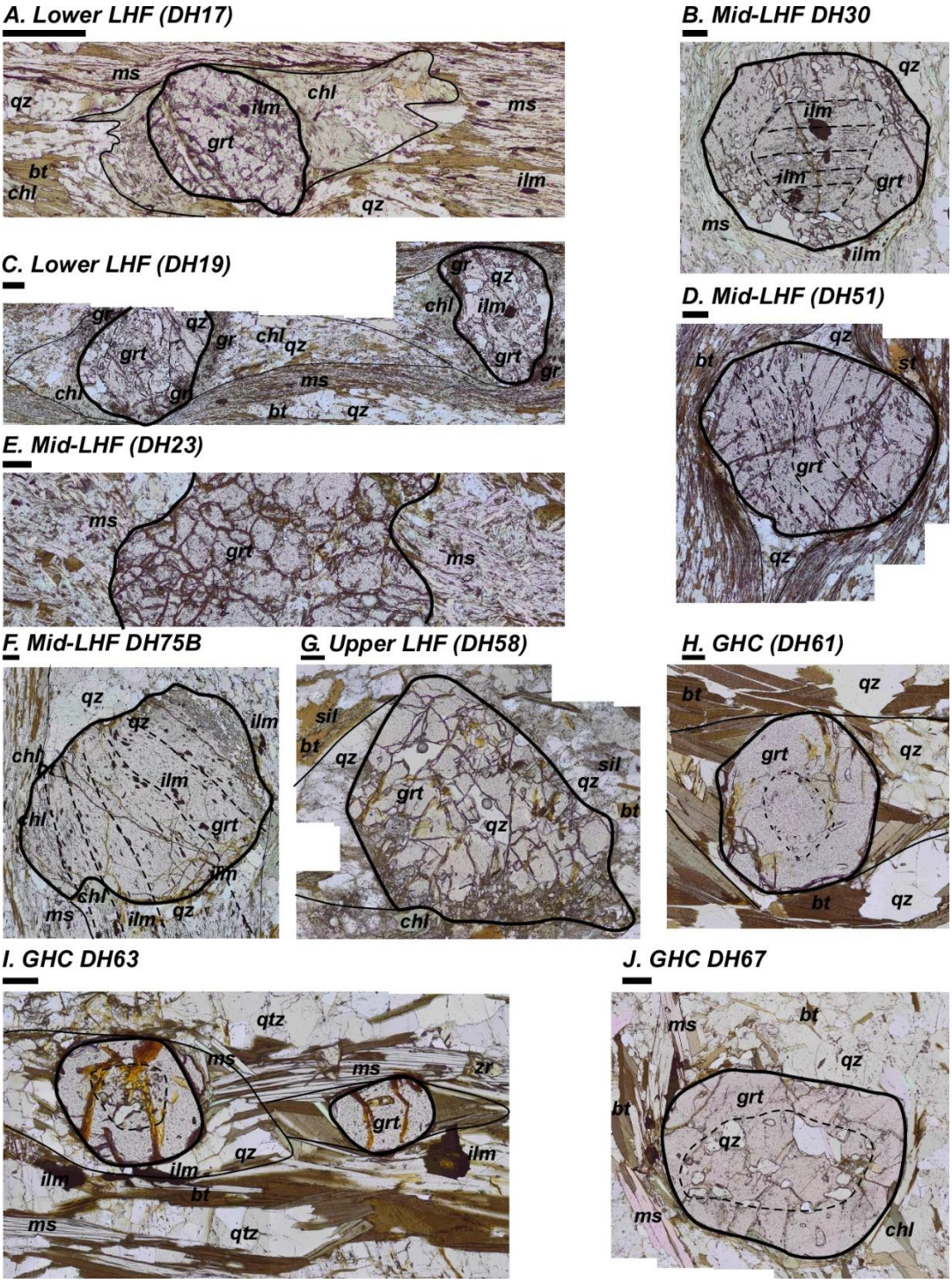

Figure S9. Selected petrographic (plane polarized light) images of samples along the Darondi Khola showing the relationship of the garnet porphyroblasts and rock textures. Garnets are outlined using bold lines. Pressure shadows and inclusion trails are indicates by lighter and dashed lines, respectively. Mineral abbreviations after Whitney and Evans (2010). Panels are labeled with sample number. The scale bar for each image is 200 μm. See Figures 4 and 5 for sample locations.